Jānis Alnis

Fizikas maģistrs / Master in Physics

Koherenti procesi sārmu metālu ierosmē un analītiskā spektroskopija, izmantojot diožu lāzerus

---

Coherent Processes in Alkali Metal Excitation and Analytical Spectroscopy with Diode Lasers

Promocijas darbs / Doctor thesis

Latvijas Universitāte / University of Latvia

Rīga – 2002

Disertācijā iekļauto publikāciju saraksts

List of publications included in thesis

[dis1] J. Alnis, M. Auzinsh, "Alignment - orientation conversion in molecules in an external magnetic field caused by a hyperfine structure", *Eur. Phys. J. D* 11, 91 (2000).

[dis2] J. Alnis, M. Auzinsh, "Angular momentum spatial distribution symmetry breaking in Rb caused by a hyperfine structure in a magnetic field", *Phys. Rev. A* 63, 023407 (2001).

[dis3] J. Alnis, M. Auzinsh, "Reverse dark resonance in Rb atom excited by a diode laser", *J. Phys. B* 34, 3889 (2001).

[dis4] U. Gustafsson, J. Alnis, S. Svanberg, "Atomic spectroscopy with violet laser diodes", *Am. J. Phys.* **68**, 660 (2000).

[dis5] U. Gustafsson, G. Someasfalean, J. Alnis, S. Svanberg, "Frequency-modulation spectroscopy with blue diode lasers", *Appl. Opt.* 39, 3774 (2000).

[dis6] J. Alnis, U. Gustafsson, G. Someasfalean and S. Svanberg, "Sum-frequency generation with a blue diode laser for mercury spectroscopy at 254 nm", *Appl. Phys. Lett.* 76, 1234 (2000).

[dis7] M. Sjöholm, G.Someasfalean, J. Alnis, S. Andersson-Engels and S. Svanberg, "Analysis of gas dispersed in scattering media", *Opt. Lett.* 26, 16 (2001).

[dis8] G. Someasfalean, M. Sjöholm, J. Alnis, C. af Klinteberg, S. Andersson-Engels and S. Svanberg, "Concentration measurement of gas imbedded in scattering media employing absorption and time-resolved laser spectroscopy", *Appl. Opt.*, accepted.

J. Alnis

Disertācijā iekļauto publikāciju saraksts

List of publications included in thesis

[dis1] J. Alnis, M. Auzinsh, "Alignment - orientation conversion in molecules in an external magnetic field caused by a hyperfine structure", *Eur. Phys. J. D* 11, 91 (2000).

[dis2] J. Alnis, M. Auzinsh, "Angular momentum spatial distribution symmetry breaking in Rb caused by a hyperfine structure in a magnetic field", *Phys. Rev. A* 63, 023407 (2001).

[dis3] J. Alnis, M. Auzinsh, "Reverse dark resonance in Rb atom excited by a diode laser", *J. Phys. B* 34, 3889 (2001).

[dis4] U. Gustafsson, J. Alnis, S. Svanberg, "Atomic spectroscopy with violet laser diodes", *Am. J. Phys.* 68, 660 (2000).

[dis5] U. Gustafsson, G. Someasfalean, J. Alnis, S. Svanberg, "Frequency-modulation spectroscopy with blue diode lasers", *Appl. Opt.* 39, 3774 (2000).

[dis6] J. Alnis, U. Gustafsson, G. Someasfalean and S. Svanberg, "Sum-frequency generation with a blue diode laser for mercury spectroscopy at 254 nm", *Appl. Phys. Lett.* 76, 1234 (2000).

[dis7] M. Sjöholm, G.Someasfalean, J. Alnis, S. Andersson-Engels and S. Svanberg, "Analysis of gas dispersed in scattering media", *Opt. Lett.* 26, 16 (2001).

[dis8] G. Someasfalean, M. Sjöholm, J. Alnis, C. af Klinteberg, S. Andersson-Engels and S. Svanberg, "Concentration measurement of gas imbedded in scattering media employing absorption and time-resolved laser spectroscopy", *Appl. Opt.*, accepted.

J. Alnis

dis 1

Eur. Phys. J. D 11, 91–97 (2000)

THE EUROPEAN PHYSICAL JOURNAL D

EDP Sciences

Alignment-orientation conversion in molecules in an external magnetic field caused by a hyperfine structure

J. Alnis and M. Auzinsh[a]

Department of Physics, University of Latvia, 19 Rainis blvd., Riga LV-1586, Latvia

Received 15 July 1999 and Received in final form 17 November 1999

Abstract. The paper presents a discussion on the problem of alignment-orientation conversion in an excited state of molecules. It is shown that a rather strong alignment-orientation conversion effect in the excited molecular state can be caused by a joint action of an external magnetic field and hyperfine interaction. The orientation thus created is transverse, *i.e.* perpendicular to the direction of the external magnetic field. The magnitude of this effect is analyzed as dependent on molecular parameters.

PACS. 32.60.+i Zeeman and Stark effects – 32.10.Fn Fine and hyperfine structure

1 Introduction

Usually, if an ensemble of atoms or molecules is excited by linearly polarized light the spatial distribution of angular momentum of excited state particles possesses alignment. That means that the cylindrical symmetry of excitation light polarization vector **E**, that can be characterized by a double-head arrow $\Longleftrightarrow$, is transferred to the ensemble of atoms or molecules.

An interest about processes, that can break this symmetry and cause alignment-orientation conversion has been alive already for a long time. As a result, one may expect an appearance of angular momentum distribution that can be characterized by a single-head arrow $\Longrightarrow$. Experimentally appearance of an orientation can be detected as an emergence of circularly polarized fluorescence from such an ensemble of particles.

The possibility of conversion from alignment to orientation under the effect of anisotropic collisions was first considered by Lombardi [1] and Rebane [2]. They have shown that partial alignment-orientation conversion in an ensemble of atoms may be induced by anisotropic collisions when the angle between the direction of these anisotropic collisions and that of alignment differs from 0 or $\pm\pi/2$. The theoretical prediction was soon after confirmed in experimental observation [3,4].

The other group of works deals with electric field effects. Lombardi [5] described a circularity signal from He in a high-frequency capacitative electrodeless helium discharge. Necessary initial alignment in this case was produced by joint action of collisions with electrons and action of an external field. The electric field of the discharge was considered as a perturbing factor able to produce an orientation signal. Later the alignment-orientation conversion caused by external electric field leading to quadratic Stark effect in atoms or molecules was considered in great detail in [6–8]. This effect was suggested to be used to orient molecules selectively in beam experiments [9]. Recently alignment-orientation conversion in an electric field was utilized for measuring permanent dipole moments and Λ-doubling constants in NaK molecules [10].

In general, the main reason why an electric field is able to convert alignment into orientation is because an electric field is characterized by a polar vector. At the same time it is known that magnetic field, which is characterized by an axial vector can not change the symmetry of angular momentum distribution.

However, this obstruction can be circumvented if in addition to the linear Zeeman effect there exist any perturbing factors causing slight non-linearity in the primarily linear Zeeman effect. For example, as such a perturbing factor can serve hyperfine interaction in atoms or molecules. For the first time alignment-orientation conversion as a result of hyperfine interaction was predicted theoretically [11] and demonstrated experimentally by Lehmann [12]. He studied optical pumping of a diamagnetic ground state of atoms possessing magnetic hyperfine structure. Atoms were excited by an unpolarized light beam in presence of an external magnetic field. Joint action of hyperfine interaction and the external magnetic field directed along the unpolarized exciting light beam caused appearance of a *longitudinal* (along the magnetic field direction) orientation. This effect can be considered as a kind of magnetic dichroism.

Vigué with his colleagues studied theoretically as well as measured experimentally in an iodine molecule the appearance of a *longitudinal* orientation in an external magnetic field as a result of predissociation [13–15]. Such orientation can take place as a direct consequence of interference between magnetic and natural predissociation.

[a] e-mail: mauzins@latnet.lv

Not so long time ago it was shown theoretically as well as demonstrated experimentally that an external magnetic field can slightly mix together molecular states with opposite parity and, as a result, can cause the appearance of *transverse* orientation (perpendicular to the direction of the external field) from an initially aligned ensemble of molecules. It needs for this that the initial alignment is created in a direction differing from 0 or $\pm\pi/2$ with respect to the external field and that the intramolecular interaction-caused Zeeman effect deviates slightly from a linear one [16,17].

In this paper we will demonstrate that the external magnetic field in the presence of hyperfine interaction can cause the appearance of a *transverse* orientation as well. In other words, we will demonstrate that the hyperfine structure (HFS) in an external magnetic field can cause the appearance of a kind of magnetic birefringence.

2 Orientation of the molecules

An easy way to characterize the angular momentum distribution in an ensemble of atoms or molecules consists in applying an angular momentum quantum density matrix. Let us consider a molecule possessing hyperfine structure which is placed in an external magnetic field. Let us further assume that angular momentum alignment in the excited state of this molecule is created by an absorption of linearly polarized light with an arbitrarily directed E vector. In this situation the density matrix, that characterizes coherence between magnetic sublevels with quantum numbers M and M' for an ensemble of molecules in an excited state can be calculated as [18]

$$ {}^{kl}f_{MM'} = \frac{\tilde{\Gamma}_p}{\Gamma + i^{kl}\Delta\omega_{MM'}} \times \sum_{j\mu} \langle \gamma_k M | \hat{\mathbf{E}}^* \cdot \hat{\mathbf{D}} \; \eta_j \mu \rangle \left(\langle \gamma_l M' | \hat{\mathbf{E}}^* \cdot \hat{\mathbf{D}} \, | \eta_j \mu \rangle \right)^* . \quad (1) $$

In this equation $\tilde{\Gamma}_p$ is a reduced absorption rate, Γ is the excited state relaxation rate and ${}^{kl}\Delta\omega_{MM'}$ is the splitting of magnetic sublevels M and M' belonging to the excited state levels k and l. Magnetic quantum numbers of the ground state level η_j are denoted by μ and the magnetic quantum numbers of the excited state level γ_k by M or M'.

In an external magnetic field the ground and excited state levels η_j and γ_k are not characterized any more by total angular momentum quantum numbers F'' and F' respectively, but are mixture of these states

$$ |\gamma_k M\rangle = \sum_{F'=J'-I}^{F'=J'+I} C^{(e)}_{kF'} \; |F', M\rangle \, . $$

$$ |\eta_j \mu\rangle = \sum_{F''=J''-I}^{F''=J''+I} C^{(g)}_{jF''} \, |F'', \mu\rangle \quad (2) $$

created by an external field. $C^{(e)}_{kF'}$, $C^{(g)}_{jF''}$ are the wave function expansion coefficients that represent the expansion of the molecular state in a magnetic field over the wave functions of hyperfine levels in absence of an external field. The method for calculating these coefficients will be described further.

There are several methods how to tell whether or not a particular molecular state described by a density matrix (1) possesses orientation. One possibility is to expand this matrix over the irreducible tensorial operators. These expansion coefficients can directly be attributed to the alignments and the orientation of the molecular ensemble [7,19,20]. This method was used previously to analyze hyperfine interaction in the H_2 molecule and the influence of this interaction on the polarization of laser-induced fluorescence [21]. Another way which will be used in this paper is to calculate directly the fluorescence circularity rate

$$ C = \frac{I(E_{\text{left}}) - I(E_{\text{right}})}{I(E_{\text{left}}) + I(E_{\text{right}})} \quad (3) $$

from the density matrix in spontaneous transition from a particular excited state of the molecule. $I(E_{\text{left}})$ and $I(E_{\text{right}})$ are the intensities of the fluorescence with opposite circularity, if detected at some certain direction from the source containing excited molecules. If circularity differs form zero, then it means that the ensemble of molecules in excited state possesses an orientation. This is a functional way of calculating orientation of molecules, because in experimental studies this is a most frequently used approach to registering the appearance of orientation in an ensemble of molecules or atoms, see for example [6].

Let us assume that we register spontaneous fluorescence with a spectral device which does not resolve hyperfine components, say, an ordinary monochromator. The intensity of the fluorescence with definite polarization characterized by a vector $\mathbf{E}_f$ in a spontaneous transition from the excited state J', characterized by a set γ_k of levels in an external field, to the ground state J''_{final}, characterized by a set η_j of levels, can be calculated, according to [18], as

$$ I(\mathbf{E}_f) = I_0 \sum_{MM'\mu} \sum_{kl_j} \langle \gamma_k M | \hat{\mathbf{E}}_f^* \cdot \hat{\mathbf{D}} \, | \eta_j \mu \rangle \times \left(\langle \gamma_l M' | \hat{\mathbf{E}}_f^* \cdot \hat{\mathbf{D}} \; \eta_j \mu \rangle \right)^* {}^{kl} f_{M'M} . \quad (4) $$

To calculate the matrix elements entering equations (1, 4) some technical problems must be solved. Matrix elements of type $\langle \gamma_k M | \hat{\mathbf{E}}^* \cdot \hat{\mathbf{D}} \, | \eta_j \mu \rangle$ can be easily expressed through the matrix elements defined by hyperfine levels of the molecular states in absence of an external field

$$ \langle \gamma_k M | \hat{\mathbf{E}}^* \cdot \hat{\mathbf{D}} \; \eta_j \mu \rangle = \sum_{F'F''} C^{(e)}_{kF'} C^{(g)}_{jF''} \, \langle F' M | \hat{\mathbf{E}}^* \cdot \hat{\mathbf{D}} \, | F'' \mu \rangle \, . \quad (5) $$

To matrix elements defined by hyperfine states the Wigner-Eckart theorem [7,19,20] can be applied

$$\langle F'M|\,\hat{\mathbf{E}}^*\cdot\hat{\mathbf{D}}\,|F''\mu\rangle = \sum_q (E^q)^*\,(-1)^{F'-M} \times \begin{pmatrix} F' & 1 & F'' \\ -M & q & \mu \end{pmatrix} \langle F'\|\,\hat{D}\,\|F''\rangle . \quad (6)$$

Here, the light vector is represented by its components E^q in a cyclic system of coordinates [7,20]. Finally, the last reduced matrix element for an axially symmetric system, such as a diatomic molecule, can be written as [19]

$$\langle F'\|\,\hat{D}\,\|F''\rangle = (-1)^{J'+I+F''+1}\sqrt{(2F'+1)(2F''+1)} \times \begin{Bmatrix} J' & F' & I \\ F'' & J'' & 1 \end{Bmatrix} \langle J'\|\,\hat{D}\,\|J''\rangle . \quad (7)$$

All this allows to calculate an angular momentum distribution in an excited state of a molecule with HFS, if it absorbs light of definite polarization $\mathbf{E}$ while placed in an external magnetic field. This angular momentum distribution is characterized by the excited state angular momentum density matrix ${}^{kl}f_{MM'}$ (Eq. (1)). In turn this density matrix allows to calculate the degree of circular polarization of the fluorescence from the ensemble of molecules and, as a consequence, to determine whether or not the ensemble of molecules possesses overall orientation.

Nevertheless, to carry out a simulation of the fluorescence circularity rate for a particular model situation we still need to find the energy splitting ${}^{kl}\Delta\omega_{MM'}$ of magnetic sublevels of excited state molecules in an external field and the wave function mixing coefficients $C^{(e)}_{kF'}$, $C^{(g)}_{jF''}$ entering equations (1, 2) respectively. The next section will describe how these quantities can be determined.

3 A molecule with HFS in an external magnetic field

The additional energy of a molecule with an electronic magnetic moment $\boldsymbol{\mu}_J$ and a nuclear magnetic moment $\boldsymbol{\mu}_I$ in an external magnetic field $\mathbf{B}$ can be written as

$$E_B = -\boldsymbol{\mu}_J\cdot\mathbf{B} - \boldsymbol{\mu}_I\cdot\mathbf{B}, \quad (8)$$

where the magnetic moments are connected with the respective angular moments $\mathbf{J}$ and $\mathbf{I}$ of a molecule

$$\boldsymbol{\mu}_J = -\frac{g_J\mu_B}{\hbar}\mathbf{J}, \qquad \boldsymbol{\mu}_I = -\frac{g_I\mu_0}{\hbar}\mathbf{I}. \quad (9)$$

We assume here that the Landé factor g for orbital motion of an electron is positive.

Molecular wave functions for a molecular rotational state with HFS created by one nucleus with nuclear spin quantum number I can be written as

$$|(JI)\,FM\rangle . \quad (10)$$

where F is the total angular momentum of the molecule with projection on the quantization axis z characterized by quantum number M.

The matrix elements of the respective Hamilton operator H_B can be written as

$$\begin{aligned} H_B &= \langle (JI)\,FM|\,E_B\,|(J'I)\,F'M'\rangle \\ &= \frac{g_J\mu_B}{\hbar}B\,\langle (JI)\,FM|\,\mathbf{J}\,|(J'I)\,F'M'\rangle \\ &\quad + \frac{g_I\mu_0}{\hbar}B\,\langle (JI)\,FM|\,\mathbf{I}\,|(J'I)\,F'M'\rangle \end{aligned} \quad (11)$$

where the operator in the first term acts only upon the electronic part of the wave function, but in the second term only upon the nuclei part of the molecular wave function.

Let us consider each term on the right-hand-side of (11) separately. In the $\langle (JI)\,FM|\,\mathbf{J}\,|(JI)\,FM\rangle$ operator acts only on the electronic part of the wave function. So, according to the Wigner-Eckart theorem [19,20], we have

$$\langle (JI)\,FM|\,J^0\,|(J'I)\,F'M'\rangle = (-1)^{F-M} \times \begin{pmatrix} F & 1 & F' \\ -M & 0 & M' \end{pmatrix} \langle (JI)\,F\|\,J^0\,\|(J'I)\,F'\rangle , \quad (12)$$

and the reduced matrix element can be expanded further

$$\langle (JI)F\|\,J^0\,\|(J'I)F'\rangle = (-1)^{J+I-F'+1}\sqrt{(2F+1)(2F'-1)} \times \begin{Bmatrix} J & F & I \\ F' & J' & 1 \end{Bmatrix} \langle J\|\,J^0\,\|J'\rangle . \quad (13)$$

For the last reduced matrix element we have

$$\langle J\|\,J^0\,\|J'\rangle = \sqrt{J(J+1)(2J+1)}\,\delta_{JJ'}. \quad (14)$$

If we collect all terms together we arrive at

$$\langle (JI)FM|\,J^0\,|(J'I)F'M'\rangle = (-1)^{J+I+F'-F-M+1} \times \sqrt{(2F+1)(2F'+1)J(J+1)(2J+1)} \times \begin{Bmatrix} J & F & I \\ F' & J' & 1 \end{Bmatrix} \begin{pmatrix} F & 1 & F' \\ -M & 0 & M' \end{pmatrix} \delta_{JJ'}. \quad (15)$$

In a similar way for second term we have

$$\langle (JI)\,FM|\,I^0\,\,(J'I)\,F'M'\rangle = (-1)^{J+I+F'-F-M+1} \times \sqrt{(2F+1)(2F'+1)I(I+1)(2I+1)} \times \begin{Bmatrix} I & F & J' \\ F' & I & 1 \end{Bmatrix} \begin{pmatrix} F & 1 & F' \\ -M & 0 & M' \end{pmatrix} . \quad (16)$$

Besides, as part of the diagonal elements we have ordinary HFS. Magnetic dipole HFS

$$H_m = a\frac{1}{2}\frac{A^2}{J(J+1)}\left[F(F+1) - J(J-1) - I(I+1)\right]. \quad (17)$$

a being a magnetic HFS constant, and the electric quadrupole HFS

$$H_q^{(0)} = b_0 \times \frac{[3-J(J+1)][3X(X+1)/4 - J(J-1)I(I+1)]}{(2J-1)J(J+1)(2J+3)2I(2I-1)} \quad (18)$$

b_0 being the usual (longitudinal) electric quadrupole HFS constant. In addition to this

$$H_q^{(2)} = \pm b_2 \frac{\sqrt{3/2}\,[3X(X+1)/4 - J(J+1)I(I+1)]}{(2J-1)(2J+3)2I(2I-1)} \quad (19)$$

must be considered for Π state [22–24], where the + sign stands for the e component and the − sign for f components. In these equations $X = F(F+1) - J(J+1) - I(I+1)$. The HFS constant b_2 may be called a transversal HFS constant, because it is associated with the transversal irreducible component of the electric field gradient.

Energies of molecular states in an external field can be obtained by a standard procedure by diagonalization of the Hamilton matrix defined above. Besides, in a process of matrix diagonalization the coefficients defining the expansion of the wave function of state in the field over the hyperfine state wave functions can be obtained as well.

4 Example for NaK

To make calculations for a real molecule and to find out how large the effect of alignment-orientation conversion can be for a real system, one must know certain molecular constants. In particular one must know the orbital Landé factor g_J and the nuclear Landé factor g_I in equation (11) as well as the molecular hyperfine constants a, b_0, b_2 entering equations (17–19). Unfortunately, at least some of these quantities are not known for most of the molecules in excited state.

Nevertheless, in many cases the necessary molecular constants can be easily estimated with good accuracy from the known properties of the nucleus and atomic constants. In this section we are going to demonstrate how it can be done. As an example, let us consider the very simple and widely studied molecule – NaK in its excited $D^1\Pi$ state. We chose this heteronuclear molecule, because, as it will be shown further, for this molecule the assumption that only one nucleus creates HFS can be justified with certain accuracy. Of course, calculations can be also performed accounting for influence of both nuclei, but this would make calculations unnecessary complicated and exceeds the limits of the present paper.

Let us start with Landé factors. The most accurate values of the gyromagnetic ratio for nuclei of interest in Bohr magnetons are $g_I = -0.000\,804\,610\,8(8)$ for ^{23}Na and $g_I = -0.000\,141\,934\,89(12)$ for ^{39}K [25]. This means that the magnetic moment of Na is almost six times larger than that of K. The electron Landé factor in molecular $^1\Pi$ state can easily be calculated as $g_J = 1/[J(J+1)]$ [26].

Let us continue with HFS constants. The magnetic HFS constant a can be calculated as

$$a = 2g_I\mu_B^2 \sum_n \left\langle \frac{1}{r^3} \right\rangle_{av}. \quad (20)$$

where g_I is the Landé factor of a nucleus causing the HFS.

Let us estimate the magnitude of magnetic HF splitting constants a for both nuclei of NaK. As pointed out as early as in [27], the average of $\langle r^{-3}\rangle_{av}$ is taken over only those electrons which form the angular momentum of a molecule.

We know that the molecular $D^1\Pi$ state at large internuclear distance correlates with atomic states 3^2P for Na and 4^2S for K [28]. It means that in this approximation the K does not contribute to the molecular electronic angular momentum. For the atomic orbital of Na an estimation of $\langle r^{-3}\rangle_{av}$ can be done using alkali atom wave functions. This leads to [19]

$$\frac{1}{r^3} = \frac{Z_a^2 Z_i}{n_*^3(l+1)(l+1/2)l}. \quad (21)$$

The parameters are $Z_a(\mathrm{Na}) = 1$, $n_*^3(\mathrm{Na}(3p)) = 2.12$, and $Z_i(\mathrm{Na}) = 7.59$ [19]. Obviously, all these numerical values of constants allow us to conclude that at first approximation we can neglect the magnetic nuclear splitting caused by K and deal only with the effect caused by one nucleus, namely Na.

A direct way, how to estimate the HFS constant a for Na is to calculate equations (20, 21), and we arrive at $a = 37.3$ MHz. This estimate for the molecular a_{mol} can be cross-checked using data that can be obtained directly from the atomic hyperfine spectrum. From [27] we know the connection between atomic a_{at} and molecular a_{mol} constants

$$a_{\mathrm{mol}} = a_{\mathrm{at}} \frac{j(j+1)}{l(l+1)}. \quad (22)$$

From [25] we know the atomic magnetic HFS constants for Na $3P_{1/2}$, being $a_{1/2} = 94.3$ MHz and for $3P_{3/2}$ $a_{3/2} = 18.69$ MHz. Making use of (22) we get from two atomic constants $a_{\mathrm{mol}} = 35.4$ MHz and $a_{\mathrm{mol}} = 35.0$ MHz respectively. For final check we can use an experimental value of $\overline{r^{-3}}$ given in [27] explicitly for Na p electrons as 1.65×10^{24} cm^{-3}. Using this directly in formula (20), we again get the very close numerical value $a = 34.5$ MHz. The level of coincidence of a values for the NaK molecule, as estimated by different approaches gives us confidence in the value obtained. This means that we can use further the a value around 35 MHz relatively safely.

The magnetic HFS constants b_0 and b_2 can be calculated according to the expressions $b_0 = eQq_{11}$ and $b_2 = eQq_{-11}$, where e is the electron charge, Q is the nucleus quadrupole moment, and $q_{\Lambda\Lambda}$ and $q_{\Lambda-\Lambda}$ are the longitudinal and transversal electric field gradients respectively. The electric field gradient components q_{ij} can be calculated according to [22, 24]

$$q_{\Lambda+\mu\,\Lambda} = 2N(-1)^{\mu}\langle -\Lambda-\mu|\,eC_{-\mu}^{(2)}(\theta,\varphi)/r^3\,|-\Lambda\rangle. \quad (23)$$

where N is the number of electrons, and Λ is a quantum number that represents the angular momentum projection on the internuclear axis.

At first approximation we can assume that the molecular orbital consists of two atomic orbitals centered on each nucleus. Besides, a p orbital is centered on the Na atom, but on the K atom s one.

For Na we can write

$$|\Lambda) = \psi_r(r)\, Y_{l\Lambda}(\theta, \varphi) \tag{24}$$

and, using an explicit form for the operator $C^{(2)}_{\mu}(\theta, \varphi) = \sqrt{4\pi/5} Y_{2\mu}(\theta, \varphi)$, we can immediately obtain

$$\begin{aligned} q_{\Lambda+\mu\,\Lambda} &= 2N(-1)^{\mu} e (\psi_r | r^{-3} | \psi_r) (Y_{l\,-\Lambda-\mu} | C^{(2)}_{-\mu} | Y_{l\,-\Lambda}) \\ &= 2N(-1)^{\mu} e\overline{r^{-3}} C^{l0}_{l020} C^{l\,-\Lambda+\mu}_{l\,-\Lambda\,2\,\mu}. \end{aligned} \tag{25}$$

The explicit form for Clebsch-Gordan coefficients allows us to have

$$q_{\Lambda\Lambda} = -\frac{2e}{5}\overline{r^{-3}}, \qquad q_{\Lambda-\Lambda} = -\sqrt{6}\frac{2e}{5}\overline{r^{-3}}. \tag{26}$$

An important point here is that the average $\overline{r^{-3}}$ for these calculations is over all electrons, not only those contributing to an electron angular momentum, as it was in the case of magnetic HFS.

For an s orbital it immediately follows from formulae presented above that $q_{\Lambda\Lambda} = q_{\Lambda-\Lambda} = 0$. This means that at first approximation we can assume again that in a HFS of NaK in $D^1\Pi$ state only the Na nucleus contributes and that the ratio between electric HFS constants related to longitudinal $q_{\Lambda\Lambda}$ and transversal $q_{\Lambda-\Lambda}$ components of the electric field gradient can be obtained from (26).

Most precise data on nuclear quadrupole moments are available from [29]. Namely, $Q(^{23}\mathrm{Na}) = +0.1006(20)$ b and $Q(^{39}\mathrm{K}) = +0.049(4)$ b. As far as for closed shell electrons we have the electric field gradient $q = 0$, probably for estimates within the same accuracy range as in a case of magnetic constants we can put numerical values of $\overline{r^{-3}}$ for p electrons obtained in case of a in formulae $b = eQq_{\Lambda\Lambda}$. This gives us a first approximation for $b_0 = 2.64$ MHz. This value should be close to the experimental one for the Na atom in ^{2}P state, as it actually is. For the Na atom we have $b = 2.90$ MHz [25].

5 Analysis of the observable signals

The analysis performed above allows as to assume that, at first approximation hyperfine splitting of NaK molecule is caused only by the Na nucleus, with little influence from the K nucleus. The following parameters determine the HFS splitting: nucleus spin of Na $I = 3/2$, Landé factor for the Na atom $g_J = 0.5$, $g_I = -0.0008$. Hyperfine constants-magnetic dipole $a = 35$ MHz, electric quadrupole $b_0 = 3$ MHz, $b_2 = \sqrt{6}b_0$. The excited state relaxation rate for NaK in $D^1\Pi_u$ state is equal to 5×10^7 s^{-1} [24,30]. Diagonalization of the Hamilton matrix for the $^1\Pi$ excited state rotational level $J = 1$ yields the magnetic sublevel energies as dependent on the external magnetic field strength, as depicted in Figure 1. All level crossings are real, because in a model considered only levels with coinciding angular projection M values mutually interact. For levels with the same M but different F it would be anticrossing, in case they came close in the energy scale.

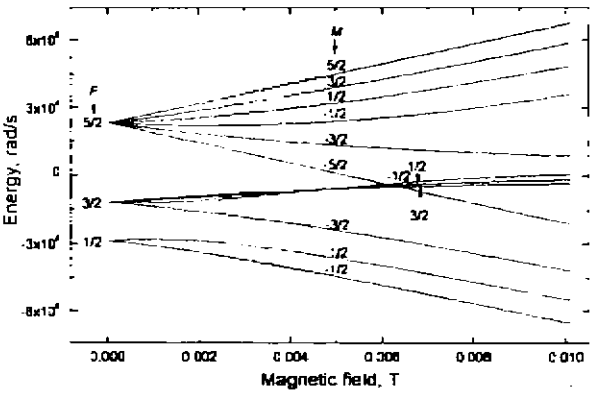

Fig. 1. HFS level splitting in an external magnetic field for excited molecular state with quantum numbers $J = 1$, $I = 3/2$. Other parameters see in the text.

The considered magnetic field region corresponds to a situation when the field is of an intermediate strength. For a very low field strength each hyperfine level experiences linear Zeeman effect. As the field strength increases, we are coming to the region when the Zeeman energy is close to the hyperfine splitting energy and we have an energy level pattern that is most complicated. If the field is increased further, we arrive at a region when we see normal Zeeman splitting again (linear Zeeman effect) but in this case not for a hyperfine level, but for a rotational level J with quantum number equal to 1. The obtained energy level pattern allows us to calculate observable signals. As demonstrated in [6], one may expect an orientation signal with largest amplitude, if molecules are excited with linearly polarized light, with the light electric field vector at the angle $\pi/4$ with respect to the external field direction – the z-axis. Let us assume $\theta = \pi/4$ and $\varphi = 0$. To have a most pronounced signal one must observe circular polarization of fluorescence in the xy-plane. In our calculation we assumed that fluorescence circularity as defined by equation (3) is measured in the direction characterized by the angles $\theta = \pi/2$, $\varphi = \pi/2$.

Let us consider two possible transition types $J''_{\mathrm{initial}} = 0 - J' = 1 - J''_{\mathrm{final}} = 0$ and $J''_{\mathrm{initial}} = 0 - J' = 1 - J''_{\mathrm{final}} = 2$, where the rotational quantum numbers of the initial, excited and final state are shown. For these two types of transition simulated signals are presented in Figure 2.

As it may be seen, the signals reveal a remarkable amplitude. We can obtain angular momentum orientation that leads to the fluorescence circularity of several percents. It must be considered as a circularity rate which can be measured easily on simple setups [7]. Another important feature is that these signals have different signs (different directions of angular momentum orientation)

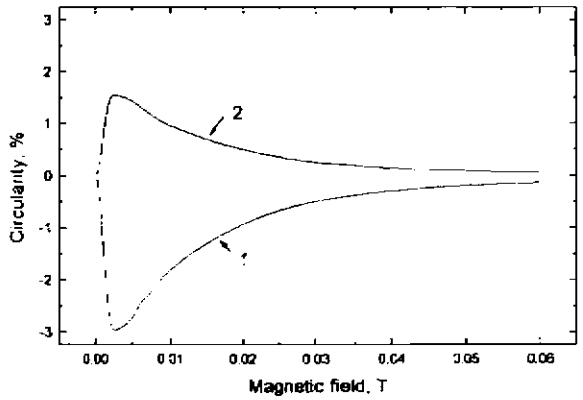

Fig. 2. Fluorescence circularity determined by an orientation of the excited state as dependent on the external magnetic field strength for two types of molecular transitions: 1 – $J''_{\text{initial}} = 0 \quad J' = 1 \quad J''_{\text{final}} = 0$ and 2 – $J''_{\text{initial}} = 0 \quad J' = 1 \quad J''_{\text{final}} = 2$.

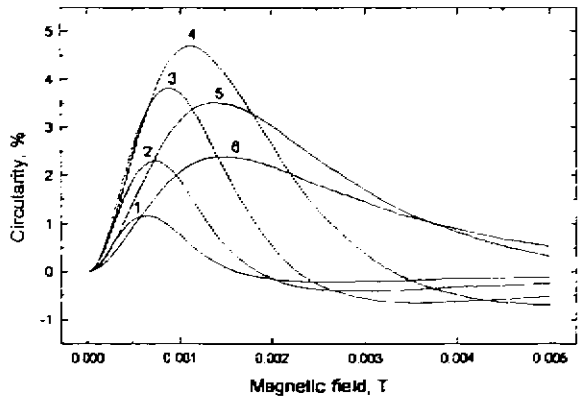

Fig. 3. Fluorescence circularity dependence on magnetic field strength for different values of magnetic hyperfine interaction constant a; 1 $a = 7$ MHz, 2 $a = 10$ MHz, 3 $a = 15$ MHz, 4 $a = 25$ MHz, 5 $a = 50$ MHz, 6 $a = 80$ MHz.

for different molecular transitions in the final stage of an excitation-fluorescence cycle.

As far as, in order to determine different properties of atoms and molecules fluorescence circularity rates are measured that are even smaller than expected due to hyperfine structure, one must be very careful in the analysis of the signals and keep this possible reason for appearance of fluorescence circularity in mind.

On the other hand, this effect can be exploited in itself to determine hyperfine constants of molecules. In order to demonstrate this, let us consider an even more simple situation than the one analyzed above. To make the signal dependent on just one parameter, let as assume that only one nucleus of a molecule has non-zero nuclear spin and that this spin is characterized by a quantum number $I = 1/2$. Then, in the same geometry as considered above for a molecular transition $J''_{\text{initial}} = 0 - J' = 1 - J''_{\text{final}} = 0$, we can calculate the circularity rate as dependent on the magnetic hyperfine constant a (values of Landé factors and relaxation rate are assumed the same as in the previous example). In Figure 3 one can see the signal as dependent on the magnetic hyperfine constant a. This dependence is well pronounced and obviously can be used for measurements of a.

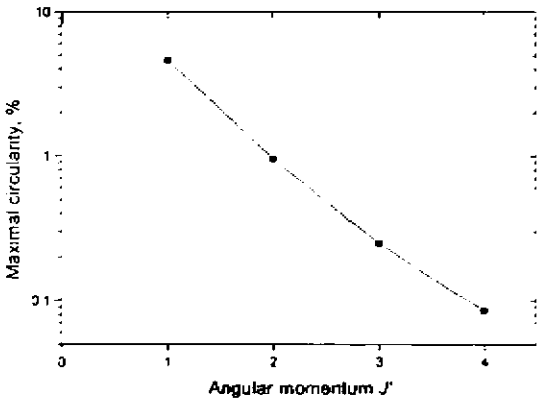

Fig. 4. Maximal fluorescence circularity dependence on the excited state rotational quantum number J'.

An important question is, how the magnitude of the circularity signal is dependent on the excited state angular momentum value. Obviously, the effect must decrease when the excited state angular momentum increases. This follows from a simple model. The total angular momentum F of a molecules is formed by a coupling between the rotational angular momentum J and the nucleus spin angular momentum I. In a magnetic field this coupling breaks down and the total angular momentum F ceases to exist as a good quantity. Instead the rotational angular momentum J starts playing the dominant role. If J, F and I are of the same magnitude, transition form F to J can considerably influence the signal. This is what we see in the examples above. If, on the contrary, J is considerably larger than I, then the total and rotational angular momenta almost coincide, and transition from F to J influences observable signals only insignificantly. In Figure 4 the maximal circularity amplitude for a transition $J''_{\text{initial}} = J - 1 \rightarrow J' = J \rightarrow J''_{\text{final}} = J - 1$ is depicted as dependent on J. For this calculation the value of a magnetic hyperfine constant is assumed as $a = 25$ MHz. Other parameters are as for Figure 3. We can see that the amplitude of the signal decreases almost exponentially with increase in J. This means that the influence of hyperfine structure on the observed signals can be significant only for very small angular momentum values.

We have considered here a simplified situation when only one nucleus causes HFS of a molecule. In the case when two or more nuclear spins are influencing the magnetic sublevel pattern in a magnetic field and consequently the fluorescence signal, the analysis can be performed as well. For this methods have been developed, see for example [27]. Unfortunately, these calculations are rather laborious.

6 Conclusions

From the discussion above the following conclusions may be drawn. First, when one measures alignment-orientation

conversion in presence of an external magnetic field, one must be very careful in the signal analysis. Besides, the non-linear effects of a type discussed in references [10, 16], for which intramolecular perturbations are responsible, similar appearances in experimentally measured circularity rate can be caused by a hyperfine structure which is present almost in all atoms and molecules. The circularity rate caused by a joint action of an external magnetic field and hyperfine interaction can have an amplitude comparable with, if not larger than some features in fluorescence circularity dependence on the magnetic field strength, as observed in experiment and attributed to a specific intramolecular interaction, see [16]. Of course, as shown above, the last conclusion is relevant only for molecular states with small rotational angular momentum, and this was not the case in the experiment cited above.

On the other hand, alignment-orientation transition can be used for good at certain conditions, in measuring hyperfine interaction constants in molecules as well as in atoms. Despite the fact that in the model analyzed above molecules were used as an example, all description could be applied to atoms as well.

Besides, in this paper some relations between atomic and molecular hyperfine structure constants on the one hand, and between constants a, b_0 and b_2 in molecules on the other, have been discussed. This approach can allow to make estimates of necessary molecular hyperfine interaction constants in the cases when only respective atomic constants are available.

References

1. M. Lombardi, C.R. Acad. Sci. B **265**, 191 (1967).
2. V.N. Rebane, Opt. Spectrosc. USSR **51**, 163 (1968).
3. M. Lombardi, in *Beam Foil Spectroscopy*, edited by I.A. Sellin, D.J. Pegg (Plenum Press, New York, 1976), Vol. 2, p. 731.
4. T. Manabe, T. Yabuzaki, T. Ogawa, Phys. Rev. Lett. **46**, 637 (1981).
5. M. Lombardi, J. Phys. France **30**, 631 (1969).
6. M. Auzinsh, R. Ferber, J. Chem. Phys. **99**, 5742 (1993).
7. M. Auzinsh, R. Ferber, *Optical Polarization of Molecules* (Cambridge University Press, Cambridge UK, 1995).
8. M. Auzinsh, Can. J. Phys. **75**, 853 (1997).
9. M. Auzinsh, R. Ferber, Phys. Rev. Lett. **69**, 3463 (1992).
10. O. Nikolayeva, M. Auzinsh, M. Tamanis, R. Ferber, J. Mol. Spectr. **480–481**, 283 (1999).
11. J.C. Lehmann, J. Phys. France **25**, 809 (1964).
12. J.C. Lehmann, Phys. Rev. **178**, 153 (1969).
13. M. Broyer, J. Vigué, J.-C. Lehmann, Chem. Phys. Lett. **22**, 313 (1973).
14. J. Vigué, M. Broyer, J.-C. Lehmann, J. Phys. B **7**, L158 (1974).
15. J. Vigué, M. Broyer, J.-C. Lehmann, J. Chem. Phys. **62**, 4941 (1975).
16. I. Klintsare, M. Tamanis, A.V. Stolyarov, M. Auzinsh, R. Ferber, J. Chem. Phys. **99**, 5748 (1993).
17. M. Auzinsh, A.V. Stolyarov, M. Tamanis, R. Ferber, J. Chem. Phys. **105**, 37 (1996).
18. M. Tamanis, M. Auzinsh, I. Klincare, O. Nikolayeva, A.V.Stolyarov, R. Ferber, J. Chem. Phys. **106**, 2135 (1997).
19. I.I. Sobelman, *Atomic Spectra and Radiative Transitions* (Springer-Verlag, Berlin, 1979).
20. D.A. Varshalovich, A.N. Moskalev, V.K. Khersonskii, *Quantum Theory of Angular Momentum* (World Scientific, Singapore, 1988).
21. M.-A. Melieres-Marechal, M. Lombardi, J. Chem. Phys. **61**, 2600 (1974).
22. K.F. Freed, J. Chem. Phys. **45**, 4214 (1966).
23. J. Bulthuis, J.M. Milan, H.M. Jassen, S. Stolte, J. Chem. Phys. **94**, 1781 (1991).
24. M. Tamanis, M. Auzinsh, I. Klincare, O. Nikolajeva, R. Ferbers, E.A. Pazyuk, A.V. Stolyarov, A. Zaitsevskii, Phys. Rev. A **58**, 1932 (1998).
25. E. Arimondo, M. Inguscio, P. Violino, Rev. Mod. Phys. **49**, 31 (1977).
26. G. Herzberg, *Molecular Spectra and Molecular Structure I. Spectra of Diatomic Molecules* (D. van Nostrand Company, Princeton, New Yersey, Toronto, London, 1957).
27. C.H. Townes, A.L. Schawlow, *Microwave Spectroscopy* (Dover Pubns, Dover, 1975).
28. W.J. Stevens, D.D. Konowalow, L.B. Ratcliff, J. Chem. Phys. **80**, 1215 (1984).
29. P. Raghavan, A. Data Nucl. Data Tables **42**, 189 (1989)
30. J. Pfaff, M. Stock, D. Zevgolis, Chem. Phys. Lett. **65**, 310 (1979)

dis 2

Angular-momentum spatial distribution symmetry breaking in Rb by an external magnetic field

Janis Alnis and Marcis Auzinsh*
Department of Physics, University of Latvia, 19 Rainis blvd., Riga LV-1586, Latvia
(Received 26 July 2000; published 16 January 2001)

Excited-state angular-momentum alignment–orientation conversion for atoms with hyperfine structure in the presence of an external magnetic field is investigated. Transversal orientation in these conditions is reported. This phenomenon occurs under Paschen Back conditions at intermediate magnetic-field strength. Weak radiation from a linearly polarized diode laser is used to excite Rb atoms in a cell. The laser beam is polarized at an angle of $\pi/4$ with respect to the external magnetic-field direction. Ground-state hyperfine levels of the $5S_{1/2}$ state are resolved using laser-induced fluorescence spectroscopy under conditions for which all excited $5P_{3/2}$ state hyperfine components are excited simultaneously. Circularly polarized fluorescence is observed to be emitted in the direction perpendicular to both to the direction of the magnetic field B and direction of the light polarization E. The obtained circularity is shown to be in quantitative agreement with theoretical predictions.

DOI: 10.1103/PhysRevA.63.023407 PACS number(s): 32.80.Bx, 32.10.Fn

I. INTRODUCTION

In the absence of external forces an ensemble of unpolarized atoms can only be aligned [1] by linearly polarized light. The fact that the atoms are only aligned implies that, although the magnetic sublevels of different $|m_J|$ are populated unequally, magnetic sublevels of $+m_J$ and $-m_J$ are equally populated. For this reason, atoms excited by linearly polarized laser radiation are not expected to produce circularly polarized fluorescence. In the presence of external forces, however, excitation by linear polarized light can produce an orientated population of atoms (with different $+m_J$ and $-m_J$ populations). This effect, called alignment-orientation conversion, was predicted and experimentally observed in the late 1960's in the anisotropic collisions of initially aligned atoms [2–5]. Later an electric field was also shown to induce alignment–orientation conversion [6]. Electric-field-induced alignment–orientation conversion has since been studied in great detail [7].

Contrary to the case of an electric field, linear perturbation by a magnetic field is not able to orient an initially aligned angular momentum distribution. This inability to induce alignment–orientation conversion is a result of the reflection symmetry of axial vector fields. This symmetry can be broken if, in addition to the linear Zeeman effect, there exists nonlinear dependencies of the magnetic sublevel energies on the field intensity and the magnetic quantum numbers m_J. Such nonlinear perturbations can have a variety of causes including predissociation [8–11] and hyperfine interaction. Alignment-orientation conversion as a result of hyperfine interaction in a magnetic field in context of nuclear spin $I=1/2$ was studied by Lehmann for the case of optically pumped cadmium in a magnetic field [12,13]. Baylis described the same effect in sodium [14]. The first experiment to detect directly a net circular polarization of fluorescence from an initially aligned excited state in an external magnetic field was reported by Krainska-Miszczak [15]. In this work the optical pumping of ^{85}Rb by a π-polarized D_2 line was studied. This effect was also examined by Han and Schinn in sodium atoms [16]. They describe this alignment-orientation conversion process as resulting from hyperfine-F-level mixing in an external magnetic field and the interference of different excitation–decay pathways in such mixed levels.

In all above cases, a joint action of the magnetic field and hyperfine interaction creates different population of magnetic sublevels $+m_F$ and $-m_F$ of hyperfine levels F. This means that *longitudinal* orientation of atoms along the direction of an external magnetic field is created. Recently it was predicted that joint action of a magnetic field and hyperfine interaction from an initially aligned ensemble would create *transverse* orientation of angular momentum of atoms or molecules [17]. Transverse orientation implies orientation in a direction perpendicular to the external magnetic field **B**. In this particular case magnetic sublevels $+m_F$ and $-m_F$ are equally populated, but orientation is a result of coherence between pairs of wave functions of magnetic sublevels m_F with $\Delta m_F=1$. Creation of transverse orientation is achieved if the excitation light polarization vector is neither parallel nor perpendicular to the external magnetic field direction with the largest effect occurring for the case of a light polarization–magnetic field angle of $\pi/4$. In a previous paper [17], parameters of the NaK molecule were used for numerical simulations of orientation and fluorescence circularity signals. We found that transverse orientation only occurred when the rotational angular momentum J is small enough to be comparable with the nuclear spin I. For levels with larger angular-momentum quantum number, the magnitude of created orientation was found to decrease rapidly.

Previously transverse alignment-orientation conversion was studied in detail for the case of an external electric field [7]. In this case the conversion occurs with or without hyperfine interaction. In this article we report the first experimental observation to our knowledge of alignment–orientation conversion that creates net transverse orientation of atoms with hyperfine structure in an external magnetic field. As we will show, this effect is interesting not only as a

*Corresponding author. E mail address: mauzins@latnet.lv

new way to create orientated atoms, but also can be used to increase the accuracy with which constants related to the hyperfine interaction can be determined.

II. THEORETICAL DESCRIPTION

The general scheme how transverse orientation of angular momentum is created from an aligned ensemble of atoms is the following: Initial alignment, for example by absorption of a linearly polarized light, is created at some nonzero acute angle with respect to the direction of an external-field (in this case a **B** field). The optimum angle is $\pi/4$, but the effect will take place at any angle that differs from 0 and $\pi/2$. The perturbing field together with the hyperfine interaction causes unequally spaced magnetic sublevel splittings. Under these conditions, angular-momenta orientation at the direction perpendicular to the direction of the external field is created [22]. A semiclassical interpretation of this effect in terms of angular momentum precession in an external field can be found in a previous publication [7]. In this vectorial model, alignment–orientation conversion is the result of a different precession rate for different orientations of angular momentum with respect to the external field. In what follows we explain this transverse-orientation in terms of a accurate quantum mechanical model.

In the present study we exploit laser excitation of pure isotopes of Rb atoms from their ground state $5S_{1/2}$ to the first excited state $5P_{3/2}$ (resonance D_2 line) (see inset Fig. 5). The two most common naturally occurring isotopes of Rubidium are ^{85}Rb (72.15%, nuclear spin $I=5/2$) and ^{87}Rb (27.85%, nuclear spin $I=3/2$). As a result of hyperfine interactions, the ground-state level of ^{85}Rb is split into components with total angular momentum quantum numbers $F_i=2$ and $F_i=3$ and the ground-state level of ^{87}Rb is split into components with total angular momentum quantum numbers $F_i=1$ and 2. The ground-state-level splittings for ^{85}Rb and ^{87}Rb are approximately 3 and 6 GHz, respectively. In contrast, the four excited-state hyperfine components are separated by only several hundred MHz (see Figs. 1 and 3).

Excited-state hyperfine structure in absorption is not resolved due to Doppler broadening and laser-frequency jittering. To make an accurate signal modeling assuming broad line excitation, laser frequency is modulated by a few hundred MHz superimposing a 10 kHz sine wave on laser current. This allows accurate modeling to be done assuming that the excitation radiation is broad enough to excite all hyperfine components of the excited state without frequency selection, yet narrow enough to completely resolve the two ground-state components.

Magnetic field caused mixing takes place between sublevels with different total angular momentum F_e, but with identical magnetic quantum numbers m_F. Only levels of identical m_F mix because, as far as the magnetic field possesses axial symmetry, the magnetic quantum number m_F remains a good quantum number. However, levels of different F_e mix because an intermediate strength magnetic field partially decouples the electronic angular momentum J_e and nuclear spin I. As a consequence F_e ceases to be a good quantum number. The fact the m_F remains a good quantum number

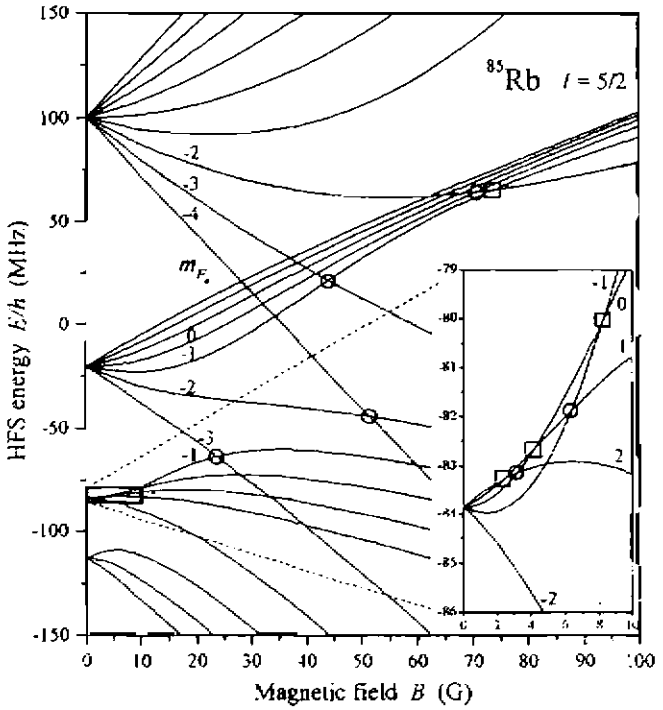

FIG. 1. Hyperfine structure energy-level diagram of ^{85}Rb $5p^2P_{3/2}$ in an external magnetic field. Symbols $\overline{-}$ indicate $\Delta m_{F_e}=1$ level crossings, ○ indicate $\Delta m_{F_e}=2$ level crossings.

whereas F_e does not is important to the interpretation of the data.

A convenient way to describe excited state atoms is by means of a quantum density matrix $^{kl}f_{mm'}$ [18]. Upper indices characterize atomic states in a magnetic field. In the weak field limit these states correspond to hyperfine levels F_e. Lower indices characterize magnetic quantum numbers. We consider an atom possessing the hyperfine structure which is placed in an external magnetic field. We further assume that this atom absorbs laser light polarized in the direction characterized by light electric field vector $\mathbf{E}_{exc}$. In this situation the density matrix that characterizes coherence between magnetic sublevels with quantum numbers m and m' is given as [21]

$$^{kl}f_{mm'}=\frac{\Gamma_p}{\Gamma-i^{kl}\Delta\omega_{mm'}}\sum_{j\mu}\langle\gamma_k m|\hat{\mathbf{E}}^*_{exc}\cdot\hat{\mathbf{D}}|\eta_j\mu\rangle \times\langle\gamma_l m'|\hat{\mathbf{E}}^*_{exc}\cdot\hat{\mathbf{D}}|\eta_j\mu\rangle^*. \quad (1)$$

Here Γ_p is a reduced absorption rate, Γ is the excited-state relaxation rate and $^{kl}\Delta\omega_{mm'}=(^{\gamma_k}E_m-^{\gamma_l}E_{m'})/\hbar$ is the energy splitting of magnetic sublevels m and m' belonging to the excited-state levels k and l. Magnetic quantum numbers of the ground-state level η_j are denoted by μ and magnetic quantum numbers of the excited-state level γ_k by m and m'.

In an external magnetic field, ground- and excited-state levels η_j and γ_k are not characterized by a total angular momentum quantum numbers F_i and F_e, but are instead mixtures of these states:

$$|\gamma_k m\rangle = \sum_{F_e=J_e-I}^{F_e=J_e+I} C^{(e)}_{kF_e} |F_e, m\rangle,$$
$$|\eta_j \mu\rangle = \sum_{F_i=J_i-I}^{F_i=J_i+I} C^{(i)}_{jF_i} |F_i, \mu\rangle. \quad (2)$$

The wave-function-expansion coefficients $C^{(e)}_{kF_e}, C^{(i)}_{jF_i}$ represent the mixing of field free hyperfine state wave functions by the magnetic field. These expansion coefficients along with the magnetic sublevel energy splittings ${}^{kl}\Delta\omega_{mm'}$ can be obtained by a standard procedure of diagonalization of a Hamilton matrix that contains both the diagonal hyperfine elements and the off-diagonal magnetic field interaction elements (see for example [17]).

There are several methods how to tell whether or not a particular atomic state described by a density matrix (1) possesses orientation. One possibility is to expand this matrix over the irreducible tensorial operators. Then those expansion coefficients can directly be attributed to the alignment and orientation of the atomic ensemble [18–20]. Alternatively, one may calculate directly the fluorescence circularity rate in spontaneous transitions from a particular excited state of an atom:

$$C = \frac{I(\mathbf{E}_{right}) - I(\mathbf{E}_{left})}{I(\mathbf{E}_{right}) + I(\mathbf{E}_{left})}. \quad (3)$$

Observed circularity of the fluorescence in a specific direction can differ from zero only for the case that the ensemble of atoms possesses overall orientation in this direction [18]. $I(\mathbf{E}_{right})$ and $I(\mathbf{E}_{left})$ are intensities of two fluorescence components with opposite circularity. We choose to calculate this expected circularity rate because it is the experimental measure used to register the appearance of orientation in an ensemble of atoms (see for example [22]).

We consider the case that spontaneous emission is detected without hyperfine state resolution. The intensity of the fluorescence with definite polarization characterized by a vector $\mathbf{E}_f$ in a spontaneous transition from an excited state J_e characterized by a set γ_k of levels in an external field to the ground state J_i characterized by a set η_j of levels can be calculated according to a previous work [21] as

$$I(\mathbf{E}_f) = I_0 \sum_{mm'\mu} \sum_{klj} \langle \gamma_k m|\hat{\mathbf{E}}_f^* \cdot \hat{\mathbf{D}}|\eta_j \mu\rangle \times \langle \gamma_l m'|\hat{\mathbf{E}}_f^* \cdot \hat{\mathbf{D}}|\eta_j \mu\rangle^* {}^{kl}f_{mm'}. \quad (4)$$

To find the circularity rate C, one needs to not only determine the matrix elements appearing in (1) and (4), but also the hyperfine level splitting and magnetic sublevel mixing coefficients. In Fig. 1 the hyperfine energy level splitting of the first excited state $5P_{3/2}$ for ^{85}Rb is presented. In these calculations the following published [23] hyperfine splitting constants and magnetic moment for the rubidium atom in its first excited state are used: $a = 25.009$ MHz, $b = 25.83$ MHz, $g_J = -1.3362$, $g_I = 0.000\,293$.

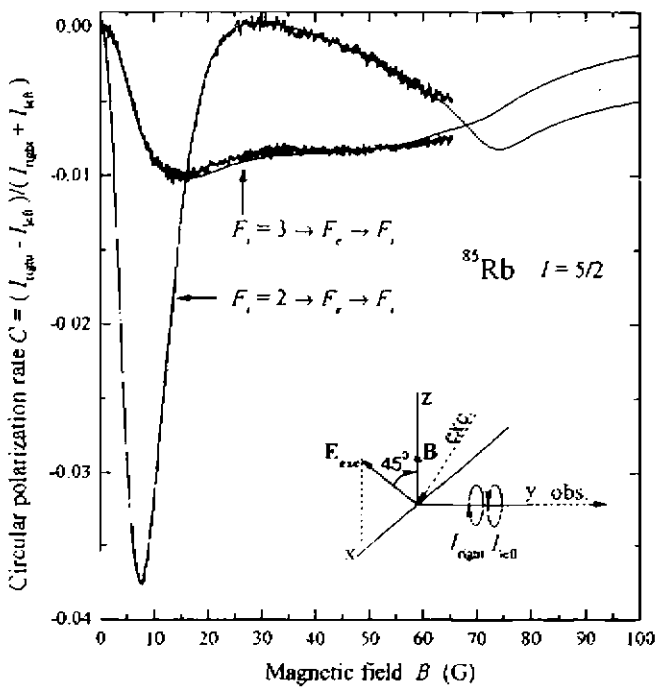

FIG. 2. Numerically simulated (smooth line) and experimentally measured (signal with noise) level crossing signals in fluorescence circularity for ^{85}Rb in conditions of alignment-orientation conversion and production of transversal orientation.

In Fig. 1 level crossing positions for magnetic sublevels with $\Delta m_{F_e} = 2$ are indicated by circles and crossings with $\Delta m_{F_e} = 1$ by squares. At values of magnetic field strength for which coherently excited magnetic sublevels undergo a level crossing, ${}^{kl}\Delta\omega_{mm'} = 0$, the prefactor appearing in Eq. (1) becomes large. This leads to resonance behavior of the observed signal. For case of excitation with linearly polarized light, the intensity of the resonance depends upon the angle between polarization direction of the laser light and external magnetic field direction. If the angle between these directions is 0, different magnetic sublevels are differently populated but no coherence is created in the ensemble. If the angle is $\pi/2$, coherence is created between magnetic sublevels with $\Delta m_{F_e} = 2$. If the angle differs form 0 and $\pi/2$, then magnetic sublevels with $\Delta m_{F_e} = 1$ and 2 [22] are excited coherently. This $\Delta m_{F_e} = 1$ coherence is required for transverse orientation.

We now consider the fluorescence circularity enhancement due to $\Delta m_{F_e} = 1$ level crossing for the case that the linear polarization and external field meet at an angle of $\pi/4$ (inset Fig. 2). The circularity C is calculated assuming an excited-state relaxation rate [24] $\Gamma = 3.8 \times 10^7$ s^{-1} and observation along an axis normal to the plain containing the external field $\mathbf{B}$ and the polarization vector $\mathbf{E}_{exc}$. The smooth lines of Fig. 2 give the expected signals for both resolved absorption lines. Both signals are maximum at an approximate magnetic field strength of 10 G. For both absorption lines we calculate a total fluorescence circularity with unresolved hyperfine components in a transition back to the ground state $5S_{1/2}$. The resonance peak is more pro-

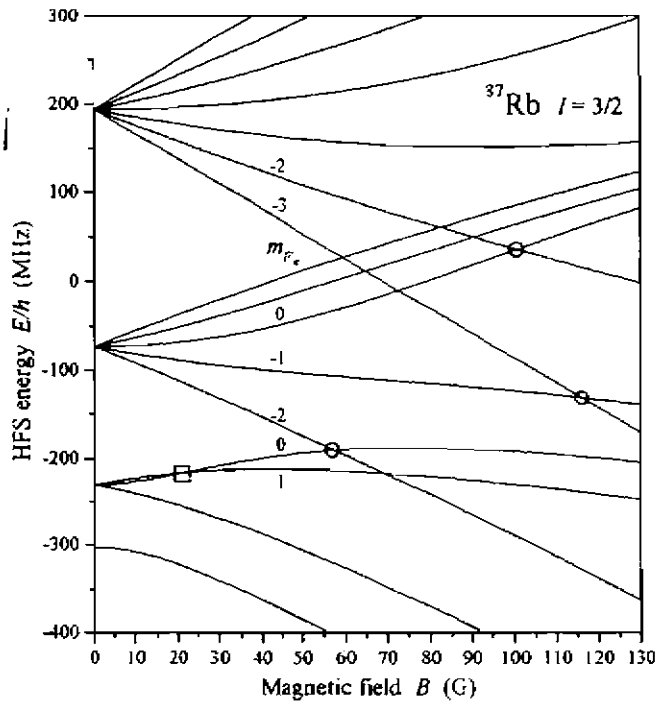

FIG. 3. Hyperfine structure energy-level diagram of ^{87}Rb $5p^2P_{3/2}$ state in an external magnetic field. Symbols $\square$ indicate $\Delta m_{F_e} = 1$ level crossings, and $\bigcirc$ indicate $\Delta m_{F_e} = 2$ level crossings.

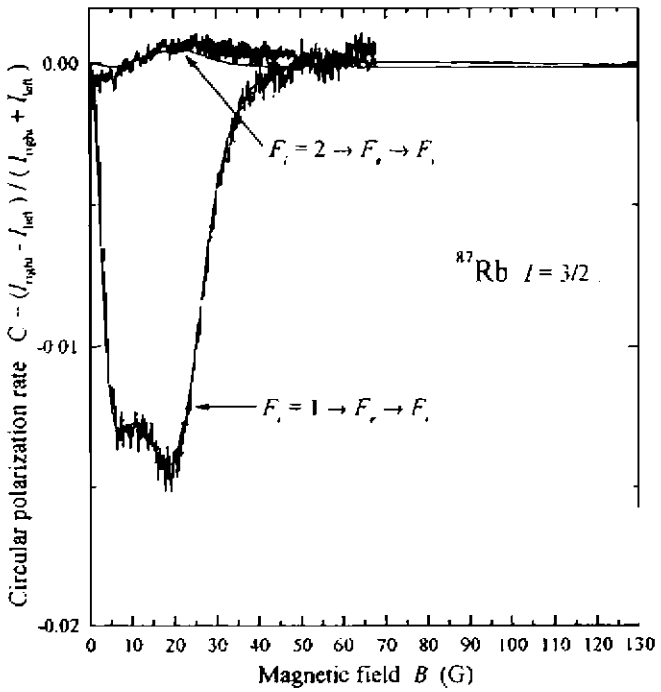

FIG. 4. Numerically simulated (smooth line) and experimentally measured (signal with noise) level crossing signals in fluorescence circularity for ^{87}Rb in conditions of alignment–orientation conversion and production of transversal orientation.

nounced for the $F_i = 2 \rightarrow F_e$ absorption transition than for the $F_i = 3 \rightarrow F_e$ transition.

Because a 10 G field is weak enough not to cause substantial hyperfine level mixing (i.e., the magnetic sublevel splitting in the magnetic field still is small in comparison with hyperfine splitting), the increase in orientation for $F_i = 2$ absorption can be understood using the relative transition probability $W_{F_i \rightarrow F_e}$ given by Sobelman [20]:

$$W_{F_i \rightarrow F_e} = (2F_i + 1)(2F_e + 1)(2J_i + 1)(2J_e + 1) \times \begin{Bmatrix} J_i & F_i & I \\ F_e & J_e & 1 \end{Bmatrix}^2 \begin{Bmatrix} L_i & J_i & S \\ J_e & L_e & 1 \end{Bmatrix}^2. \quad (5)$$

Here J_i, J_e and L_i, L_e are quantum numbers of total and orbital electronic angular momentum of the initial and final atomic state and S is the electronic spin of the atomic state. Quantities in curled brackets are 6-j symbols. This expression predicts that the $F_i = 2 \rightarrow F_e = 2$ absorption contributes 39% of the total allowed ($\Delta F = 0, \pm 1$) absorption from $F_i = 2$. In contrast, the $F_i = 3 \rightarrow F_e = 2$ absorption contributes only 8% of the total allowed ($\Delta F = 0, \pm 1$) absorption from $F_i = 3$. At the same time the $F_e = 2$ state is the state for which the magnetic sublevels undergo a level crossing in the vicinity of a 10 G magnetic field. Thus the absorption from the $F_i = 2$ state leads to a greater degree of transverse orientation.

Similar level splitting diagrams (Fig. 3) and expected circularity signals (Fig. 4) are calculated also for rubidium isotope ^{87}Rb. In this case the following atomic constants are used: $I = 3/2$, $a = 84.845$ MHz, $b = 12.52$ MHz, $g_J = -1.3362$, $g_I = -0.000\,995$ [23].

III. EXPERIMENT

In our experiment we use isotopically enriched rubidium (99% of ^{85}Rb) contained in a glass cell at room temperature to keep atomic vapor concentration low and avoid reabsorption. The $5s^2S_{1/2}$ to $5p^2P_{3/2}$ transition at 780.2 nm is excited using a temperature- and current-stabilized single-mode diode laser (Sony SLD114VS). Absorption signal is measured using a photodiode. As the laser frequency is swept using a ramped current drive, two absorption peaks with half-width of about 600 MHz separated by ~3 GHz appear due to the ^{85}Rb ground-state hyperfine structure. Absorption lines at 60 G broaden by less than 10%. The excited-state hyperfine structure is not resolved under the Doppler profile and introduced laser-frequency jittering. The laser line width without jittering is about 60 MHz. To avoid optical pumping and other nonlinear effects, neutral density filters are used to reduce the laser intensity.

During the level crossing and circularity measurements, the laser wavelength is stabilized on one of the two absorption peaks. Fluorescence is monitored on an axis normal to the electric vector $\mathbf{E}_{exc}$ and external magnetic field $\mathbf{B}$. A two-lens system is used to image the fluorescence on a photodetector containing a 3×3 mm photodiode (Hamamatsu S1223-01) and a transimpedance amplifier. A rotating ($f = 240$ Hz) sheet polarizer is inserted between the lenses. The photodetector signal is fed to a lock-in amplifier (Femto

LIA-MV-150) that measures the intensity difference of two orthogonal linearly polarized fluorescence components. A magnetic field of up to 65 G is produced by passing current through a pair of Helmholz coils 20 cm in diameter. The uncertainty of the magnetic field is estimated to ± 0.3 G. The sweep time is 5 s and 256 sweeps are averaged on an IBM compatible computer with a National Instruments data acquisition card. A lock-in time constant of 10 ms is used. Several adjustments are made to record symmetrical level crossing signals while sweeping the magnetic field in opposite directions. First, a linear polarizer is placed in a laser beam before the rubidium cell to fine adjust the laser polarization. Second, the lock-in phase is adjusted and, third, the Earth magnetic field components are compensated with additional Helmholz coils.

To detect circularly polarized light the gain electronics are first adjusted so that the linear polarization signals are symmetrical in opposite magnetic field directions. A $\lambda/4$ wave plate is then placed before the polarizer so that right- and left-handed circularly polarized light components are converted to orthogonal linear polarizations. It is checked that circularity signal at $B=0$ is zero. During the circularity measurements the magnetic field is swept alternatively in one and another direction and both traces are averaged. The experimentally recorded signal actually is $I(\mathbf{E}_{right})-I(\mathbf{E}_{left})$ and not the ratio $[I(\mathbf{E}_{right})-I(\mathbf{E}_{left})]/[I(\mathbf{E}_{right})+I(\mathbf{E}_{left})]$. Numerical simulations reveal that these two signals have almost the same shapes, the relative difference is less than 3%. Experimentally recorded signals are scaled vertically to fit the calculated ones.

Figures 2 and 4 compare experimentally obtained circularity to the theoretical ones. After the scaling factor to the experimental signal is applied (no other adjustable parameters are used) an excellent agreement between theoretical predictions and experimental signals can be observed. For both isotopes circularity signals with amplitude of several percent are measured.

In case of the measurements with ^{87}Rb, another cell was used that contained isotopically enriched ^{87}Rb (99%). For this isotope the signal starting from $F_i=1$ exhibits stronger resonance circularity than the one starting from the $F_i=2$ ground state. The reason for this is the same as already discussed in Sec. II for the ^{85}Rb isotope. Only in this case the excited-state hyperfine component $F_e=1$ undergoes level crossings with $\Delta m_{F_e}=\pm 1$. This resonance intensity ratio for two measured signals reflects the general situation that transitions with $\Delta F=0$ are more intense than transitions with $\Delta F=\pm 1$.

IV. COMPARISON OF CIRCULARITY MEASUREMENTS TO OTHER LEVEL-CROSSING MEASUREMENTS

In previous studies, atoms are excited by a linearly polarized light with $\mathbf{E}_{exc}$ vector perpendicular to an external magnetic field. The fluorescence emitted along the magnetic field is then detected. Fluorescence linear polarization as a function of magnetic field is measured. Here we repeat this experiment for the case of ^{85}Rb (see inset of Fig. 5). Two signals are numerically simulated and experimentally recorded, the first one when absorption occurs on the transitions ($F_i=2\rightarrow F_e$) and the second one for a ($F_i=3\rightarrow F_e$) absorption transition. In both cases the conditions are maintained so that the excited-state hyperfine levels are not resolved. For the first absorption transition in the absence of the magnetic field electric dipole transitions are allowed only to the levels $F_e=1$, 2, and 3. For the second absorption transition in absence of the external field hyperfine components with $F_e=2$, 3, and 4 can be excited.

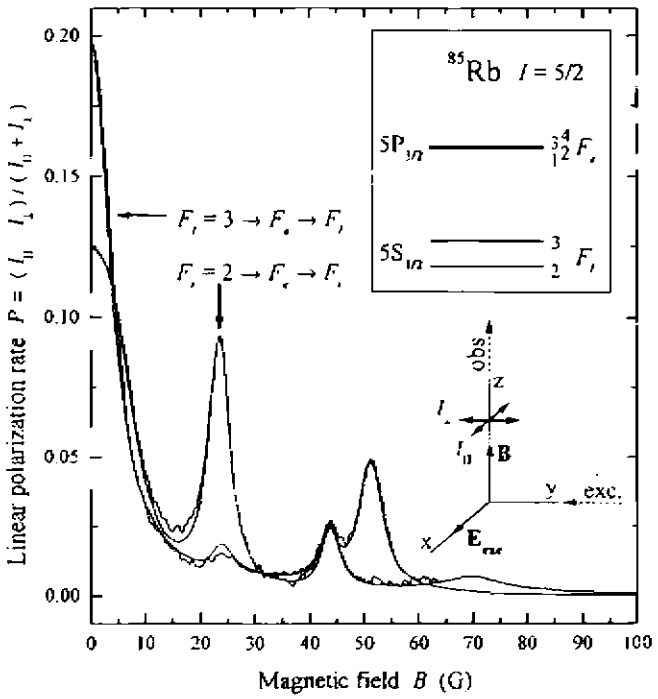

FIG. 5. Numerically simulated (smooth line) and experimentally measured (signal with noise) level crossing signals in linearly polarized fluorescence for ^{85}Rb.

In the presence of the magnetic field selection rules change substantially. As it was mentioned before, F_e is no longer a good quantum number. Each hyperfine level in the presence of external field is mixed together with others. As far as m_{F_e} remains a good quantum number in the presence of the external field, only components with the same m_{F_e} are mixed. This implies that for the present example of ^{85}Rb, magnetic sublevels with $m_{F_e}=4$ and -4 at any field value are unmixed because only $F_e=4$ contains such sublevels and there is no counterpart for these states to be mixed with. In the case of $m_{F_e}=3$ and -3 only two magnetic sublevels originating from $F_e=3$ and 4 are mixed together, etc. This means that magnetic sublevels $m_{F_e}=0,\pm 1$ in the external field are composed from $F_e=1,2,3,4$ components, $m_{F_e}=\pm 2$ from $F_e=2,3,4$ components, $m_{F_e}=\pm 3$ from $F_e=3,4$ components, but $m_{F_e}=\pm 4$ contain only one component $F_e=4$.

In Fig. 1 we can see several $\Delta m_{F_e}=2$ magnetic sublevel crossings. The first crossing takes place at zero magnetic field when all magnetic sublevels belonging to the same hy-

perfine level have the same energy. This crossing is the zero field level crossing. Because all magnetic sublevels belonging to the same hyperfine state cross at zero field, the zero field level crossing leads to the largest resonance amplitude. Then subsequent crossings take place at approximately 2.4, 4.2, 8.2, 24, 44, 52, and 74 G magnetic field strength. A resonant peak occurs on both linear polarization signals for almost every one of these level crossings, although with differing amplitudes (see the Fig. 5). There is one exception. The strong resonance peak at 52 G that is present in the $F_i=3\rightarrow F_e$ signal is missing in the $F_i=2\rightarrow F_e$ signal. This seeming inconsistency can be easily explained. This resonance appears when the magnetic sublevels $m_{F_e=4}=-4$ and $m_{F_e=3}=-2$ are crossing. But as it was mentioned due to dipole transition selection rules that the $m_{F_e=4}=-4$ level can not be excited from $F_i=2$ and this restriction can not be removed by external field because $m_{F_e=4}=-4$ remains unmixed at any field strength.

In Fig. 5 along with the theoretically simulated signal the experimentally registered signal is depicted as well. The only adjustable parameter in this comparison is a scaling factor for the overall intensity of the experimentally detected signal. The observed signals agree very well with the level-crossing signal registered by several groups before us [24,25]. However, in these previous studies the first derivative from the intensity was measured and so we were able to compare only the exact positions of resonances. These coincide perfectly. In our case we are able to calculate not only the positions of resonances, but also the shape, width and relative amplitudes of the resonance peaks.

V. CONCLUSIONS

In this study we report for the first time the appearance of transverse orientation in atoms with hyperfine structure after excitation by linearly polarized light in the presence of an external magnetic field. We have also presented a theory that is in quantitative agreement with our data. The use of transverse alignment–orientation as a probe of level crossings is compared to previous measurements The case of measured circularity has an advantage over the more conventional measurement of the degree of linear polarization: For the case of alignment–orientation conversion, there is no signal in the absence of the external field. This implies that we do not have the first trivial resonance position at zero field value which is always present in traditional geometry (Hanle effect [26]). This allows measurements of first level crossing positions that are very close to the zero field resonance. In traditional methods these resonances are hidden under the zero field peak. For example, from the inset of Fig. 1 we can see that there must exist several resonances of $\Delta m_{F_e}=2$ crossings around 3 and 6 G. However, these resonances are hidden in a traditional level crossing signal and can not be observed (see Fig. 5). At the same time $\Delta m_{F_e}=1$ crossings that appear even at smaller field values 2, 4, and 8 G in alignment–orientation conversion signals, although not fully resolved, are clearly visible. The possibility to detect these resonances can improve the precision of atomic hyperfine splitting constants.

ACKNOWLEDGMENTS

This work could not be completed without the valuable comments and advice of Dr. Habil. Phys. Maris Tamanis from Institute of Atomic Physics and Spectroscopy, University of Latvia, and the continuous support of Professor Sune Svanberg from Department of Physics at Lund Institute of Technology. We are grateful to Professor Neil Shafer-Ray from University of Oklahoma for careful reading of the manuscript and valuable comments. Financial support from the Swedish Institute Visby program is greatly acknowledged.

[1] In this work the terms alignment, orientation, and polarization take on their technical meaning. Alignment refers to a distribution of angular momentum direction with respect to an axis, but not a preferred direction. Orientation refers to a distribution of angular momentum direction that favors a given direction.
[2] M. Lombardi, C. R. Acad. Sci., Ser. B **265B**, 191 (1967).
[3] V.N. Rebane, Opt. Spektrosk. **51**, 163 (1968).
[4] M. Lombardi, in *Beam Foil Spectroscopy*, edited by I.A. Sellin and D.J. Pegg (Plenum Press, New York, 1976) vol. 2, p. 731.
[5] T. Manabe, T. Yabuzaki, and T. Ogawa, Phys. Rev. Lett. **46**, 637 (1981).
[6] M. Lombardi, J. Phys. (Paris) **30**, 631 (1969).
[7] M. Auzinsh, Can. J. Phys. **75**, 853 (1997); M. Auzinsh and R. Ferber, Phys. Rev. Lett. **69**, 3463 (1992); M. Auzinsh, R. Ferber, and A.V. Stolyarov, J. Chem. Phys. **101**, 5559 (1994).
[8] J. Vigue, M. Broyer, and J.-C. Lehmann, J. Phys. B. **7**, L158 (1974).
[9] J. Vigue, M. Broyer, and J.-C. Lehmann, J. Chem. Phys. **62**, 4941 (1975).
[10] I. Klintsare, M. Tamanis, A.V. Stolyarov, M. Auzinsh, and R. Ferber, J. Chem. Phys. **99**, 5748 (1993).
[11] M. Auzinsh, A.V. Stolyarov, M. Tamanis, and R. Ferber, J. Chem. Phys. **105**, 37 (1996).
[12] J.C. Lehmann, J. Phys. (France) **25**, 809 (1964).
[13] J.C. Lehmann, Phys. Rev. **178**, 153 (1969).
[14] W.E. Baylis, Phys. Lett. **26A**, 414 (1968).
[15] M. Krainska-Miszczak, J. Phys. B **12**, 555 (1979).
[16] X.L. Han and G.W. Schinn, Phys. Rev. A **43**, 266 (1991).
[17] J. Alnis and M. Auzinsh, Eur. Phys. J. D **11**, 91 (2000).
[18] M. Auzinsh and R. Ferber, *Optical Polarization of Molecules* (Cambridge University Press, Cambridge, UK, 1995).
[19] D.A. Varshalovich, A.N. Moskalev, and V.K. Khersonskii, *Quantum Theory of Angular Momentum* (World Scientific, Singapore, 1988).
[20] I.I. Sobelman, *Atomic Spectra and Radiative Transitions* (Springer-Verlag, Berlin, 1979).
[21] M. Tamanis, M. Auzinsh, I. Klincare, O. Nikolayeva,

A.V. Stolyarov, and R. Ferber, J. Chem. Phys. **106**, 2195 (1997).
[22] M. Auzinsh and R. Ferber, J. Chem. Phys. **99**, 5742 (1993).
[23] E. Arimondo, M. Inguscio, and P. Violino, Rev. Mod. Phys. **49**, 31 (1977).
[24] G. Belin and S. Svanberg, Phys. Scr. **4**, 269 (1971).
[25] R.W. Schmieder, A. Lurio, W. Happer, and A. Khadjavi, Phys. Rev. A **2**, 1217 (1970).
[26] G. Moruzzi and F. Strumia, *Hanle Effect and Level-Crossing Spectroscopy* (Plenum Press, New York, 1991).

dis 3

INSTITUTE OF PHYSICS PUBLISHING JOURNAL OF PHYSICS B: ATOMIC, MOLECULAR AND OPTICAL PHYSICS

J. Phys. B: At. Mol. Opt. Phys. 34 (2001) 3889–3898 PII: S0953-4075(01)23132-0

Reverse dark resonance in Rb excited by a diode laser

Janis Alnis and Marcis Auzinsh

Department of Physics, University of Latvia, 19 Rainis Boulevard, Riga, LV-1586, Latvia

Received 20 March 2001, in final form 20 July 2001
Published 5 October 2001
Online at stacks.iop.org/JPhysB/34/3889

Abstract

The origin of recently discovered reverse (opposite-sign) dark resonances has been explained theoretically and verified experimentally. It is shown that the reason for these resonances is a specific optical pumping of the ground state magnetic sublevel in a transition when the ground state angular momentum is smaller than the excited state momentum. An experiment was conducted on ^{85}Rb atoms in a cell, when a diode laser using the ground state hyperfine level $F_g = 3$ simultaneously excites spectrally unresolved hyperfine levels with total angular momentum quantum numbers $F_e = 2, 3$ and 4. It is shown that due to differences in the transition probabilities the dominant role in total absorption and fluorescence signals is played by absorption on a transition $F_g = 3 \rightarrow F_e = 4$.

1. Introduction

Coherent population trapping was discovered in the interaction of sodium atoms with a laser field in 1976 [1]. Due to this effect a substantial part of the population (because of destructive quantum interference between different excitation pathways) is trapped in a coherent superposition of the ground state sublevels, i.e. dark states. Dark resonances are associated with coherent population trapping. This means that, due to the population trapping in the ground state, laser light absorption and, as a result, fluorescence from an ensemble of atoms decreases, while simultaneously the intensity of the transmitted light increases. If in addition to the optical excitation an external magnetic field is applied perpendicular to the light polarization, it can destroy the coherence between the ground state sublevels and return the trapped population to the absorbing states and result in increasing absorption and fluorescence, and decreasing the transmitted light. Some years ago Arimondo published a review [2] of the applications of dark resonances.

Coherence in an atomic ground state recently attracted substantial attention in connection with lasing without inversion [3], magnetometry [4], laser cooling [5], electromagnetically induced transparency [6] and very recently in connection with coherent information storage using halted light pulses [7, 8]. As a result dark resonances have been studied in detail, including open systems [9] and systems with losses [10]. During these studies the authors

of [11] observed a new and unexpected phenomenon. In this study the D_2 line of ^{85}Rb atoms was excited by a diode laser. The radiation was tuned to the absorption from the optically resolved ground state hyperfine level $F_g = 3$ originating from atomic $5S_{1/2}$ state. The final state of the transition was the Rb $5P_{3/2}$ excited state. Hyperfine components of this level were not resolved, and all dipole-allowed transitions to the excited state hyperfine levels with quantum numbers $F_e = 2, 3$ and 4 were excited simultaneously. At the same time one should note that although the hyperfine components of the excited state were not resolved within the Doppler linewidth, the laser linewidth was sufficiently narrow to excite different hyperfine transitions in different velocity classes of atoms. Consequently, each hyperfine transition under experimental conditions was excited almost independently from the other transitions despite the fact that all transitions had the same ground state level with quantum number $F_g = 3$.

In contrast to the usual dark resonance signal, the authors of [11] have observed the opposite effect—i.e. a decreased transmittance of laser radiation and increased fluorescence intensity was observed when the magnetic field was set to zero. The gas became more transparent and the fluorescence intensity decreased when the magnetic field was applied. According to the authors of [11] the physical reason for this effect *still remains unclear*.

In this paper we offer, in our opinion, a very simple and straightforward explanation of the origin of these 'reverse' dark resonances and carry out an experimental and numerical study.

2. Reverse resonance

In a simple qualitative explanation traditional dark resonances can be related to a well known optical pumping phenomenon. Let us assume that we excite an atomic transition $F_g = 2 \longrightarrow F_e = 1$ with linearly polarized light. The direction of the z-axis is chosen to be along the light electric field vector E. As a result π absorption takes place and transitions occur between the ground and excited state magnetic sublevels with $\Delta M = M_g - M_e = 0$, where M_g and M_e are magnetic quantum numbers of the ground and excited state, respectively (see figure 1). According to this scheme absorption does not take place from the ground state magnetic sublevels with quantum numbers $M_g = \pm 2$, because for these states there are no corresponding excited state magnetic sublevels with the same magnetic quantum number value.

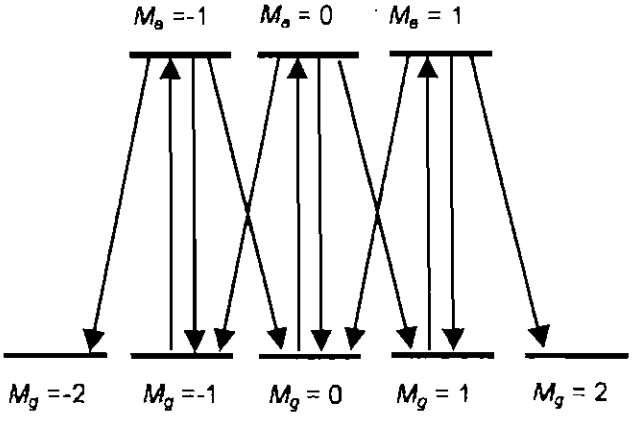

Figure 1. Allowed dipole transition scheme for ground state optical pumping in the case of π absorption for $F_g = 2 \rightarrow F_e = 1$.

In spontaneous decay, dipole transitions from optically populated excited state magnetic sublevels $M_e = \pm 1$ to the non-absorptive ground state sublevels $M_g = \pm 2$ are allowed. Consequently, if relaxation in the ground state is slow, under steady-state conditions a substantial part of the population will be optically pumped to the ground state sublevels with quantum numbers $M_g = \pm 2$ and will be trapped there. As a result the traditional decrease of the absorption and fluorescence, and increase of the transmittance will be observed, because the population of the absorbing ground state magnetic sublevels will be reduced.

If at that moment an external magnetic field is applied in a direction perpendicular to the z-axis (light polarization E), the field will effectively mix the ground state sublevels and will return the trapped population into the states from which the absorption takes place. It will increase absorption and fluorescence. This is a qualitative explanation of the usual dark resonance.

Similar reasoning can be used to explain the 'reverse' resonance reported in [11] and in this paper. Let us assume that we excite with π radiation the atomic transition $F_g = 1 \longrightarrow F_e = 2$. In this case all magnetic sublevels absorb light, and there are no sublevels that can trap the atomic population. Absorption rates between respective magnetic sublevels for linearly polarized π absorption may be calculated as

$$\Gamma_{M_g \to M_e} = \Gamma_p \frac{2F_g + 1}{2F_e + 1} \left(C^{F_e M_e}_{F_g M_g 10} \right)^2 \tag{1}$$

where Γ_p denotes the absorption rate, but $C^{c\gamma}_{a\alpha b\beta}$ denotes the respective Clebsch–Gordan coefficients. The rates of the spontaneous transitions between the excited and ground state magnetic sublevels may be calculated as

$$\Gamma_{M_e \to M_g} = \Gamma \frac{2F_e + 1}{2F_g + 1} \left(C^{F_g M_g}_{F_e M_e 1 M_g - M_e} \right)^2 \tag{2}$$

where Γ is the spontaneous relaxation rate of the excited state. Relative transition rates between magnetic sublevels of the $F_g = 1 \longleftrightarrow F_e = 2$ transition, calculated according to formulae (1) and (2), are shown in figure 2. As one can see from this figure, the ground state magnetic sublevel $M_g = 0$ is the most absorbing one, with the highest relative absorption rate. At the same time, all three excited state magnetic sublevels populated by light absorption decay strongly just to this sublevel, with high rates. One can expect that in a situation of steady-state excitation, as a result of the interplay between the absorption and the decay rates, the

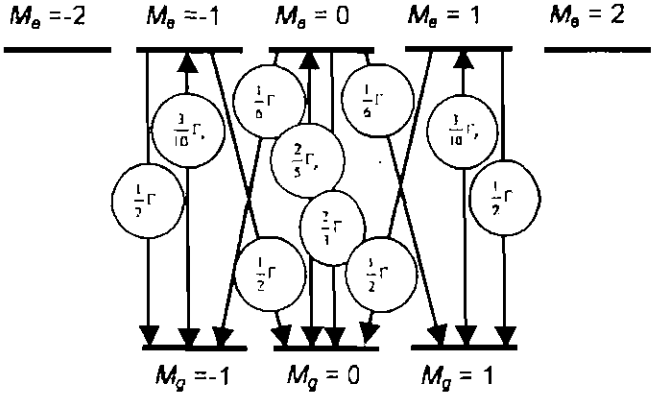

Figure 2. Transition scheme and rate constants for π absorption in the case of $F_g = 1 \longrightarrow F_e = 2$.

population of the strongly absorbing ground state magnetic sublevel $M_g = 0$ will be increased and, consequently, one can expect increased absorption and fluorescence from this atom and decreased transmittance of the resonant laser light.

If an external magnetic field is applied perpendicular to the z-axis it will mix the ground state magnetic sublevels and redistribute the population between them. Consequently, the population of the strongly absorbing magnetic sublevel $M_g = 0$ will be decreased. At the same time, the population of less strongly absorbing magnetic sublevels $M_g = \pm 1$ will be increased. This means that the total absorption and fluorescence will be decreased and transmittance will be increased. As a result reverse dark resonance will be observed.

Let us solve the balance equations for the magnetic sublevel stationary population n_{M_g} in the scheme shown in figure 2 to prove this qualitative consideration. With the steady-state conditions for the ground state magnetic sublevels we obtain

$$\begin{aligned} n_{-1} &= \frac{6(10\Gamma + 3\Gamma_p)}{5(17\Gamma + 12\Gamma_p)}\bar{n}_g \\ n_0 &= \frac{27(5\Gamma + 2\Gamma_p)}{5(17\Gamma + 12\Gamma_p)}\bar{n}_g \\ n_{+1} &= \frac{6(10\Gamma + 3\Gamma_p)}{5(17\Gamma + 12\Gamma_p)}\bar{n}_g \end{aligned} \tag{3}$$

where $\bar{n}_g$ is the ground state magnetic sublevel population in the absence of radiation. In the limit when absorption is slow $\Gamma_p \ll \Gamma$ (weak absorption), we have

$$\begin{aligned} n_{-1} &\approx \tfrac{12}{17} n_g \approx 0.706\bar{n}_g \\ n_0 &\approx \tfrac{27}{17} n_g \approx 1.59\bar{n}_g \\ n_{+1} &\approx \tfrac{12}{17} n_g \approx 0.706\bar{n}_g. \end{aligned} \tag{4}$$

This type of optical pumping in a transition $F \rightarrow F + 1$ was briefly discussed for the first time in [12] and was analysed recently in [13, 14]. If we now bear in mind the absorption rates from different magnetic sublevels of the ground state (see figure 2), and calculate the overall absorption

$$I_a = \sum_{M_g=-F_g}^{F_g} \sum_{M_e=-F_e}^{F_e} n_{M_g} \cdot \Gamma_{M_g \rightarrow M_e} \tag{5}$$

from such a state and compare it with the absorption from the equally populated magnetic sublevels then we see an increase in the total absorption by a factor of $18/17 \approx 1.059$ or by approximately 5.9%.

The same calculation can be applied to the transitions $F_g = 2 \longrightarrow F_e = 3$, $F_g = 3 \longrightarrow F_e = 4$, $F_g = 4 \longrightarrow F_e = 5$ and $F_g = 5 \longrightarrow F_e = 6$. For these schemes we will similarly obtain an even larger increasing absorption caused by this specific optical pumping. The increase factor will be $540/461 \approx 1.17$, $4004/3217 \approx 1.24$, $119\,340/92\,377 \approx 1.29$ and $1790\,712/1352\,077 \approx 1.32$, respectively. This means that the described effect increases with increase of the quantum numbers of the involved levels and can reach remarkably large values.

The presented description is of course qualitative in the sense that it does not allow prediction of the form and width of the reverse dark resonance. In our opinion nevertheless it gives a good idea about what is happening when reverse dark resonances are observed. In order to have a quantitative description of the phenomenon one must solve the equations for the density matrix for an open system with losses.

3. Expected signal

We will use equations of motion for a density matrix to perform a more accurate numerical simulation of the expected reverse dark resonance signal. They are written under the assumption of a broad spectral line excitation [15]:

$$\dot{f}_{M_e M'_e} = \Gamma_p \sum_{M_g M'_g} \langle M_e | E^* d | M_g \rangle \langle M'_e | E^* d | M'_g \rangle^* \varphi_{M_g M'_g}$$
$$- \left(\frac{\Gamma_p}{2} + i\omega_S \right) \sum_{M''_e M_g} \langle M_e | E^* d | M_g \rangle \langle M''_e | E^* d | M_g \rangle^* f_{M''_e M'_e}$$
$$- \left(\frac{\Gamma_p}{2} - i\omega_S \right) \sum_{M''_e M_g} \langle M''_e | E^* d | M_g \rangle \langle M'_e | E^* d | M_g \rangle^* f_{M_e M''_e}$$
$$- \Gamma f_{M_e M'_e} - i\omega_{M_e M'_e} f_{M_e M'_e} \tag{6}$$

$$\dot{\varphi}_{M_g M'_g} = - \left(\frac{\Gamma_p}{2} + i\omega_S \right) \sum_{M''_g M_e} \langle M_g | E^* d | M_e \rangle \langle M''_g | E^* d | M_e \rangle^* \varphi_{M''_g M'_g}$$
$$- \left(\frac{\Gamma_p}{2} - i\omega_S \right) \sum_{M''_g M_e} \langle M''_g | E^* d | M_e \rangle \langle M'_g | E^* d | M_e \rangle^* \varphi_{M_g M''_g}$$
$$+ \Gamma_p \sum_{M_e M'_e} \langle M_g | E^* d | M_e \rangle \langle M'_g | E^* d | M'_e \rangle^* f_{M_e M'_e}$$
$$- \gamma \varphi_{M_g M'_g} - i\omega_{M_g M'_g} \varphi_{M_g M'_g} + \sum_{M_e M'_e} \Gamma^{M_e M'_e}_{M_g M'_g} f_{M_e M'_e} + \lambda \delta_{M_g M'_g} \tag{7}$$

where $f_{M_e M'_e}$ and $\varphi_{M_g M'_g}$ denote density matrices of the excited and ground state level, respectively. The first term on the right-hand side of equation (6) describes the effect of light absorption on $f_{M_e M'_e}$ at an absorption rate Γ_p. The matrix elements of the form $\langle M_e | E^* d | M_g \rangle$ account for the conservation of the angular momentum in photon absorption, from the light wave with unit polarization vector E. The second and third terms jointly describe the stimulated emission of light and the shift in the dynamic Stark effect by frequency ω_S. The fourth term characterizes the relaxation of the density matrix $f_{M_e M'_e}$ with a rate constant Γ. Finally, the fifth term on the right-hand side of equation (6) describes the effect of the external magnetic field, which produces splitting of the magnetic sublevels M_e and M'_e by a value of $\omega_{M_e M'_e} = (E_{M_e} - E_{M'_e})/\hbar$.

On the right-hand side of equation (7) the first and second terms jointly describe light absorption and the effect of the dynamic Stark effect. The third term describes stimulated light emission; the fourth term describes relaxation processes in the ground state and the fifth term describes the external magnetic field effect. The sixth term characterizes the reverse spontaneous transitions at a rate $\Gamma^{M_e M'_e}_{M_g M'_g}$, and finally, the seventh term describes the relaxation of the density matrix of the ground state atoms, interacting with the rest of the gas in a cell, which is not influenced by the excitation light.

In order to solve numerically the system of equations (6) and (7), the matrix element of the electric dipole transition $\langle M_e | E^* d | M_g \rangle$ may be expanded as

$$\langle M_e | E^* d | M_g \rangle = \sum_q (E^q)^* \langle M_e | d^q | M_g \rangle \tag{8}$$

where the superscript q denotes the cyclic components of the respective vectors. The remaining matrix element can be further expanded, by applying the Wigner–Eckart theorem,

$$\langle M_e | d^q | M_g \rangle = \frac{1}{\sqrt{2F_e + 1}} C^{F_e M_e}_{F_g M_g 1 q} \langle F_e \| d \| F_g \rangle \tag{9}$$

where $\langle F_e \| d \| F_g \rangle$ is the reduced matrix element. Under stationary excitation the system of equations (6) and (7) turn into a system of linear equations for the ground and excited state density matrix elements. The coefficients for this system of equations may be calculated by means of the angular momentum algebra and the formulae presented above.

For more details concerning the system of equations of motion for the density matrix in a broad excitation line limit and methods of solution, see [15].

The analysis of the probabilities [16]

$$W_{F_g \to F_e} = (2F_e + 1)(2F_g + 1)(2J_e + 1)(2J_g + 1) \begin{Bmatrix} J_g & F_g & I \\ F_e & J_e & 1 \end{Bmatrix}^2 \begin{Bmatrix} L_g & J_g & S \\ J_e & L_e & 1 \end{Bmatrix}^2 \tag{10}$$

of optical transitions, which originate from $F_g = 3$ for three excited state hyperfine levels of the ^{85}Rb atom, shows that the levels $F_e = 2, 3, 4$ are populated in the ratio $(5/18 \approx 0.278):(35/36 \approx 0.972):(9/4 = 2.25)$. This means that the absorption rates from the ground state hyperfine level to the respective excited state hyperfine level have the same ratio (see figure 3). For the D_2 line of the rubidium atom electronic angular momentum in the ground state is $J_g = \frac{1}{2}$, and for the excited state it is $J_e = \frac{3}{2}$. In the experiment, analysed here, the rubidium isotope ^{85}Rb was used, which has a nuclear spin of $I = \frac{5}{2}$.

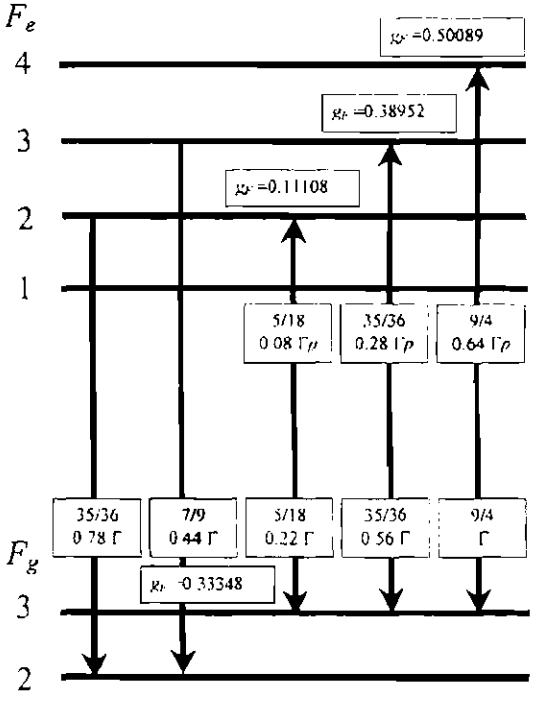

Figure 3. Relative transition strength and Landé factors of the hyperfine levels involved in formation of the reversed dark resonance signal in the ^{85}Rb atom.

In spontaneous emission there exists a disparity between the level $F_e = 4$ and all other excited state hyperfine levels involved in absorption. According to the selection rules for dipole transitions, the hyperfine level $F_e = 4$ can only decay to the initially absorbing level $F_g = 3$. This means that for this transition we have a closed cycle of optical pumping [17] with no losses. For all other excited state levels we have the possibility of spontaneously decaying to the initial level or to the other ground state hyperfine level $F_g = 2$. This decay constitutes the losses for an optical pumping. In this case the pumping cycle is open [17]. We can calculate the ratio between decay to the initial level $F_g = 3$ and the level $F_g = 2$ using the expression (10) again. We know that the total decay rate for the $5\ ^2P_{3/2}$ state is $\Gamma = 3.8 \times 10^7\ s^{-1}$ [19]. The decay rates to both ground state hyperfine levels are shown in figure 3. We assume that the magnetic field used in the experiment, which is described and analysed below, is weak enough not to substantially mix the hyperfine levels. This means that the energies of magnetic sublevels M_e and M_g are linearly dependent on the magnetic field strength, and can be found as $E_{M_i} = g_{F_i}\mu_B M_i B$, where μ_B is the Bohr magneton and B denotes the magnetic field strength. The validity of these assumptions can be justified by the results of [18]. Landé factors g_{F_i} for each of the hyperfine levels can be calculated according to the well known method [20]. Numerical values of electronic and nuclear Landé factors for the Rb atom can be found in [21]. We have used the following values for $g_{5P_{3/2}} = 1.3362$, $g_{5S_{1/2}} = 2.002\,33$ and $g_I = -0.000\,293$. The rate equations (6) and (7) for a density matrix for all allowed transitions were solved numerically. Finally, the fluorescence signal for each transition was calculated according to [15]

$$I = \tilde{I}_o \sum_{M_e M'_e M_g} \langle M_e | (E')^* d | M_g \rangle \langle M'_e | (E')^* d | M_g \rangle^* f_{M'_e M_e} \tag{11}$$

where E' is the polarization of the light, which we intend to observe and $\tilde{I}_o$ is the coefficient of proportionality. Finally, the averaged total signal was calculated by taking into account the relative transition probabilities between different hyperfine levels, as shown in figure 3. The absorbed light intensity can be calculated by noting that the energy of the absorbed light is proportional to the total population created by this absorption in the excited state of atoms for each transition involved.

Initially for signal simulation we will analyse only the $F_g = 3 \rightarrow F_e = 4$ transition. The following rate constants were used in this simulation: the total absorption rate was assumed to be $\Gamma_p = 3 \times 10^6\ s^{-1}$; ground state relaxation rate $\gamma = 2 \times 10^5\ s^{-1}$ (mainly due to collisions with the walls of the cell and flight through [15] the excitation laser beam); excited state relaxation rate, $\Gamma = 3.8 \times 10^7\ s^{-1}$; Stark shift, $\omega_S = 0$. We presume that the magnetic field is applied along the z-axis. The laser light is linearly polarized along the y-axis. The intensity of the fluorescence with the same polarization as for excitation is calculated and the intensity of the transmitted beam is calculated. For this the excited state density matrix elements are obtained as solution of the system of equations (6) and (7). Then, knowing the excited state density matrix, the fluorescence intensity can be calculated according to equation (11). For the calculation of the absorbed light intensity we are using the fact that the total absorbed light intensity is proportional to the population of the excited state, which is created by the light absorption. It may be represented by a sum of diagonal elements of the excited state density matrix. For both signals the dependence on the applied external magnetic field was analysed. The results of signal simulations are presented in figure 4. They demonstrate well the pronounced reverse resonances and are in very good qualitative agreement with the measurements obtained in [11] (see figure 5 therein). Such a strong reverse resonance is caused by the fact that in the total signal the main contribution is from the $F_g = 3 \rightarrow F_e = 4$ transition. The reason for this is that according to the data presented above, $F_g = 3 \rightarrow F_e = 4$

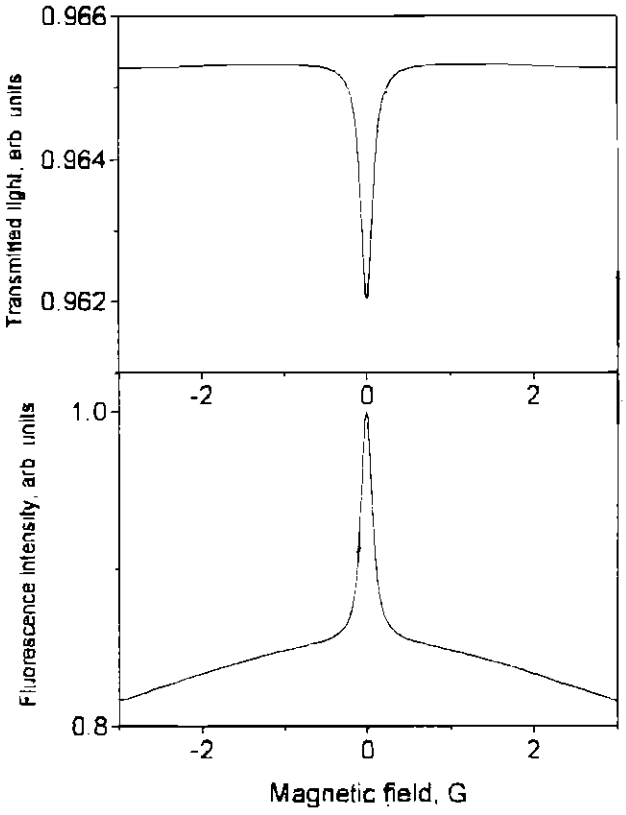

Figure 4. Calculated intensity of fluorescence and transmitted light for reverse dark resonance for $F_g = 3 \rightarrow F_e = 4$.

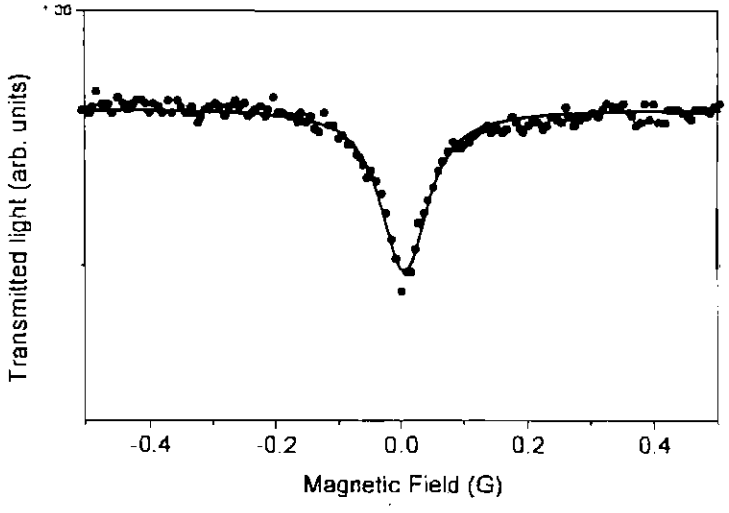

Figure 5. Measured (●) and simulated signal (full curve) for reverse dark resonance in ^{85}Rb.

is the strongest transition in the D_2 absorption. Besides, from the transitions involved in the laser light absorption, only the $F_g = 3 \rightarrow F_e = 4$ transition is a closed cycle transition. This means that only in this transition due to the selection rules do all excited atoms decay back to the initial level and the total number of atoms involved in an absorption–fluorescence cycle is conserved. In the other two transitions a certain number of the atoms decay to the other ground state hyperfine level $F_g = 2$, which do not absorb laser light with a given wavelength. As a result after several absorption–fluorescence cycles the number of atoms interacting with the laser light in these open-cycle transitions will be substantially reduced, and the absorption and fluorescence will be mainly determined by the $F_g = 3 \rightarrow F_e = 4$ transition. This effect should be well pronounced because, as already stressed, the laser line is sufficiently narrow spectrally to ensure that in each involved transition different velocity classes of atoms from the total ensemble interact with the laser. The width of the calculated resonances may be varied by changing the ground state Landé factor value, ground state relaxation rate and absorption rate.

In the weak absorption limit, $\Gamma_p \ll \Gamma$, the reverse dark resonance width is determined by a condition when the ground state Larmor frequency is equal to the ground state relaxation rate. For the $F_g = 3$ state of the ^{85}Rb atom at low concentration it can be as narrow as 20–30 mG. This is a width, which was actually observed in [11].

The obtained signals in some sense are the same as the ground state Hanle effect measured in atoms, as well as in molecules to a great extent (see, for example [15, 22]). In the case of molecules the reverse structure in the ground state Hanle effect was also observed. In the case of molecules, when optical pumping takes place in an open cycle and the total ground state population is substantially reduced due to intense absorption, this structure can be attributed to high-order coherence created by excitation light between distant ground state magnetic sublevels ($\Delta M = 6$ and greater) [23, 24]

4. Experimental

We have also carried out measurements of these reverse resonances in our laboratory. In our experiment we used isotopically enriched rubidium (99% ^{85}Rb) contained in a glass cell at room temperature to keep the atomic vapour concentration low and avoid reabsorption. The transition $5s\,^2S_{1/2}$–$5p\,^2P_{3/2}$ at 780.2 nm is excited using both temperature- and current-stabilized single-mode diode lasers (Sony SLD114VS) with beam diameter 7 mm. The absorption signal (transmitted light) is monitored using a photodiode. As the laser frequency is swept by applying a ramp on the drive current, two absorption peaks with a half-width of about 600 MHz separated by about 3 GHz appear due to the ^{85}Rb ground state hyperfine structure. The excited state hyperfine structure is not resolved under the Doppler profile.

During the resonance measurements, the laser wavelength is stabilized on the absorption peak originating from the ground state hyperfine level $F_g = 3$.

Helmholz coils are used to sweep the magnetic field over the 0 G region. Additional coils compensate the Earth's magnetic field components.

The signal which is detected in transmitted light is averaged over 64 cycles and the result is presented in a figure 5 (data points and simulated signal). The amplitude of the experimental and calculated signals in arbitrary units and the curves in the figure are scaled so as to coincide at the minimum with the measured signal. For a simulated curve the parameters are chosen to have values that best reproduce our experimental conditions. The ground state relaxation rate $\gamma = v_p/r_0 = 0.07\ \mu s^{-1}$ was chosen as a reciprocal time of thermal motion of Rb atoms at room temperature with the most probable velocity $v_p = 0.24$ mm μs^{-1} through the laser beam of radius $r_0 = 3.5$ mm [15]. The absorption rate was chosen as $\Gamma_p = 1.5\ \mu s^{-1}$. Other

parameters are the same as in figure 4. Agreement between the calculated and the measured signal is remarkable and it seems to be possible to conclude that the proposed model explains the observed signal not only qualitatively but also quantitatively.

Acknowledgments

One of us (MA) is grateful to Professor Neil Shafer-Ray from the University of Oklahoma for fruitful discussions. Financial support from the Swedish Institute Visby programme is greatly acknowledged.

References

[1] Alzetta G, Gozzini A, Moi L and Orrioli G 1976 *Nuovo Cimento* B **36** 5
[2] Arimondo E 1996 *Prog. Opt.* **35** 257
[3] Scully M, Zhu S-Y and Gavrielides A 1989 *Phys. Rev. Lett.* **62** 2813
[4] Scully M and Fleischhauer M 1992 *Phys. Rev. Lett.* **69** 1360
[5] Aspect A, Arimondo E, Kaiser R, Vansteenkiste N, Cohen-Tannoudji C 1988 *Phys. Rev. Lett.* **61** 826
[6] Harris S 1997 *Physics Today* July 36
[7] Philips D F, Fleischhauer A, Mair A, Walsworth R L and Lukin M D 2001 *Phys. Rev. Lett.* **86** 783
[8] Liu C, Dutton Z, Behroozi C H and Hau L V 2001 *Nature* **409** 490
[9] Ferrucio R, Albrecht L and Ennio A 1999 *Phys. Rev.* A **60** 450
[10] Renzoni F, Maichen W, Windholz L and Arimondo E 1997 *Phys. Rev.* A **55** 3710
[11] Dancheva Y, Alzetta G, Cartalava S, Taslakov M and Andreeva Ch 2000 *Opt. Commun.* **178** 103
[12] Kazantsev A P, Smirnov V S, Tumaikin A M and Yagofarov I A 1984 *Opt. Spectrosk.* **57** 116
[13] Renzoni F, Zimmermann C, Verkerk P and Arimondo E 2001 *J. Opt. B: Quantum Semiclass. Opt.* **3** S7
[14] Renzoni F, Cartaleve S, Alzetta G and Arimondo E 2001 *Phys. Rev.* A **63** 065401
[15] Auzinsh M and Ferber R 1995 *Optical Polarization of Molecules* (Cambridge: Cambridge University Press) p 305
[16] Sobelman I I 1979 *Atomic Spectra and Radiative Transitions* (Berlin: Springer) p 359
[17] Happer W 1972 *Rev. Mod. Phys.* **44** 169
[18] Alnis J and Auzinsh M 2001 *Phys. Rev.* A **63** 023407
[19] Belin G and Svanberg S 1971 *Phys. Scr.* **4** 269
[20] Alexandrov E B, Chaika M P and Khvostenko G I 1993 *Interference of Atomic States* (New York: Springer) p 254
[21] Arimondo E, Inguscio M and Violino P 1977 *Rev. Mod. Phys.* **49** 31
[22] Auzinsh M P and Ferber R S 1991 *Phys. Rev.* A **43** 2374
[23] Auzinsh M P and Ferber R S 1990 *Sov. Phys.–Usp.* **33** 833
[24] Auzinsh M P and Ferber R S 1983 *Opt. Spectrosk.* **55** 674

dis 4

Atomic spectroscopy with violet laser diodes

U. Gustafsson, J. Alnis, and S. Svanberg
Department of Physics, Lund Institute of Technology, P.O. Box 118, S-221 00 Lund, Sweden

(Received 28 June 1999; accepted 27 October 1999)

Laser spectroscopy with laser diodes can now also be performed in the violet/blue spectral region. A 5 mW commercially available CW laser diode operating at 404 nm was used to perform spectroscopy on potassium atoms with signal detection in absorption as well as fluorescence when operating on a potassium vapor cell and with optogalvanic detection on a potassium hollow cathode lamp. The $4s\,^2S_{1/2}-5p\,^2P_{3/2,1/2}$ transitions were observed at 404.5 and 404.8 nm, respectively. The laser diode was operated with a standard laser diode driver, and with or without an external cavity. The $4s\,^2S_{1/2}-4p\,^2P_{1/2}$ transition at 770.1 nm was also observed with a different laser diode. Here, Doppler-free saturated-absorption signals were also observed, enabling the evaluation of the ground-state hyperfine splitting of about 460 MHz. The data recorded allows an experimental verification of the theory for Doppler broadening at two widely separated wavelengths. © *2000 American Association of Physics Teachers.*

I. INTRODUCTION

The development of narrow-band tunable lasers, in particular dye lasers, has allowed the emergence of powerful spectroscopic techniques for atomic and molecular spectroscopy.[1,2] The Doppler width of the transitions is normally of the order of 1 GHz and is much larger than the laser linewidth, allowing an easy study of the Doppler-broadened transitions. Using Doppler-free techniques, a resolution limited only by the natural radiative linewidth (typically a few MHz) can be obtained for narrow-band lasers. Much data on atomic structure including hyperfine splittings and isotopic shifts have been obtained through the years.

The development of single-mode near-IR (infrared) laser diodes made the techniques of laser spectroscopy accessible for student laboratories also. The most readily available experiment was to induce the $5s\,^2S_{1/2}-5p\,^2P_{3/2,1/2}$ transitions in rubidium atoms using easily available AlGaAs semiconductor lasers at 780.2 and 794.7 nm, respectively. Such experiments using free-running diode lasers on an atomic beam were described by Camparo and Klimac.[3] At our university, a laboratory session on rubidium laser diode spectroscopy has been offered for all physics students since 1990. Doppler-broadened transitions in an atomic vapor cell are observed, and by back-reflecting the laser diode beam, Doppler-free saturation signals are also recorded. We recently helped implement such experiments on isotopically enriched cells of ^{85}Rb and ^{87}Rb at four African universities, in Dakar (Senegal), Khartoum (Sudan), Nairobi (Kenya), and Cape Coast (Ghana) (see, e.g., Ref. 4). Laser diode spectroscopy for teaching purposes has also been demonstrated for Cs (852.3 nm)[5,6] and Li (671.0 nm).[7,8] Here, an improved laser performance (extended tuning range and narrow linewidth) was achieved by employing an external cavity including a Littrow grating.

The purpose of the present paper is to bring to the attention of the reader the fact that diode laser spectroscopy can now be extended to the violet/blue spectral region, due to the recent remarkable progress in GaN semiconductor lasers at Nichia Corporation by Nakamura and collaborators.[9,10] Blue diode laser spectroscopy is illustrated with experiments on the second resonance lines $4s\,^2S_{1/2}-5p\,^2P_{3/2,1/2}$ of potassium at 404.5 and 404.8 nm. For reference and comparison, the near-IR potassium line $4s\,^2S_{1/2}-4p\,^2P_{1/2}$ at 770.1 nm was induced with a different semiconductor laser. With the near-IR laser diode used it was not possible to observe the $4s\,^2S_{1/2}-4p\,^2P_{3/2}$ line at 766.7 nm.

Natural potassium consists of two isotopes, ^{39}K (93%) and ^{41}K (7%), both with a nuclear spin of $\frac{3}{2}$. Because of the dominance of ^{39}K we only need to consider this isotope. The structures of the near-IR and blue lines are given in Fig. 1, where the hyperfine structure splittings are obtained from Ref. 11. We note that, because of the small magnetic moment of the ^{39}K nucleus, the hyperfine structure splittings are small. The ground-state splitting is 462 MHz; for ^{41}K it is even smaller, 254 MHz. Thus, the Doppler-broadened line is not expected to show any structure, while a saturated absorption spectrum should be dominated by two peaks separated by about 460 MHz and broadened by upper-state unresolved hyperfine structure. Because of the fact that the excited state hyperfine structure is small and in the present context nonresolvable, while the ground-state splitting produces sharp separated peaks, it could be argued that potassium is pedagogically better suited than Li, Rb, and Cs for a student laboratory session at a particular level of atomic physics knowledge.

It is not our intention to record and evaluate high-resolution atomic spectra in the present work. Instead we would like to emphasize the use of free-running laser diodes and laser diode use in a simple feedback cavity, to demonstrate, evaluate, and experimentally verify the theory for Doppler broadening while also drawing attention to the phenomenon of hyperfine structure.

II. EXPERIMENTAL SETUP

The experimental arrangements employed in the present experiments are shown in Fig. 2. Direct absorption monitoring, laser-induced fluorescence, and optogalvanic detection are indicated. The violet semiconductor laser enabling the experiments on the $4s-5p$ transition was acquired from Nichia Corporation (Type NLHV500) and has a nominal wavelength at 25 °C of 404 nm and an output power of 5 mW. The near-IR $4s-4p$ transition was induced by a more conventional AlGaAs semiconductor laser (Mitsubishi ML4102) with a nominal wavelength of 772 nm and output power of 5

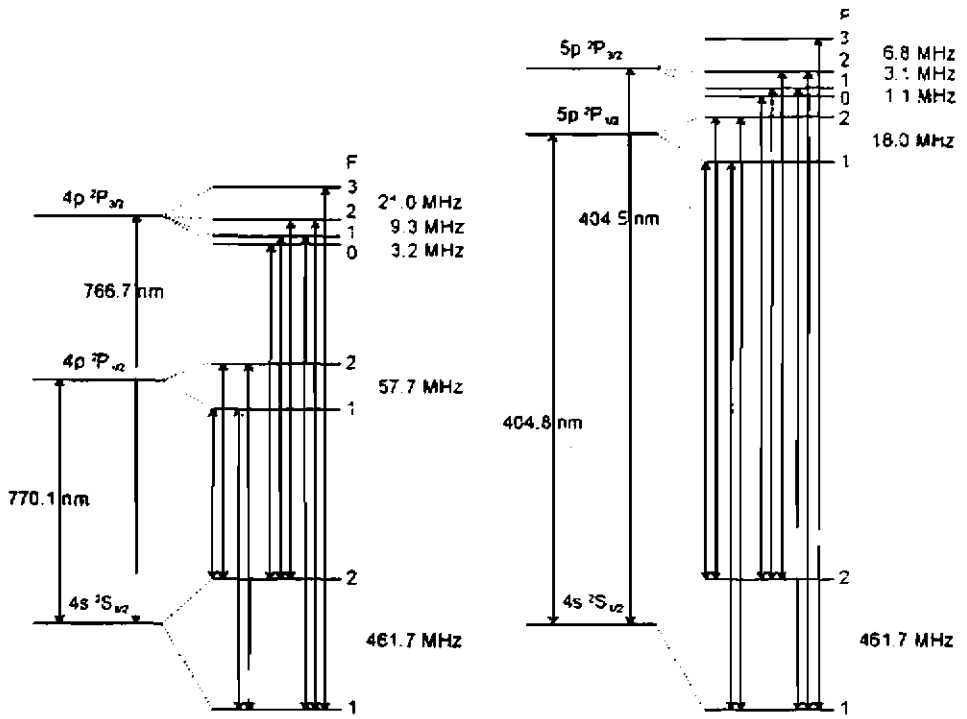

Fig. 1. Hyperfine structure diagrams of the $4s\,^2S_{1/2}$–$5p\,^2P_{3/2,1/2}$ and the $4s\,^2S_{1/2}$–$4p\,^2P_{3/2,1/2}$ transitions in ^{39}K. The energy splittings are not given to scale.

mW. The laser diodes were placed in a thermo-electrically cooled mount (Thorlabs TCLDM9) and operated with a low-noise laser diode driver (Melles Griot 06DLD103). Typically, the operating currents of the two laser diodes were set to 40 and 59 mA, respectively. Wavelength tuning of the laser diodes was accomplished by changing the temperature of the laser capsule. Once the temperature was set, a current ramp with a frequency of 100 mHz or 100 Hz was added to the operating current by means of a function generator (Tektronix FG504), allowing us to record the whole line profile in a single scan. The lower frequency was used for the optogalvanic detection while the higher frequency was used for the absorption and fluorescence measurements. In some of the experiments with the violet diode laser, a simple external feedback cavity with a Littrow grating was used to ensure single-mode operation, since the free-running laser typically lased on a few modes, separated by about 0.05 nm. External cavity laser arrangements are commercially available from several suppliers, e.g., New Focus, Newport, Thorlabs, and Tui Optics, and we used the Thorlabs system based on the laser diode mount, a piezo-electric mirror mount (KC1-PZ), a piezo-electric driver (MDT-690), and a 2400 l/mm grating (Edmund Scientific 43224). A molded glass aspheric lens (Geltech C230TM-A) was used to collimate the output beam from the diode laser. Details for constructing a laser diode system, including external cavity and electronic control, from parts in the laboratory, are given in e.g. Ref. 5. The 4 cm long potassium cell, which was prepared on a vacuum station by distilling a small amount of the metal into the cell after thorough bake-out at elevated temperatures, was placed in a small electrically heated oven. The oven had small windows for transmitting the laser beam and a larger window for observing laser-induced fluorescence.

The transmitted laser beam was focused on a detector (Hamamatsu S1223 pin photo-diode in a home-made trans-impedance amplifier module) by an $f=50$ mm lens (Thorlabs BSX060-A). The detector output voltage was fed via a low noise amplifier (Stanford Research Systems SR560) to a signal averaging oscilloscope (Tektronix TDS520B). Finally, the recorded waveform could be transferred to a PC for processing and evaluation. A small part of the laser beam was split off by a beam splitter (neutral density filter) and sent to a low-finesse solid glass etalon with a free spectral range of 991 MHz in the near-IR region and 979 MHz in the violet. The generated fringes, which were detected by another detector, allow us to frequency calibrate each individual scan.

As an alternative detection method, the fluorescence induced by the violet transition could be monitored. The $4p$–$4s$ near-IR transitions, isolated by a Schott interference filter ($\lambda_{peak}=768$ nm), were used. By employing transitions from the $4p$ state, populated in cascade decays via the $5s$ and $3d$ states, instead of the direct decays on the violet $5p$–$4s$ transition, problems with background due to scattered light from cell windows and oven structures could be completely avoided. A photomultiplier tube (EMI 9558) was employed and the signal was fed via a current-to-voltage amplifier (Ithaco 1212) to the oscilloscope. We also tested a simple large-area photo-diode (Hamamatsu S-1226-8BK) for recording the fluorescence with quite satisfactory results.

The use of a hollow-cathode discharge lamp and optogalvanic detection is a further alternative for observing the blue potassium transitions. We used an Instrumentation Laboratory hollow-cathode lamp (Model 89227), intended for an atomic absorption spectrophotometer. A discharge current of 5 mA, also passing through a ballast resistor, was driven by an Oltronik photomultiplier supply (Model A2.5K-10HR), set for typically 300 V when the discharge was running. A rotating chopper (Stanford Research System SR540) was used for modulating the laser beam at 340 Hz, and the ac voltage across the ballast resistor occurring when atoms are excited was detected with a lock-in amplifier (EG&G 5209).

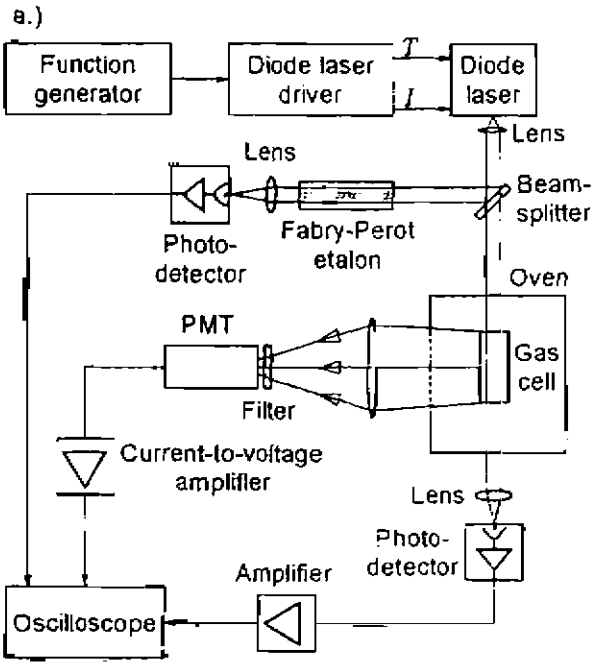

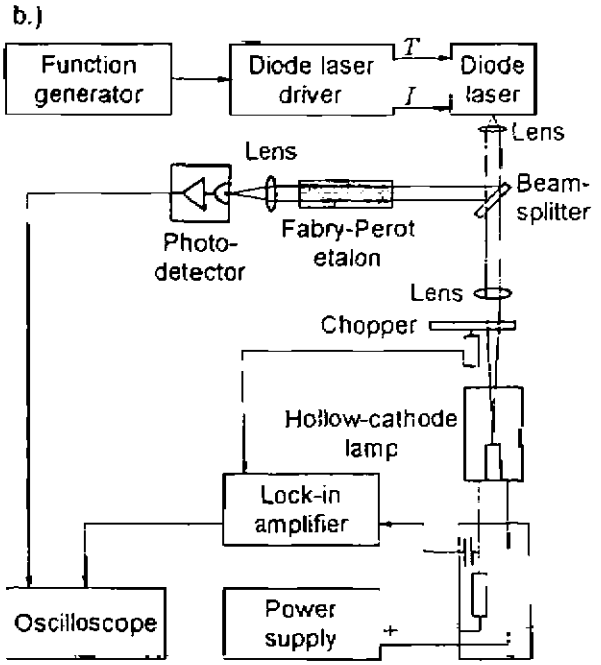

Fig. 2. Experimental setup for absorption, fluorescence (a) and optogalvanic spectroscopy (b) on potassium atoms.

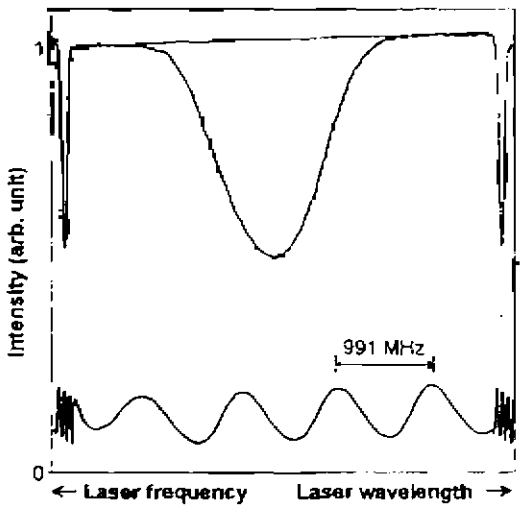

Fig. 3. Raw data obtained in an absorption recording of the $4s\,^2S_{1/2}$–$4p\,^2P_{1/2}$ potassium transition. Note the increasing laser output over the scan, but the quasi-linear frequency sweep as evidenced by equidistant Fabry–Perot fringes. The signals associated with the retrace at the end of the saw-tooth sweep are also evident.

III. MEASUREMENTS

The experimental setup was first tested by inducing the $4s\,^2S_{1/2}$–$4p\,^2P_{1/2}$ transition in the near-IR spectral region. This transition has, like the corresponding resonance lines in Rb and Cs,[3–8] high oscillator strengths, meaning a strong absorption already at atomic densities of $10^{15}/\mathrm{m}^3$, corresponding to about 50 °C for potassium. Thus, the transitions are easily observable in absorption measurements. The near-IR transition was induced with the Mitsubishi laser operated without an external cavity. Raw data for a potassium absorption measurement are shown in Fig. 3, where the low-finesse Fabry–Perot fringes are also displayed. It can be noted that the laser output power increases during the scan, but that the frequency sweep is quite linear. Thus, no frequency scale rectification was employed in our experiments, but the recorded curves were normalized the case of a constant laser output by dividing the recorded curve by a curve without atomic absorption. This procedure, like all subsequent data processing, was readily performed within the Microsoft EXCEL data package. The data shown in the rest of this paper are all preprocessed in this way. Typical normalized recordings for different vapor cell temperatures are shown in Fig. 4(a). By reflecting the laser beam back onto itself, saturated absorption signals with increased transmission are seen separated by about 460 MHz as displayed in Fig. 4(b). The excited state hyperfine structure is not resolved. In between the two signals a strong cross-over signal[1] is observed. In these measurements, performed with a beam size of about 1 mm×3 mm, care was exercised to avoid a direct feedback of the reflected beam into the diode laser which causes unstable oscillation. In the figure, an experimental curve recorded without beam reflection is superimposed, making an isolation of the nonlinear spectroscopic features easy.

Since the fluorescence is strong on the near-IR lines, the background due to scattering in cell windows, etc., is not severe, allowing the laser-induced fluorescence to be readily observed as shown in Fig. 5. Fitted curves, to be discussed later, are included in the figure. The lower trace shows the Doppler-free features due to the back-reflection of the beam into itself from the glass cell with normal-incidence windows.[12] The cross-over signal and one of the Doppler-free signals is clearly discernible. In the upper trace, we have misaligned the gas cell to only record the Doppler-broadened profile.

The $4s$–$5p$ violet transitions in potassium have much smaller oscillator strength than the near-IR transitions. Thus, considerably higher temperatures are needed on the cell to observe line absorption. In contrast, fluorescence detection, which in this case is background free, is already possible at temperatures as low as 30 °C. A transmission trace showing the violet line absorption on the $4s\,^2S_{1/2}$–$5p\,^2P_{3/2}$ transition is displayed in Fig. 6(a). This recording is performed with

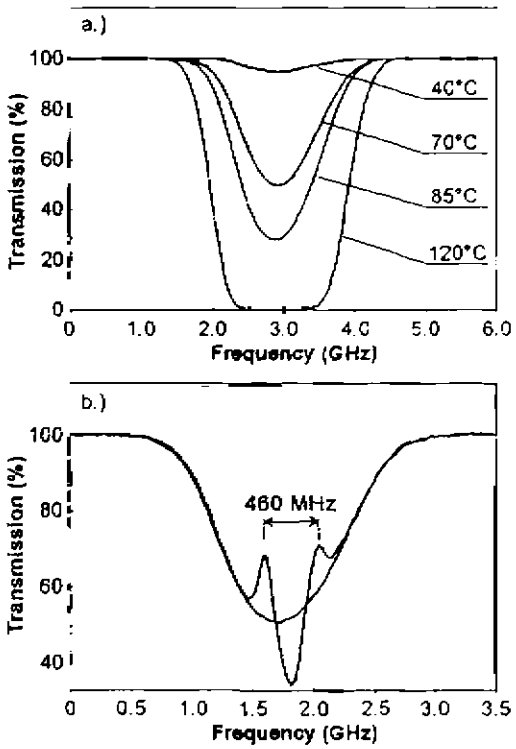

Fig. 4. Absorption recording on the $4s\,^2S_{1/2}$–$4p\,^2P_{3/2}$ potassium transition recorded for (a) different cell temperatures and (b) saturated absorption signal when the laser beam is reflected back on itself for a cell temperature of 70 °C.

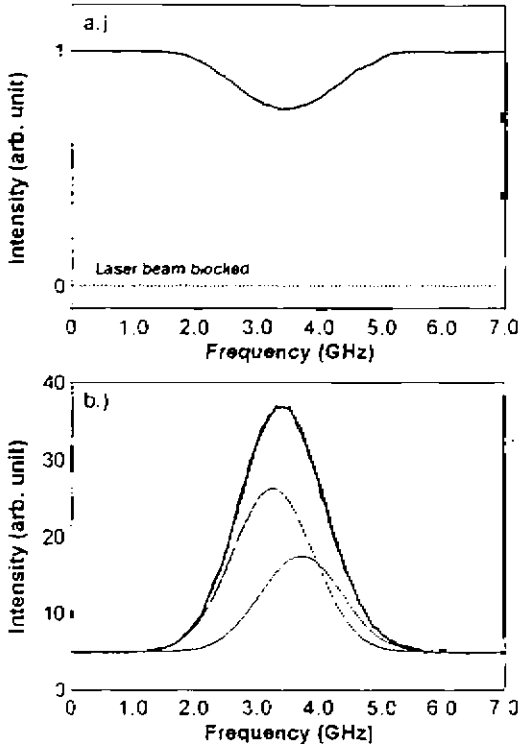

Fig. 6. Absorption (a) and fluorescence (b) recordings of the $4s\,^2S_{1/2}$–$5p\,^2P_{3/2}$ transition in potassium. The cell temperature was about 130 °C for the absorption recording and 70 °C for the fluorescence recording.

the violet laser operating in the external cavity. The $4s\,^2S_{1/2}$–$5p\,^2P_{1/2}$ transition was observed in a separate scan. For the weak violet transitions it is more difficult to reach strong saturation conditions and the Doppler-free signals were not observed in our experiments. A fluorescence recording of the same transition is shown in Fig. 6(b), together with fitted curves to be discussed later.

Optogalvanic detection[1,2] in a discharge relies on the fact that excited atoms are more easily ionized by electronic impact than ground-state atoms. Thus, when chopping the excitation beam, a corresponding ac component occurs in the discharge current at resonance. An optogalvanic lock-in recording of the $4s\,^2S_{1/2}$–$5p\,^2P_{3/2}$ transition is shown in Fig. 7. Here the violet laser was operated in free-run without using an external cavity. As mentioned above, the laser was then not running in a single longitudinal mode, as evidenced in separate tests using a high-resolution spectrometer. Laser output spectra without and with an external cavity are given in the insert of the figure. Note that for free atoms with isolated spectral features as in our case, the general spectral appearance is not influenced since only one of the oscillating modes interacts with the atoms. However, some broadening of the individual mode linewidth in multi-mode operation make spectral recordings less suited for line-shape studies such as those in the present experiments. For molecules with

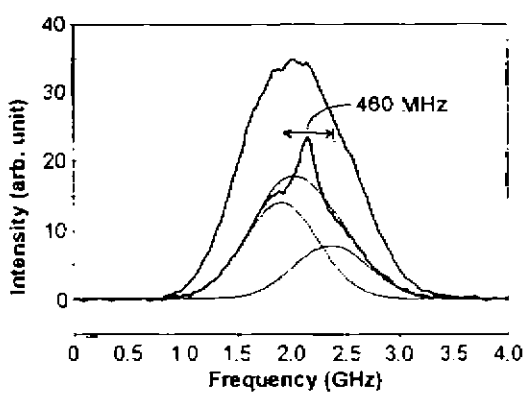

Fig. 5. Fluorescence recordings of the $4s\,^2S_{1/2}$–$4p\,^2P_{3/2}$ transition using a single laser beam, crossing a potassium vapor cell. The lower trace (magnified 4×) shows Doppler-free features by a back-reflection from the cell windows. The cell temperature was 40 °C for the lower trace and 60 °C for the upper trace.

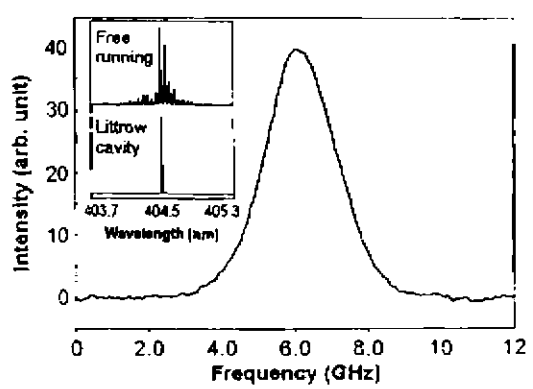

Fig. 7. Optogalvanic spectrum of the $4p\,^2S_{1/2}$–$5p\,^2P_{3/2}$ transition in potassium. The insert shows the laser diode output spectra when the laser diode is operating without and with an external cavity.

a multitude of close-lying lines, multi-mode behavior is, of course, unacceptable.

IV. DISCUSSION

Diode laser spectroscopy for the violet and near-IR $s-p$ transitions in potassium was demonstrated using simple equipment. Potassium has not previously been used in student laboratory work. With the very recent availability of violet semiconductor lasers, it became possible to directly excite, for the first time to our knowledge, a more highly excited state of an alkali atom with a laser diode. The outcome could then be compared with the results from experiments involving the first excited state, performed with the same simple setup.

The pedagogical value of a laboratory session along the lines discussed in this paper in part consists of running and scanning the diode lasers, and of adjusting the optical components and electronic devices for allowing the spectroscopic recordings, which could be demonstrated with three different detection methods. The other part is the atomic physics content. For this part, a useful approach is to record the near-IR $4s\,^2S_{1/2}-4p\,^2P$ transition in fluorescence and absorption for single and double laser beam passage through the cell. Since the upper-state hyperfine structure for the present purpose could be considered to be absent, the two Doppler-free peaks directly allow the ground-state splitting to be evaluated. The fluorescence line-shape $S(\nu)$ recorded for single-beam passage can then be fitted to a sum of two Gaussians with a half-width (FWHM) of $\Delta\nu$, separated by 460 MHz and having an intensity ratio of $A:B$,

$$S(\nu)=A\exp(-4\ln(2)(\nu/\Delta\nu)^2)+B\exp(-4\ln(2)((\nu+460)/\Delta\nu)^2). \quad (1)$$

The value for $\Delta\nu$ obtained is then compared with the theoretical value $\Delta\nu_D$:

$$\Delta\nu_D=\sqrt{\frac{(8\ln 2)RT}{c^2M}}\,\nu_0, \quad (2)$$

where ν_0 is the transition frequency at line center, R is the gas constant [8.3143 J/mol K], c is the speed of light, T is the cell temperature (in K), and M is the atomic mass number (39). The Doppler width for the near-IR transition is about 0.8 GHz for the temperatures discussed here (20 °C–120 °C).

With the violet laser a substantially broader fluorescence lineshape is then recorded and fitted to Eq. (1), and the Doppler width is extracted. Now the transition frequency is a factor of 1.90 higher and the violet theoretical Doppler width is correspondingly larger, typically 1.5 GHz using Eq. (2).

For both lines, good fits and experimental widths close to the calculated ones are obtained, e.g., the fits included in the fluorescence recordings in Figs. 5 and 6 yield 0.82 GHz (40 °C) and 1.55 GHz (70 °C), respectively, for the Doppler widths, to be compared with the theoretical values of 0.79 and 1.57 GHz, respectively. The good curve fits obtained using Gaussians and the experimental Doppler width values obtained in two widely separated wavelength ranges strongly support the theory for Doppler broadening. A discussion of the velocity Maxwellian distribution and Doppler broadening can be found, e.g., on p. 67 of Ref. 1 and p. 86 of Ref. 2.

The ratio of the statistical weights of the two hyperfine ground state levels ($F=2$ and $F=1$) is 5:3, which is also the expected line intensity ratio (A/B) for transitions to an unresolved excited state. The experimentally deduced intensity ratios, 1.80 and 1.71, respectively, for the curves in Figs. 5 and 6 are close to the theoretical ratio, 1.67.

A further suitable violet transition for a student laboratory session is the aluminum 397 nm line. The $3p\,^2P_{1/2}-4s\,^2S_{1/2}$ transition at 396.2 nm for the single aluminum isotope ^{27}Al with a 1.26 GHz S-state hyperfine splitting allows very pedagogical optogalvanic recordings from an aluminum hollow-cathode lamp. A calcium hollow-cathode lamp run at a somewhat higher discharge current than normal produces Ca^+ ions with its potassium-like resonance transitions at 393.5 and 397.0 nm, respectively, which could be monitored by optogalvanic spectroscopy. An interesting pedagogical observation is, then, that the first excited state in potassium-like Ca^+ is located at about the same energy as the second excited state in potassium, due to the excess charge of the calcium nucleus.

V. CONCLUSION

We have performed laser diode spectroscopy in the near-IR and violet spectral region on potassium. The experiments demonstrate the possibility to perform simple and inexpensive laser spectroscopy on Doppler-broadened profiles of the same atom in different spectral regions, allowing the experimental verification of the theory for Doppler broadening at two widely separated wavelengths.

ACKNOWLEDGMENTS

This work was supported by the Swedish Research Council for Engineering Sciences (TFR) and the Knut and Alice Wallenberg Foundation.

[1] W. Demtröder, *Laser Spectroscopy* (Springer Verlag, Heidelberg, 1996), 2nd ed.

[2] S. Svanberg, *Atomic and Molecular Spectroscopy—Basic Aspects and Practical Applications* (Springer Verlag, Heidelberg, 1997), 2nd ed.

[3] J. C. Camparo and C. M. Klimac, "Laser spectroscopy on a shoestring," Am. J. Phys. 51 (12), 1077–1081 (1983).

[4] S. Diop, "Utilisation des lasers a semi-conducteurs (AlGaAs) en spectroscopie d'absorption de saturation et de modulation de frequence dans le rubidium (^{85}Rb et ^{87}Rb)," Thesis for Maitre es Science, Universite Cheikh Anta Diop de Dakar, 1997.

[5] K. B. MacAdam, A. Steinbach, and C. Wieman, "A narrow-band tunable diode laser system with grating feedback, and a saturated absorption spectrometer for Cs and Rb," Am. J. Phys. 60 (12), 1098–1111 (1992).

[6] C. Wieman and L. Hollberg, "Using diode lasers for atomic physics," Rev. Sci. Instrum. 62 (1), 1–20 (1991).

[7] K. G. Libbrecht, R. A. Boyd, P. A. Willems, T. L. Gustavson, and D. K. Kim, "Teaching physics with 670 nm diode lasers—construction of stabilized lasers and lithium cells," Am. J. Phys. 63 (8), 729–737 (1995).

[8] L. Ricci, M. Weidemüller, T. Esslinger, A. Hemmerich, C. Zimmermann, V. Vuletic, W. König, and T. W. Hänsch, "A compact grating-stabilized diode laser system for atomic physics," Opt. Commun. 117 (5–6), 541–549 (1995).

[9] S. Nakamura and G. Fasol, *The Blue Laser Diodes* (Springer Verlag, Heidelberg, 1997).

[10] S. Nakamura and W. Kaenders, "Market-ready blue diodes excite spectroscopists," Laser Focus World May 1999, 69–75.

[11] E. Arimondo, M. Inguscio, and P. Violino, "Experimental determinations of the hyperfine structure in the alkali atoms," Rev. Mod. Phys. 49 (1), 31–75 (1977).

[12] T. P. Duffey, D. Kammen, A. L. Schawlow, S. Svanberg, H. R. Xia, G. G. Xiao, and G. Y. Yan, "Laser spectroscopy using beam overlap modulation," Opt. Lett. 10 (12), 597–599 (1986).

dis 5

Frequency-modulation spectroscopy with blue diode lasers

Ulf Gustafsson, Gabriel Somesfalean, Janis Alnis, and Sune Svanberg

Frequency-modulation spectroscopy provides ultrasensitive absorption measurements. The technique is especially adaptable to diode lasers, which can be modulated easily, and has been used extensively in the near-infrared and infrared spectral regions. The availability of blue diode lasers now means that the accessible wavelength region can be increased. We successfully demonstrate wavelength-modulation spectroscopy and two-tone frequency-modulation spectroscopy for the weak second resonance line of potassium at 404.8 nm and for the transition at 405.8 nm in lead, starting from the thermally populated $6p^2\ ^3P_2$ metastable level. Information on the modulation parameters is obtained with a fitting procedure. Experimental signal-to-noise ratios at different absorption levels are compared with theoretical signal-to-noise ratios and show good agreement. Detection sensitivities of 2×10^{-6} and 5×10^{-5} for wavelength and two-tone frequency-modulation spectroscopy, respectively, for a 120-Hz bandwidth are demonstrated.

OCIS codes: 300.6260, 300.6380, 300.1030.

1. Introduction

Diode laser absorption spectroscopy based on frequency modulation (FM) is a commonly used method for fast and ultrasensitive detection of minute concentrations of gas.[1–6] The interaction between a modulated laser field and an absorbing sample leads to the generation of an absorption-related signal that can be detected at the applied modulation, at an overtone, or at an intermediate frequency by use of frequency- and phase-sensitive electronics. Characteristically this process shifts the detection band to a high-frequency region, where the laser excess ($1/f$) noise is avoided. Although a variety of FM methods have been implemented, they actually represent limiting cases of the same technique. Depending on the number of modulation tones, on the choice of modulation frequency relative to the spectral width of the absorbing feature, and on the detection frequency, the methods are referred to as wavelength-modulation spectroscopy (WMS),[7] single-tone FM spectroscopy (STFMS),[8] or two-tone FM spectroscopy (TTFMS).[9]

In WMS the modulation frequency is much smaller than the half-width of the absorbing feature, whereas STFMS and TTFMS are characterized by modulation frequencies that are comparable to or larger than the half-width of the absorbing feature. WMS is usually performed at kilohertz frequencies (low-frequency WMS), with conventional lock-in amplifiers used for signal detection. For maximum sensitivity a large FM index, defined as the ratio between the maximum frequency deviation and the modulation frequency, is required. The sensitivity can be significantly improved by use of megahertz modulation frequencies (high-frequency WMS) and harmonic detection at moderate FM indices.[10–12] Inasmuch as STFMS and TTFMS use high modulation frequencies, high sensitivity can be achieved with a low FM index.[10–12] STFMS used for broad atmospheric-pressure lines with linewidths of some gigahertz requires detection electronics with matching bandwidths. Such instruments are complicated, expensive, and not always available in the wavelength region of interest. TTFMS circumvents this problem by using high FM of the laser at two closely spaced frequencies and detecting the signal at the difference frequency, often in the megahertz range. Thus, in TTFMS it is possible to use detection electronics of moderate bandwidth and still preserve high sensitivity at a low FM index. In the high-FM techniques (high-frequency WMS, STFMS, and TTFMS), the lock-in amplifier is

The authors are with the Department of Physics, Lund Institute of Technology, P.O. Box 118, SE-221 00 Lund, Sweden. J. Alnis is on leave from the Institute of Atomic Physics and Spectroscopy, University of Latvia, Rainis Boulevard 19, LV-1586 Riga, Latvia. The e-mail address for S. Svanberg is sune.svanberg@fysik.lth.se.

Received 28 October 1999; revised manuscript received 21 April 2000.

0003-6935/00/213774-07$15.00/0

replaced by discrete components. The use of FM at high frequencies offers the possibility of quantum-noise-limited detection.[13–17]

Diode lasers are especially well suited for high-sensitivity absorption spectroscopy because one can both tune their emission wavelengths over the whole absorption profile by changing the temperature of the laser capsule and modulate their frequencies directly by applying an ac current on the drive current. Recently the Nichia Corporation introduced blue cw GaN diode lasers that emit near 400 nm.[18] Gustafsson *et al.*[19] recently demonstrated the usefulness of these lasers for spectroscopy by performing experiments with potassium vapor. No attempts at sensitive detection were made in these experiments, which employed direct absorption, laser-induced fluorescence, and optogalvanic spectroscopy. Here we extend this study by using the blue diode laser and perform WMS and TTFMS on potassium as well as on lead. We study the second resonance line, $4s\ ^2S_{1/2}$–$5p\ ^2P_{3/2}$, in potassium (^{39}K) at 404.8 nm. We also record the transition in lead (^{208}Pb) at 405.8 nm, starting from the thermally weakly populated $6p^2\ ^3P_2$ metastable level situated 1.3 eV above the ground state. Absorption signals are measured at different temperatures and thus at different absorptions. By means of a fitting procedure, information regarding the modulation parameters is obtained. We examine the possibilities of making highly sensitive absorption measurements in what is for diode lasers a new and interesting wavelength region and compare experimentally deduced and theoretically calculated signal-to-noise ratios (SNR's). To achieve high sensitivity for both WMS and TTFMS, we perform WMS in the high-frequency wavelength-modulation regime, applying a modulation frequency of 5 MHz and detecting the second harmonic at 10 MHz, whereas for TTFMS we use modulation frequencies near 900 MHz, i.e., larger than the Doppler widths (HWHM), which are less than 800 MHz for the transitions studied and detect beat signals at the same frequency as for WMS.

2. Experiment

A schematic of the setup for WMS and TTFMS experiments is shown in Fig. 1. The blue diode laser (Nichia NLHV500) has a nominal wavelength of 404 nm at 25 °C and a typical output power of 5 mW. The laser diode is placed in a thermoelectrically cooled mount and is current and temperature controlled by a precision diode laser driver (Melles Griot 06DLD103). The diverging laser beam is collimated by a molded glass aspheric lens (Geltech C230TM-A) and is divided by a neutral-density filter. One part of the beam is transmitted through a small electrically heated oven into which either a 4-cm-long potassium cell or a 3.5-cm-long lead cell is placed. The other part of the beam is directed through a low-finesse confocal Fabry–Perot etalon (free spectral range, 1.5 GHz) for frequency calibration of the absorption spectrum. Both beams are focused on detectors that contain p–i–n photodiodes (Hamamatsu S-1190) and homemade transimpedance amplifiers.

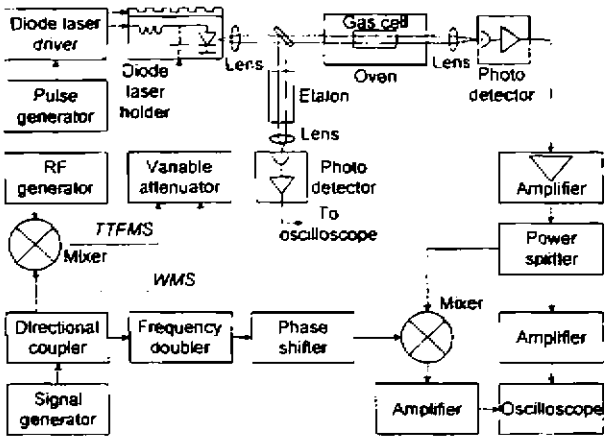

Fig. 1. Experimental setup for direct absorption spectroscopy, WMS, and TTFMS of potassium and lead vapor in sealed-off cells.

Wavelength scanning is achieved by repetitive application of a rectangular current pulse (Tektronix RG501) with a duration of 1–2 ms and a repetition rate of 100 Hz to the diode laser drive current, which is biased below the threshold current. A heat-induced constant-current wavelength shift is produced during the rectangular current pulse if the rise time of the pulse is short compared with the growth rate of the junction temperature. This wavelength-scanning technique minimizes variations in laser intensity and spectral characteristics and ensures an almost constant FM index during the scan.[20,21] It also permits simultaneous recording of the absorption line and of the zero intensity level in direct absorption. The free-running laser typically lases on a few modes separated by ~0.05 nm, as evidenced in a separate test with a high-resolution spectrometer. However, judicious choices of temperature and drive current ensure nearly single-mode operation.

The FM schemes for WMS and TTFMS are almost identical; the only difference is in the method of generating the modulation frequencies. In TTFMS we generate the two modulation frequencies by mixing a 905-MHz signal (Wavetek 2510A) and a 5.35-MHz signal (Tektronix SG503) in a frequency mixer (Mini-Circuits ZFM-4H). For WMS, only the 5.35-MHz modulation frequency is used. The modulation current, before it is superimposed upon the laser drive current, passes a variable attenuator, which allows the radio-frequency (rf) power to the diode laser to be varied. We detect the TTFMS and WMS signals by mixing (Mini-Circuits ZFM-3) the amplified (Mini-Circuits ZFL-1000LN) beat and second-harmonic signals (at 10.7 MHz) from the detector with the frequency-doubled (Mini-Circuits FD-2) and appropriately phase shifted (Synergy PP-921) 5.35-MHz signal. We adjust the rf power for the highest possible WMS and TTFMS signal amplitudes that can be achieved without the introduction of any significant modulation broadening. We split off (Mini-Circuits ZFRSC-2050) one part of the detector signal before the frequency mixer so we can observe the direct

absorption signal. Where appropriate, bandpass-, high-pass, and low-pass filters are inserted to prevent the modulation frequencies from reaching the demodulation mixer, the detection frequency signal from reflecting back toward the laser, and the modulated absorption-related signals from influencing the direct absorption signals. The direct and demodulated signals are amplified and low-pass filtered at 30 kHz in low-noise preamplifiers (Stanford SR560) and then averaged 256 times in a digital oscilloscope (Tektronix TDS520B). Thus the effective bandwidth of the detection system is approximately 120 Hz. Finally, the recorded waveforms are transferred to a computer for processing and evaluation.

In WMS it is possible to record both the absorption and the dispersion related to the probed medium. Here we consider only the absorption-related signal by making the appropriate choice of detection phase. We can do this because the in-phase (0 or π) component of the signal corresponds to pure absorption, whereas the quadrature ($\pm\pi/2$) component corresponds to pure dispersion. In TTFMS a small part of the dispersion component will fall into the detection angle, provided that the detection phase (approximately 0 or π) is adjusted for optimum signal amplitude.[22] However, for the transitions studied, the chosen modulation frequencies, and the precision of the detection phase adjustment ($\pm 5\%$), the dispersion component is less than 0.1% of the absorption component and is thus negligible.

3. Measurements

Natural potassium consists of two isotopes, ^{39}K (93%) and ^{41}K (7%), both with a nuclear spin of 3/2. The studied sealed-off potassium gas cell contains only the isotope ^{39}K. We note that the existence of a nonzero nuclear spin for potassium gives rise to a hyperfine splitting of the $4s\ ^2S_{1/2}$–$5p\ ^2P_{3/2}$ transition. However, because of the small magnetic moment of the potassium nucleus, the hyperfine splittings are small; for ^{39}K the ground-state splitting is only 462 MHz and the upper-state splitting is ~2 orders of magnitude smaller.[23] Thus the Doppler-broadened potassium line, with a half-width of ~800 MHz for the temperatures used here, is not expected to show any structure.

Typical recorded spectra for direct absorption and TTFMS measurements at 90 °C in potassium are shown in Fig. 2, where the low-finesse etalon fringes are also displayed. The WMS line shape is almost identical to that of TTFMS and is not shown. Because a rectangular current pulse is used for wavelength scanning, the laser output power is almost constant during the scan, the zero intensity level can be seen in the direct absorption recording, and the frequency sweep is quite nonlinear. This means that neither any laser output power rectification nor any separate zero intensity recording is necessary with direct absorption. It means, though, that the frequency scale has to be linearized, and subsequently this was done for all the spectra shown in the remaining part of this paper.

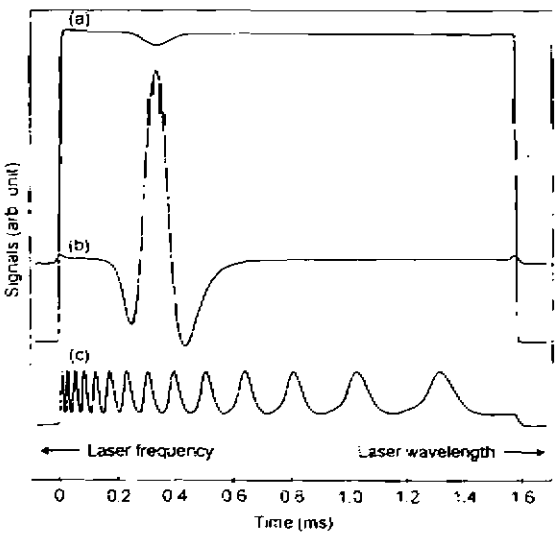

Fig. 2. (a) Direct absorption and (b) TTFMS spectra of the $4s\ ^2S_{1/2}$–$5p\ ^2P_{3/2}$ line at 404.8 nm recorded with a rectangular current pulse. (c) Corresponding recording of the Fabry–Perot etalon fringes.

WMS and TTFMS line shapes for potassium vapor were recorded from ~90 °C to room temperature. In Fig. 3, linearized recordings at 60 and 30 °C, corresponding to peak absorptions of 1.6×10^{-3} and 6.7×10^{-5}, respectively, are displayed. Interference fringes, caused by reflections between the neutral-density filter and the detector surface, are clearly visible in the recording of the TTFMS line shape at 30 °C. Although FM spectroscopy offers the possibility of quantum-noise-limited detection, the minimum achievable sensitivity is in practice often set by

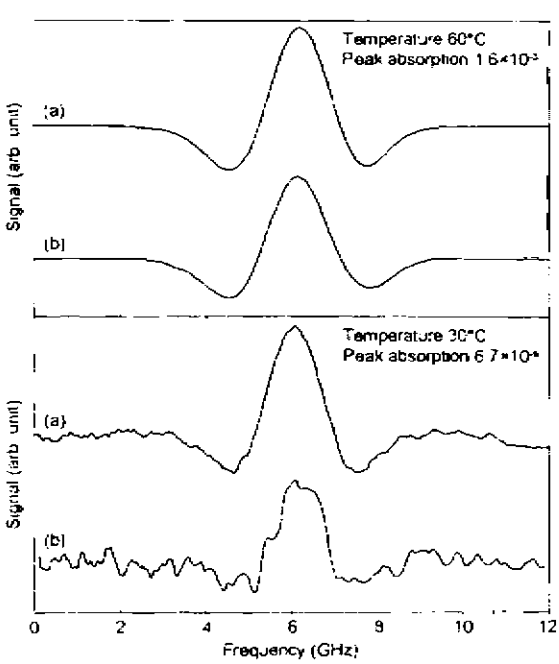

Fig. 3. Linearized (a) WMS and (b) TTFMS recordings for potassium at two cell temperatures.

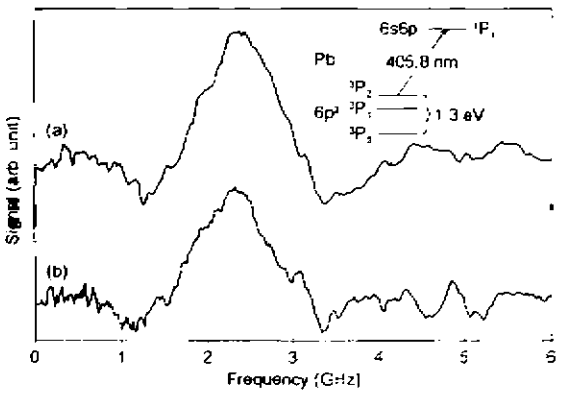

Fig. 4. Linearized (a) WMS and (b) TTFMS recordings of the lead 405.8-nm line. Inset, diagram of the structure of lead.

interference fringes that are seen as a periodically oscillating background and originate from spurious reflections along the laser beam path. The interference effect can often be removed or largely reduced by careful angling of all transmissive optics, and, as can be seen from the WMS recording in Fig. 3 [upper curve (a)], a slight adjustment of the neutral-density filter removes the interference fringes.

It is necessary to perform experiments at considerably higher temperatures if one wishes to observe the absorption in lead, because of the low vapor pressure of this metal. We studied the transition at 405.8 nm, starting from the thermally weakly populated $6p^2\ ^3P_2$ metastable level situated 1.3 eV above the ground state. The lead experiments were performed at temperatures that ranged from 500 to 700 °C, corresponding to ground-state atomic densities of 2×10^{17} m^{-3} to 7×10^{19} m^{-3} and to Boltzmann factors of 2×10^{-8} to 9×10^{-7}. These atomic densities can be compared with those in the potassium cell, which range from 3×10^{14} m^{-3} (20 °C) to 3×10^{17} m^{-3} (90 °C). The lead gas cell contains a natural mixture of lead isotopes, but the specific measurements were performed on the transition corresponding to the ^{208}Pb isotope with a nuclear spin of 0. The isotope, which has no hyperfine splitting because of the zero nuclear spin, has a Doppler width of ~550 MHz.

The linearized WMS and TTFMS recordings at 600 °C (peak absorption, 2.0×10^{-4}) are shown in Fig. 4. These recordings were also influenced by interference fringes that originated from a reflection from the detector surface back into the diode laser cavity. Despite cautious angling of all optics as well as of the diode laser and the detector, we were not able to suppress completely the interference fringes in the lead experiments. We explain the difference in the results of the experiment with potassium from that with lead as being due to different diode laser behaviors at the two wavelengths because different current and temperature settings were used. Another unwanted and limiting effect in the lead experiments is a diode laser mode jump close to the transition on the low-frequency side. The frequency position of the mode jump varies in time, and this variation adds an irregular background to the recorded line shapes.

4. Results and Discussion

Here we first determine the modulation parameters in WMS and TTFMS by means of a fitting procedure of the recorded line shapes. Then we use these modulation parameters to calculate the theoretical SNR's and compare them with the experimentally deduced SNR's. Finally, we estimate the maximum achievable sensitivity of this blue diode laser–based spectrometer. The evaluation was performed mainly with the experimental data for potassium, because, as we noted above, the lead experiments were hampered by interference fringes and a diode laser mode jump, in which case, the SNR was set by these effects rather than by the fundamental noise sources in a FM spectrometer. The formalism that describes the FM theory, including calculations of WMS and TTFMS line shapes and SNR's, can be found, e.g., in Refs. 22 and 24–26.

FM of diode lasers is always accompanied by residual amplitude modulation (RAM), which is noticeable in WMS and TTFMS recordings as a line-shape asymmetry. This RAM, which is accounted for in the FM theory by the AM index M and the AM–FM phase difference ψ, is an effect that is caused by the laser intensity not being exactly uniform over the FM range, and it is undesirable because it carries some of the low-frequency noise into the FM signal. The AM index and the AM–FM phase difference are closely connected in theory and are difficult to determine independently. A value of $\psi = \pi/2$ for the AM–FM phase difference is generally considered to be a good approximation for diode lasers,[22,27,28] and, in what follows, we adopt this value.

As we mentioned above, the studied transition in potassium actually consists of several hyperfine components. These can be divided mainly into two Gaussians that have a half-width given by the Doppler width, are separated by 462 MHz and have an intensity ratio of 5/3, which is equal to the statistical weights of the two hyperfine ground-state levels ($F = 2$ and $F = 1$). The FM index, designated β in the FM nomenclature, and the AM index M were determined by fits to the WMS and TTFMS line shapes recorded at different temperatures. The parameters obtained were $\beta = 230$ and $M = 0.045$ for WMS and $\beta = 1.0$ and $M = 0.035$ for TTFMS. With these parameter values, two curves were calculated, and they and their sum are displayed in Fig. 5, together with the potassium line experimentally recorded at 80 °C.

The AM–FM index ratio M/β is an intrinsic property of a diode laser and depends on the modulation frequency and the bias current.[29] Typically, the ratio scales with the modulation frequency, and for our experiments with equal bias current for WMS and TTFMS the ratio of the AM–FM index ratio for TTFMS and WMS was 179, which is in excellent agreement with the ratio of the modulation frequencies, 181.

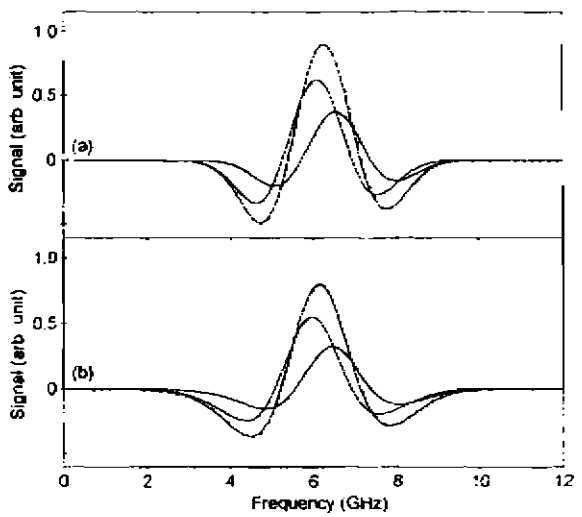

Fig. 5. Observed (symbols) and calculated (solid curves) line shapes for (a) WMS and (b) TTFMS of the potassium transition. The modulation parameters are $\beta = 2.30$ and $M = 0.045$ for WMS and $\beta = 1.0$ and $M = 0.035$ for TTFMS.

It can be observed from the experimental data that the signals (peak-to-peak value) in WMS are approximately 20% higher than those of TTFMS; see Fig. 3–5. This result agreed well with the theoretically calculated signal values that yielded a signal difference for the temperatures employed of ~21% for potassium and ~23% for lead. No modulation broadening is observed in either the WMS or the TTFMS line shape. This result is consistent with the experimentally applied rf powers, which we carefully adjusted for the highest signal amplitudes achievable without introducing modulation broadening. The presence of modulation broadening would make the fitting procedure more difficult and less accurate. WMS and TTFMS line shapes that were optimized only for maximum signal amplitudes showed considerable modulation broadening.

In a frequency-modulated system the power SNR_P can be expressed as[25]

$$SNR_P = \frac{\langle i_s(t)\rangle^2}{i_{sn}^2 + i_{th}^2 + i_{RAM}^2 + i_{ex}^2} = \frac{\left(\frac{e\eta}{h\nu}\right)^2 2(P_0)^2 Q(\alpha, \varphi)|^2}{2\frac{e^2\eta}{h\nu}\langle P_0\rangle\left(1 + \frac{M^2}{2}\right)^N \Delta f + \frac{4kT}{R_L}\Delta f + \left(\frac{e\eta}{h\nu}\right)^2 2R(M)\sigma_p^2 + \left(\frac{e\eta}{h\nu}\right)^2 \frac{\Delta f}{f^b}\sigma_{ex}^2}, \quad (1)$$

where the terms in the two expressions are in the same order and where the mean-squared noise currents in the denominator (from left to right) are related to laser-induced detector shot noise, detector and amplifier thermal noise, AM-induced (RAM) noise, and laser source or excess noise and the term in the numerator is the time-averaged mean-squared detector current. e is the charge of the electron, η is the detector quantum efficiency, h is Planck's constant, ν is the transition frequency, P_0 is the laser power, $Q(\alpha, \varphi)$ is a signal that is due to absorption α and dispersion φ, M is the AM index, N is the number of modulating tones, Δf is the detection bandwidth, k is Boltzmann's constant, T is the absolute temperature of the detector, R_L is the resistance of the detection system, $R(M)$ is the RAM function, σ_p is the standard deviation of the laser power within the noise equivalent bandwidth of the detector system, f is the detection frequency, and σ_{ex} is a system-dependent constant that is defined as the laser power fluctuations at 1-Hz bandwidth at 1-Hz frequency. The value of the exponent b is typically 1.0 but can range from 0.8 to 1.5.

The absorption- and dispersion-related line-shape function $Q(\alpha, \varphi)$, which depends on M, β and ψ, is calculated as the peak-to-peak value of the absorption component of the WMS and TTFMS line shapes because the dispersion component vanishes as a result of our choice of detection phase. The RAM function describes the nonzero signal that is detected even in the absence of absorption and is due to the AM. The reason for employing second-harmonic detection instead of first-harmonic detection in WMS is that the influence of RAM will be decreased. For WMS and second-harmonic detection, $R(M) = 1/4\,M^2 \cos(2\psi + \pi)$; for TTFMS, $R(M) = M^2$. The total power impinging upon the detector is $P_0 = 3$ mW, and the parameters for detector and detection electronics in our setup are $\eta = 0.37$ and $R_L = 50\ \Omega$. From direct absorption measurements, a value of $1 \times 10^{-3}\,P_0$ for the parameter σ_p was deduced. The only adjustable parameter in the SNR calculations is σ_{ex}, and its value is estimated to be $4.5 \times 10^{-4}\,P_0$. These values of σ_p and σ_{ex} are approximately 1 order of magnitude higher than typical values for diode lasers used for FM in the near infrared and the infrared.[10,14] We attribute the difference to the multimode behavior of our blue diode laser.

The experimental SNR is calculated as the ratio of the line-shape peak-to-peak value to the noise rms value. Inasmuch as we measure voltage and not power, the experimental SNR is related to the theoretical voltage SNR_V, which is given by $SNR_V = (SNR_P)^{1/2}$. In Fig. 6 the experimental SNR's for

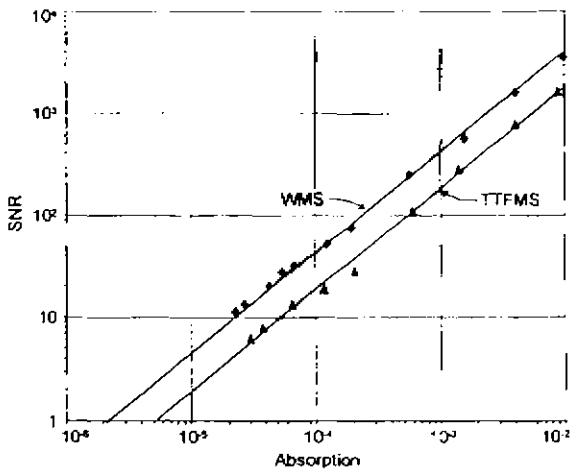

Fig. 6. Experimentally deduced SNR's for WMS (diamonds) and TTFMS (triangles) for potassium together with theoretical curves calculated from Eq. (1) and the parameter values mentioned in the text.

WMS and TTFMS are presented, together with the theoretical SNR curves. Clearly, absorption signals for less than the smallest experimentally recorded absorption of 2×10^{-5} (at -20 °C) are detectable, but with our current setup it is not possible to cool the gas cell and record signals below room temperature. The sensitivity limits that can be deduced are 2×10^{-6} for WMS and 5×10^{-6} for TTFMS. In the lead experiments we were able to record WMS and TTFMS signals down to a SNR of 1, which occurs at temperatures of -500 °C and corresponds to an absorption of 5×10^{-5}. Thus the interference fringes and the mode jump limit the detection sensitivity by -1 order of magnitude.

There are two reasons for the approximately two-times better SNR in WMS than in TTFMS. The first is the higher signal amplitude in WMS, and the second is the higher RAM noise level in TTFMS, as expected from the different RAM dependencies given by the RAM function. All other noise sources have the same amplitude in WMS and TTFMS. The ratio of the shot noise, the thermal noise, the laser excess noise, the TTFMS RAM noise, and the WMS RAM noise is 1:1.7:0.7:5.4:2.2. These numbers clearly show that TTFMS is essentially limited by RAM noise, whereas the sensitivity in WMS is set by both RAM and thermal noise. We also note that the laser excess noise is below the shot noise and that the main purpose for employing FM is achieved. RAM noise and, as a consequence of the technique, laser excess noise can be greatly reduced by the use of balanced homodyne detection.[13,15,21] However, the power transmitted through the absorbing medium is halved and the thermal noise is doubled in this technique. Theoretical calculations of the SNR's in balanced homodyne detection, with the same parameter values as above, show that the SNR's for TTFMS are almost the same but that the SNR's for WMS are lower, as we also verified experimentally. The results obtained in the present study are broadly in line with those obtained in previous comparisons of the sensitivity of various modulation schemes in which infrared lead-salt diode lasers[10] and near-infrared GaAlAs diode lasers[11] were used.

A possible extension of the present study would be to monitor NO_2, which has strong absorption bands in the wavelength region about 400 nm. At atmospheric pressure these transitions are much broader than for potassium and lead and might also partially overlap. Such a study would require continuous scans of the order of 50 GHz, which at present are not feasible with the diode laser used. One should also note that the multimode behavior of the diode laser does not influence the spectral appearance for free atoms with isolated spectral features as in our case, because only one of the oscillating modes interacts with the atoms. However, for molecules with a multitude of close-lying lines, multimode behavior is, of course, unacceptable. As the blue diode laser used is a prototype laser, we believe that later versions will be better suited for spectroscopy, i.e., will operate in a single mode. One can use an external-feedback cavity to ensure single-mode operation and large frequency-tuning ranges, but doing so will limit the high-FM capabilities and thus the detection sensitivity.

5. Conclusions

We performed FM spectroscopy on potassium and lead, using a blue diode laser. We made highly sensitive absorption measurements in this new and interesting diode-laser wavelength region, employing WMS and TTFMS. In fits to experimental data the modulation parameters for the blue diode laser used in our experimental setup were determined. We have shown that experimentally deduced SNR's are in good agreement with theoretically calculated SNR's. Additionally, various noise sources were examined, and we have concluded that TTFMS is dominated by RAM noise, whereas WMS is limited by both RAM and thermal noise. A minimum detectable absorption of 2×10^{-6} for WMS and 5×10^{-6} for TTFMS in a 120-Hz detection bandwidth was observed. By sum-frequency mixing blue and red diode lasers, even shorter emission wavelengths can be achieved, further extending the possibilities for sensitive absorption spectroscopy of many atomic and molecular transitions.[30]

This study was supported by the Swedish Research Council for Engineering Sciences (TFR) and the Knut and Alice Wallenberg Foundation. J. Alnis thanks the Swedish Institute for a stipend supporting his stay in Sweden.

References

1. P. Werle, R. Mücke, F. D. Amato, and T. Lancia, "Near-infrared trace-gas sensor based on room-temperature diode lasers," Appl. Phys. B **67**, 307–315 (1998).
2. G. Modugno, C. Corsi, M. Gabrysch, and M. Inguscio, "Detection of H_2S at ppm level using a telecommunication diode laser," Opt. Commun. **145**, 76–80 (1998).

3. H. Riris, C. B. Carlisle, D. F. McMillen, and D. E. Cooper, "Explosives detection with a frequency modulation spectrometer," Appl. Opt. **35**, 4694–4704 (1996).
4. J. A. Silver, D. J. Kane, and P. S. Greenberg, "Quantitative species measurements in microgravity flames with near-IR diode lasers," Appl. Opt. **34**, 2787–2801 (1995).
5. P. Kauranen, H. M. Hertz, and S. Svanberg, "Tomographic imaging of fluid flows by the use of two-tone frequency-modulation spectroscopy," Opt. Lett. **19**, 1489–1491 (1994).
6. P. Kauranen, I. Harwigsson, and B. Jönsson, "Relative vapor pressure measurements using a frequency-modulated tunable diode laser, a tool for water activity determination in solutions," J. Phys. Chem. **98**, 1411–1415 (1994).
7. E. G. Moses and C. L. Tang, "High sensitivity laser wavelength modulation spectroscopy," Opt. Lett. **1**, 115–117 (1977).
8. G. C. Bjorklund, "Frequency-modulation spectroscopy: a new method for measuring weak absorptions and dispersions," Opt. Lett. **5**, 15–17 (1980).
9. G. R. Janik, C. B. Carlisle, and T. F. Gallagher, "Two-tone frequency-modulation spectroscopy," J. Opt. Soc. Am. B **3**, 1070–1074 (1986).
10. D. S. Bomse, A. C. Stanton, and J. A. Silver, "Frequency modulation and wavelength modulation spectroscopies: comparison of experimental methods using a lead-salt diode laser," Appl. Opt. **31**, 718–731 (1992).
11. F. S. Pavone and M. Inguscio, "Frequency- and wavelength-modulation spectroscopies: comparison of experimental methods using and AlGaAs diode laser," Appl. Phys. B **56**, 118–122 (1993).
12. D. E. Cooper, R. U. Martinelli, C. B. Carlisle, H. Riris, D. B. Bour, and R. J. Menna, "Measurement of $^{12}CO_2$: $^{13}CO_2$ ratios for medical diagnostics with 1.6-μm distributed-feedback semiconductor diode lasers," Appl. Opt. **32**, 6727–6731 (1993).
13. G. Modugno, C. Corsi, M. Gabrysch, F. Marin, and M. Inguscio, "Fundamental noise sources in a high-sensitivity two-tone frequency modulation spectrometer and detection of CO_2 at 1.6 μm and 2 μm," Appl. Phys. B **67**, 289–296 (1998).
14. C. B. Carlisle, D. E. Cooper, and H. Preier, "Quantum noise-limited FM spectroscopy with a lead-salt diode laser," Appl. Opt. **28**, 2567–2576 (1989).
15. C. B. Carlisle and D. E. Cooper, "Tunable-diode-laser frequency-modulation spectroscopy using balanced homodyne detection," Opt. Lett. **14**, 1306–1308 (1989).
16. P. Werle, F. Slemr, M. Gehrtz, and C. Bräuchle, "Quantum-limited FM-spectroscopy with a lead salt diode laser," Appl. Phys. B **49**, 99–108 (1989).
17. M. Gehrtz, G. C. Bjorklund, and E. A. Whittaker, "Quantum-limited laser frequency-modulation spectroscopy," J. Opt. Soc. Am. B **2**, 1510–1526 (1985).
18. S. Nakamura and G. Fasol, *The Blue Laser Diodes* (Springer-Verlag, Heidelberg, 1997).
19. U. Gustafsson, J. Alnis, and S. Svanberg, "Atomic spectroscopy with violet laser diodes," Am. J. Phys. (to be published).
20. P. Kauranen and V. G. Avetisov, "Determination of absorption line parameters using two-tone frequency-modulation spectroscopy with diode lasers," Opt. Commun. **106**, 213–217 (1994).
21. V. G. Avetisov and P. Kauranen, "High-resolution absorption measurements using two-tone frequency-modulation spectroscopy with diode lasers," Appl. Opt. **36**, 4043–4054 (1997).
22. V. G. Avetisov and P. Kauranen, "Two-tone frequency-modulation spectroscopy for quantitative measurements of gaseous species: theoretical, numerical, and experimental investigation of line shapes," Appl. Opt. **35**, 4705–4723 (1996).
23. E. Arimondo, M. Inguscio, and P. Violino, "Experimental determinations of the hyperfine structure in the alkali atoms," Rev. Mod. Phys. **49**, 31–75 (1977).
24. D. E. Cooper and R. E. Warren, "Frequency modulation spectroscopy with lead-salt diode lasers: a comparison of single-tone and two-tone techniques," Appl. Opt. **26**, 3726–3732 (1987).
25. J. A. Silver, "Frequency-modulation spectroscopy for trace species detection: theory and comparison among experimental methods," Appl. Opt. **31**, 707–717 (1992).
26. J. M. Supplee, E. A. Whittaker, and W. Lenth, "Theoretical description of frequency modulation and wavelength modulation spectroscopy," Appl. Opt. **33**, 6294–6302 (1993).
27. W. Lenth, "High frequency heterodyne spectroscopy with current-modulated diode lasers," IEEE J. Quantum Electron. **QE-20**, 1045–1050 (1984).
28. S. Kobayashi, Y. Yamamoto, M. Ito, and T. Kimura, "Direct frequency modulation in AlGaAs semiconductor lasers," IEEE J. Quantum Electron. **QE-18**, 582–595 (1982).
29. M. Osinski and J. Buus, "Linewidth broadening factors in semiconductor lasers: an overview," IEEE J. Quantum Electron. **QE-23**, 9–29 (1987).
30. J. Alnis, U. Gustafsson, G. Somesfalean, and S. Svanberg, "Sum-frequency generation with a blue diode laser for mercury spectroscopy at 254 nm," Appl. Phys. Lett. **76**, 1234–1236 (2000).

dis 6

Sum-frequency generation with a blue diode laser for mercury spectroscopy at 254 nm

J. Alnis,[a] U. Gustafsson, G. Somesfalean, and S. Svanberg,[b]
Department of Physics, Lund Institute of Technology, P.O. Box 118, S-221 00 Lund, Sweden

(Received 28 October 1999; accepted for publication 12 January 2000)

Blue diode lasers emitting 5 mW continuous-wave power around 400 nm have recently become available. We report on the use of a blue diode laser together with a 30 mW red diode laser for sum-frequency generation around 254 nm. The ultraviolet power is estimated to be 0.9 nW, and 35 GHz mode-hop-free tuning range is achieved. This is enough to perform high-resolution ultraviolet spectroscopy of mercury isotopes. The possibility to use frequency modulation in the ultraviolet is demonstrated; however, at present the ultraviolet power is too low to give advantages over direct absorption monitoring. Mercury detection at atmospheric pressure is also considered which is of great interest for environmental monitoring. © *2000 American Institute of Physics.* [S0003-6951(00)02810-2]

Absorption spectroscopy using diode lasers is a fast and sensitive method for detection of many gases in atmospheric monitoring.[1] The technique has been widely employed in the mid-infrared spectral region (2–15 μm), where numerous species of interest have fundamental vibrational absorption bands, and in the near-infrared region (0.6–2 μm), where weaker overtone and combination bands occur. Near-infrared spectroscopy makes extensive use of low-cost and room-temperature operated diode lasers which are readily available in this wavelength region. Atomic trace element detection in, e.g., a graphite furnace,[2,3] using diode-laser based absorption is an attractive possibility. Midinfrared absorption measurements apply cryogenically cooled lead-salt diode lasers or utilize difference-frequency generation in a nonlinear crystal pumped by two near-infrared diode lasers.[4] Many species also have strong electronic transitions in the ultraviolet (UV) spectral region (200–400 nm). These transitions are typically one or two orders of magnitude stronger than the mid-infrared transitions. Additionally, interference from water vapor is less significant in the UV spectral region.

Mercury (Hg) is the only pollutant present as a free atom in the lower atmosphere and has a strong transition at 253.7 nm that allows detection at low concentrations. Typical background concentrations of mercury in air are a few ng/m^3,[5] but much higher mercury concentrations exist around mercury mining areas and chloralcali plants.[6] Zeeman absorption,[7] differential optical absorption spectroscopy (DOAS)[8] or light detection and ranging (Lidar)[6] techniques are used for mercury measurements in air. A diode-laser-based spectrometer in the UV region could be especially interesting for low absorption measurements, since modulation techniques,[9,10] which give several orders higher sensitivity compared to direct absorption, can be easily employed.

The access to the UV spectral region employing diode lasers is usually provided by quadrupling[11–13] or sum-frequency generation.[14] The sum-frequency generation is generally conducted in two successive stages. The first stage is frequency doubling of a near-infrared diode laser output, and the second stage is mixing the second harmonic with another or the same near-infrared diode laser. The nonlinear conversion efficiency can be increased by mode locking an external-cavity laser based on a high-power tapered semiconductor amplifier.[11,12,14] A spectral linewidth of about 100 GHz is usually obtained, and that is typically 100 times larger than the required resolution for spectroscopic measurements. Another method to increase the conversion efficiency is to place the nonlinear crystal in an external buildup resonator.[13] This generates relatively high UV powers (~2 mW), but suffers from limited continuous tuning range and increased system complexity.

Very recently Nichia Corporation introduced blue diode lasers[15] and we have studied the possibility to use them for potassium and lead spectroscopy.[16,17] At present we report on the generation of UV radiation around 254 nm for mercury spectroscopy based on frequency mixing of a blue diode laser and a red diode laser.

The setup for sum-frequency generation is shown in Fig. 1. The blue diode laser (Nichia NLHV500 with a nominal wavelength of 404 nm at 25 °C and a free-running output power 5 mW) was operated in a Littrow-type cavity that ensured single-mode operation and less sensitivity to back reflections. We used a Thorlabs system based on a diode laser mount (TCLDM9), a piezoelectric mirror mound (KC1-PZ) and a 2400 l/mm grating (Edmund Scientific 43224).

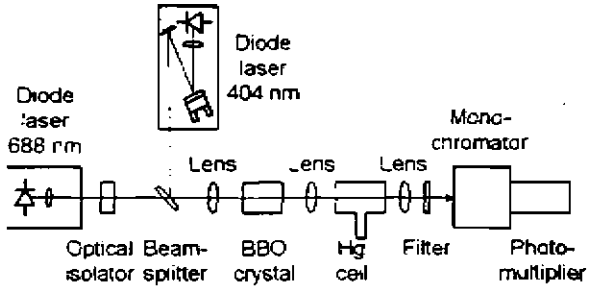

FIG. 1. Experimental setup for sum-frequency generation at 254 nm.

[a]Also with the Institute of Atomic Physics and Spectroscopy, University of Latvia, Rainis Blvd. 19, LV-1586 Riga, Latvia.
[b]Electronic mail: sune.svanberg@fysik.lth.se

The output power with the laser operated in the external cavity was 1 mW. The single-mode red diode laser (Toshiba TOLD 9150, 688 nm, 30 mW) was free-running and could be scanned continuously over 35 GHz by a current ramp. Moulded glass aspheric lenses with $f=4.5$ mm were used for collimation (Geltech C230TM). The diode lasers were temperature and current controlled using low-noise diode laser drivers (Melles Griot 06DLD 103). Both lasers were polarized vertically. An optical diode (OFR IO-5-NIR-I) was placed in the red diode laser beam to reduce backscattering from the nonlinear crystal. The blue and red beams were spatially overlapped via a dichroic beamsplitter and focused by a Nikon camera objective with a 50 mm focal length onto a 8-mm-long BBO crystal cut at $\theta=49°$ and $\varphi=90°$. Type I phase matching was achieved by tilting the crystal horizontally. A quartz lens of 50 mm focal length was used to collimate the UV light exiting the crystal. The detection side consisted of an $f=50$ mm quartz lens, a 254 ± 10 nm interference filter, a monochromator (Oriel 77250) tuned to 254 nm, and a photomultiplier (EMI 9558 QA). Without the monochromator a strong background existed from the not converted red and blue laser light. The signal from the photomultiplier was sent to a transimpedance amplifier (Itacho 1212) and a preamplifier (Stanford Research 560) and further to a signal averaging oscilloscope (Tektronix TDS520B).

It was not possible to measure the UV light power directly and we estimated it by photon counting. At optimized setup $n=5\times10^6$ pulses per second were counted. The quantum efficiency of the photomultiplier at $\lambda=254$ nm is $\eta=0.2$. That gives the UV power at the detector $P=nhc/(\lambda\eta)\approx2\times10^{-11}$ W. The two quartz lenses, the interference filter, and the monochromator had a transmission of 0.84, 0.28, and 0.09, respectively, thus the UV power after the crystal was about 0.9 nW.

From the theory of sum-frequency mixing of focused Gaussian beams and assuming a lossless crystal, the UV power can be expressed as[18,19]

$$P_3=\frac{4\omega_1\omega_2\omega_3 d_{\mathrm{eff}}^2 P_1 P_2 l h}{\pi\epsilon_0 c^4 n_3^2}, \tag{1}$$

where ω_i are the angular frequencies ($\omega_1<\omega_2<\omega_3$), P_i are the powers, n_i are the refractive indices of the crystal, d_{eff} is the effective nonlinear coefficient, l is the crystal length, and h is a dimensionless focusing parameter. The effective nonlinear coefficient was calculated to $d_{\mathrm{eff}}=1.59\times10^{-12}$ m/V according to the expressions in Ref. 20, and from the plots presented in Ref. 18 for the focusing parameter, we estimated $h=0.01$. Using the measured input powers (measured after the camera objective lens to $P_1=0.76$ mW and $P_2=25$ mW) and accounting for the approximately 7% reflection losses at the crystal input and output faces, we calculated a theoretically generated UV power $P_3=1.9$ nW. We believe that the approximately 2 times smaller UV power experimentally observed is due to imperfect overlap of the two input beams.

The spectrum of a natural isotopic mixture of mercury contains 5 peaks, that are formed by 10 Doppler-broadened transitions.[21,22] An absorption signal from a low pressure quartz cell containing a natural mixture of mercury is shown in Fig. 2(a). The spectrum was recorded by sweeping the red laser 35 GHz, and that resulted in an equally long scan in the UV. The mercury cell had a finger that was cooled by liquid nitrogen, because at room temperatures there was a 100% absorption on all the peaks. Absorption signals from two isotopically enriched low pressure cells with ^{204}Hg and ^{202}Hg are shown in Figs. 2(b) and 2(c), respectively. As a reference the designation and relative line strength of the isotope lines are displayed in Fig. 2(e).

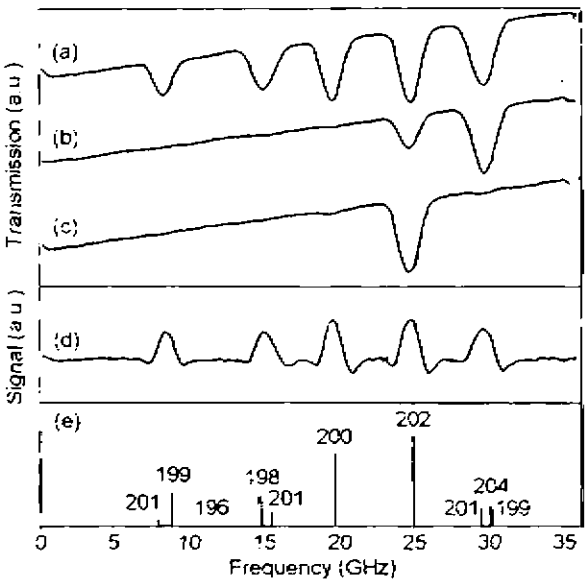

FIG. 2. Recorded UV absorption spectra from low pressure cells at −20 °C containing (a) natural isotope mixture of Hg, (b) enriched with ^{204}Hg, (c) enriched with ^{202}Hg, and (d) wavelength modulation signal from a natural isotope mixture of Hg. (e) Designation and relative strength of the Hg isotope lines according to Ref. 22.

The possibilities to use wavelength modulation in the UV region were also explored. A modulation frequency of 5 MHz was applied to the red diode laser through a bias tee. At the detection side the photomultiplier signal was amplified by a high frequency preamplifier and mixed with a frequency-doubled 5 MHz signal (standard radio-frequency components from Mini Circuits). The output from the mixer was low-pass filtered at 1 kHz, amplified and fed to the oscilloscope. Figure 2(d) shows the recorded second-harmonic ($2f$) signal. We also recorded low-frequency wavelength modulation signals at a few kilohertz frequency by modulating the external cavity grating angle with a piezo. Two-tone frequency-modulation signals with a setup used by our group extensively[17,23–27] were also recorded. Usually frequency modulation techniques have higher sensitivity compared to direct absorption, because the detection bandwidth is moved to higher frequencies, where laser excess ($1/f$) noise is very low, resulting in shot-noise limited measurements. At very low laser power though, as in our case, it is no advantage to use frequency modulation instead of direct detection.

At atmospheric pressures the isotope lines broaden and overlap to form a single absorption feature.[5,7] A scan of about 80 GHz is required to record the absorption at atmospheric pressures. Using our mode-hop-free scanning interval of 35 GHz we have measured the whole mercury absorption feature by recording three separate but overlapping scans. The recorded spectrum is shown in Fig. 3 together with a reference spectrum from a low-pressure cell. It can be

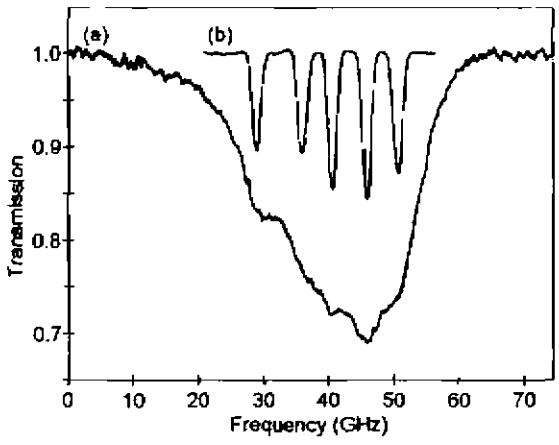

FIG. 3. (a) Hg absorption signal at atmospheric pressure in a 4 mm cell and (b) reference lines from a low pressure cell.

noted that since the isotope shifts are larger than the pressure-broadened linewidth (3.5 GHz obtained in a fit) individual isotope lines are clearly discernable in the recording at atmospheric pressure.

We have demonstrated the applicability of the recently available blue diode lasers for useful sum-frequency generation in the UV spectral region. High resolution absorption spectroscopy signals of mercury at 253.7 nm in a low pressure cell were recorded. Mercury detection at atmospheric pressure was performed, that is of great interest for trace element and environmental monitoring. The possibility to use different modulation techniques in the UV is demonstrated; however, at present the UV power is too low to give advantages over direct absorption monitoring. When higher UV powers become available through the fast development of diode lasers and nonlinear materials, the full power of our scheme combined with modulation techniques can be exploited.

This work was supported by the Swedish Research Council for Engineering Sciences (TFR) and the Knut and Alice Wallenberg Foundation. One of us (J.A.) would like to thank the Swedish Institute for a stipend supporting his stay in Sweden. The authors are grateful to A. Skudra for the loan of mercury isotope cells.

[1] H. I. Schiff, G. I. Mackay, and J. Bechara, in *Air Monitoring by Spectroscopic Techniques*, edited by M. W. Sigrist (Wiley, New York, 1994), pp. 239–333.
[2] P. Ljung and O. Axner, Spectrochim. Acta B **52**, 305 (1997).
[3] A. Zybin, C. Schnürer-Patschan, M. A. Bolshov, and K. Niemax, Trends Anal. Chem. **17**, 513 (1998).
[4] D. Richter, D. Glancaster, R. F. Curl, W. Neu, and F. K. Tittel, Appl. Phys. B: Lasers Opt. **67**, 347 (1998).
[5] S. H. Williston, J. Geophys. Res. **73**, 7051 (1961).
[6] H. Edner, G. W. Faris, A. Sunesson, and S. Svanberg, Appl. Opt. **28**, 921 (1989).
[7] J. Robbins, in *Geochemical Exploration*, edited by M. J. Jones (Institute of Mining and Metallurgy, London, 1973), p. 315.
[8] H. Edner, A. Sunesson, S. Svanberg, L. Unéus, and S. Wallin, Appl. Opt. **25**, 403 (1986).
[9] J. A. Silver, Appl. Opt. **31**, 707 (1992).
[10] D. S. Bomse, A. C. Stanton, and J. A. Silver, Appl. Opt. **31**, 718 (1992).
[11] L. Goldberg and D. A. V. Kliner, Opt. Lett. **20**, 1145 (1995).
[12] D. A. V. Kliner, J. P. Koplow, and L. Goldberg, Opt. Lett. **22**, 1418 (1997).
[13] C. Zimmerman, V. Vuletic, A. Hemmerich, and T. W. Hänsch, Appl. Phys. Lett. **66**, 2318 (1995).
[14] L. Goldberg and D. A. V. Kliner, Opt. Lett. **20**, 1640 (1995).
[15] S. Nakamura and G. Fasol, *The Blue Laser Diodes* (Springer, Heidelberg, 1997).
[16] U. Gustafsson, J. Alnis, and S. Svanberg, Am. J. Phys. (to be published).
[17] U. Gustafsson, G. Somesfalean, J. Alnis, and S. Svanberg (unpublished).
[18] G. D. Boyd and D. A. Kleinman, J. Appl. Phys. **39**, 3597 (1968).
[19] K. Sugiyama, J. Yoda, and T. Sakurai, Opt. Lett. **16**, 449 (1991).
[20] Y. X. Fan, R. C. Eckhardt, R. L. Byer, C. Chen, and A. D. Jiang, IEEE J. Quantum Electron. **QE-25**, 1196 (1989).
[21] W. Schweitzer, J. Opt. Soc. Am. **53**, 1055 (1963).
[22] R. Wallenstein and T. W. Hänsch, Opt. Commun. **14**, 353 (1975).
[23] P. Kauranen, H. M. Hertz, and S. Svanberg, Opt. Lett. **19**, 1489 (1994).
[24] P. Kauranen, I. Harwigsson, and B. Jönsson, J. Phys. Chem. **98**, 1411 (1994).
[25] P. Kauranen and V. G. Avetisov, Opt. Commun. **106**, 213 (1994).
[26] V. G. Avetisov and P. Kauranen, Appl. Opt. **35**, 4705 (1996).
[27] V. G. Avetisov and P. Kauranen, Appl. Opt. **36**, 4043 (1997).

dis 7

Analysis of gas dispersed in scattering media

M. Sjöholm, G. Somesfalean, J. Alnis, S. Andersson-Engels, and S. Svanberg

Department of Physics, Lund Institute of Technology, P.O Box 118, S-221 00 Lund, Sweden

Received August 7, 2000

Monitoring of free gas embedded in scattering media, such as wood, fruits, and synthetic materials, is demonstrated by use of diode laser spectroscopy combined with sensitive modulation techniques. Gas detection is made possible by the contrast of the narrow absorptive feature of the free-gas molecules with the slow wavelength dependence of the absorption and scattering cross sections in solids and liquids. An absorption sensitivity of 2.5×10^{-4}, corresponding to a 1.25-mm air column, is demonstrated by measurements of dispersed molecular oxygen. These techniques open up new possibilities for characterization and diagnostics, including internal gas pressure and gas-exchange assessment, in organic and synthetic materials. © 2001 Optical Society of America

OCIS codes: 300.6360, 290.7050, 290.5820, 170.3660, 020.3690, 160.4890.

We demonstrate, for what we believe to be the first time, how free gas dispersed in scattering materials can be detected and characterized by use of diode laser spectroscopy. The technique, provisionally denoted gas in scattering media absorption spectroscopy (GASMAS) opens up new possibilities for characterization and diagnostics of scattering solids and turbid liquids.

Many substances, frequently of organic origin, are porous and contain free gas that is distributed throughout the material. For instance, wood, plants, fruits, cheese, powders, sintered materials, and foams can be considered. A common way to analyze gas *in situ* is to use absorption spectroscopy that employs a sufficiently narrow-band light source in combination with the Beer–Lambertian law. However, the straightforward application of this method fails for turbid media, since the radiation is heavily scattered in the material containing the gas. Thus there are no well-defined path lengths as required by the Beer–Lambertian law, but light emerges diffusely. This situation has been much discussed in connection with light propagation in living tissue, which has applications to optical mammography,[1–3] dosimetry for photodynamic therapy,[4] and concentration determinations for tissue and blood constituents.[5,6]

In this Letter we consider solid or fluid bulk materials containing pockets or small bubbles of gas. Light scattering is caused by inhomogenities in the optical properties of the medium. Even in the case of a clear liquid containing fine bubbles of gas, e.g., beer, a diffuse refraction occurs.[7] In the case of strong scattering, which is the most interesting aspect of the proposed gas-detection technique, a long effective path length is achieved, giving rise to a strong gas signature. Clearly, the gas-containing medium should not have substantial absorption of radiation in the wavelength range needed for monitoring of the particular gas. A consequence of this restriction is that materials containing liquid water, e.g., substances derived from living organisms, can be investigated only up to a limiting wavelength of $\sim 1.4\ \mu m$. Generally, absorption and scattering properties of solids and liquids have a very slow wavelength dependence. In contrast, free gas exhibits extremely sharp absorptive features. Thus bulk material will not influence the detected radiation when the frequency of a single-mode probing laser is slightly changed, whereas embedded gas gives rise to a tiny but narrow signal that can be picked up by use of modulation techniques even in the presence of a large background.

Diode lasers are particularly convenient sources of tunable radiation. Tunable diode lasers can easily be wavelength modulated by addition of an ac component to the driving current and are very suitable for monitoring of small but sharp absorptive features.[8] Modulation techniques can be used to increase detection sensitivity by typically several orders of magnitude compared with that of direct absorption.[9,10]

Two basic geometries can be considered when one is performing measurements with the proposed technique. In Fig. 1(a), a transillumination arrangement is presented, and in Fig. 1(b), a backscattering detection scheme is shown. In both cases optical fibers can be used for light injection and for collection of scattered radiation. In a medium with a homogeneous distribution of gas, the "history" of the photons

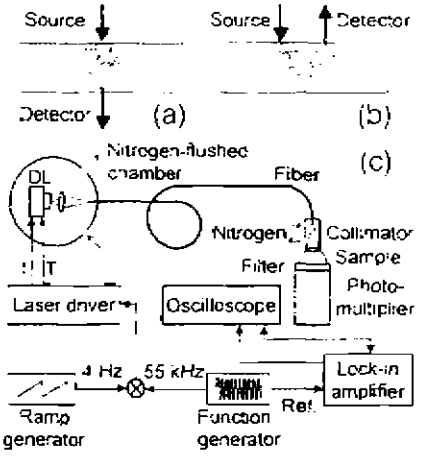

Fig. 1. (a), (b) Basic geometrical arrangements for monitoring of free gas in scattering media. (c) Experimental setup of the initial experiments. DL, diode laser; I, current; T, temperature control; Ref., reference.

0146-9592/01/010016-03$15.00/0

can partially be followed by measurement of the relative amplitude of the sharp gas-absorption signal, which increases with the path length. The absorption and scattering properties of the bulk material can be deduced independently by spatially resolved, time-resolved, or frequency-domain measurements, as is frequently done in tissue optics studies.[3] Thus a mean path length of the impinging photons through the scattering material can be estimated, which together with the magnitude of the gas absorption determines the concentration of the dispersed gas.

In our exploratory proof-of-principle measurements we used the setup shown schematically in Fig. 1(c). A tunable diode laser with a nominal wavelength of 757 nm at 25 °C and a free-running output power of 7 mW was used as a spectroscopic source for molecular oxygen monitoring. The spectroscopic measurements were performed on a double line near 759.95 nm ($R17Q18$ and $R19R19$) as well as on a strong isolated line at 761.003 nm ($R7R7$). These lines belong to the oxygen A band and were within the wavelength range of the diode laser that we used. Since oxygen is abundant in normal air, we placed the laser and a lens that focused the radiation into a 600-μm quartz fiber in a nitrogen-flushed chamber to eliminate spurious oxygen signals. At the other end of the fiber, the output light was collimated by another lens fixed in a nitrogen-flushed adapter. Since the transmitted light intensities through the samples were usually very low, it was important to ensure high detection sensitivity. Thus a photomultiplier tube with a 50-mm-diameter photocathode was used for detection. The ambient room light was effectively suppressed by a Schott RG695 colored-glass long-pass filter attached directly to the photocathode, in combination with the sensitivity falloff of the photomultiplier tube toward longer wavelengths. The samples were placed directly between the colored-glass filter and the collimating lens, which could be freely positioned by a fine translation stage. The diode laser was operated in a thermoelectrically cooled mount and was current and temperature controlled by a precision diode laser driver. Wavelength scanning was achieved by repetitive application of a current ramp with a repetition rate of 4 Hz to the drive current, whereas a sinusoidal current at 55 kHz was superimposed for wavelength modulation of the diode laser. The photomultiplier tube signal was picked up phase-sensitively by a lock-in amplifier. The extracted second-harmonic component and the direct signal were then accumulated for 256 scans in a digital oscilloscope.

Experiments were performed on a variety of samples of different thicknesses. Data for a piece of dried pine wood are shown in Figs. 2(a) and 2(b). Measurements were performed with the collimator lens of the transmitter initially in contact with the surface of the sample and then retracted to add several free air paths of well-defined lengths. The oxygen contained in the scattering medium could be evaluated as illustrated in Fig. 2(a) by use of the standard addition method, which is well known from physical chemistry. Since the absorption is of the order of a few percent, the signal is expected to depend linearly on the concentration. An equivalent mean path length in the sample, i.e., the mean distance that light travels through air dispersed in the sample, can be evaluated. For determination of the sensitivity of the oxygen concentration measurement, the specific absorption of oxygen was also measured in air with the laser beam strongly attenuated by a neutral-density filter. We also calibrated the wavelength-modulation signal by use of long-path direct absorption in air (measurable at a path length of 4.5 m), given the atmospheric oxygen concentration of 20.8%. In the present experiments we were able to detect an absorbance of 2.5×10^{-4}, which corresponds to a 1.25-mm column of air.

The signal that was due to oxygen dispersed in a 26-mm-thick slice of apple is displayed in Fig. 2(c), which shows that liquid water does not pose problems for measurement in this wavelength region. Finally, Fig. 2(d) shows signals from a bulk of turbid epoxy glue containing air bubbles embedded at an ambient pressure of 300 mbars. The pressure dependence of the line shape can clearly be seen, illustrating the potential of the technique for internal pressure assessment, e.g., in porous mineral samples or sintered ceramics. Measurement data for different samples are compiled in Table 1, in which the thicknesses of the samples are also given. Note that the evaluated air equivalent mean path lengths through the different samples are often several times longer than the geometrical dimension but can also be shorter, as in epoxy.

Our experiments show that it is possible to monitor small and sharp absorptive features that are due to free gas in strongly scattering solids by use of sensitive diode laser spectroscopy. Many applications of this new type of scattering spectroscopy for solids and

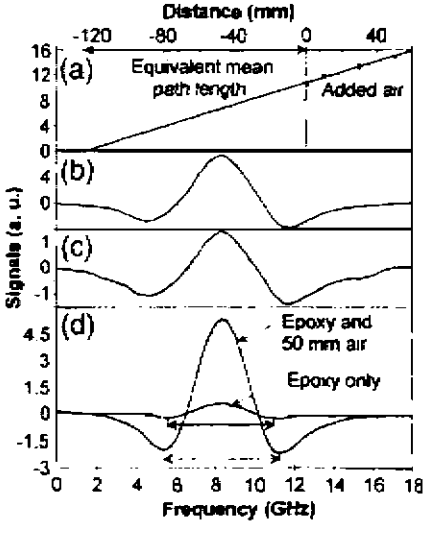

Fig. 2. Experimental data for lines in the molecular oxygen A band obtained by wavelength-modulation diode laser spectroscopy. (a) Standard addition plot for a 10-mm-thick piece of wood, (b) corresponding recorded line shape for wood only, (c) spectral recording for a 26-mm-thick slice of apple, and (d) spectra for a 19-mm-thick bulk of turbid epoxy containing air bubbles at low pressure and when 50 mm of background air is added. The isolated molecular oxygen line was used in these last two recordings.

Table 1. Equivalent Mean Path Lengths for Oxygen-Containing Porous Media of Various Thicknesses

Material	Thickness (mm)	Equivalent Mean Path Length (mm)
Wood	10	123
Apple	26	33
Lump sugar	12	20
Granulated salt	18	170
Wheat flour	18	380
Polystyrene foam	19	600
Turbid epoxy	19	5

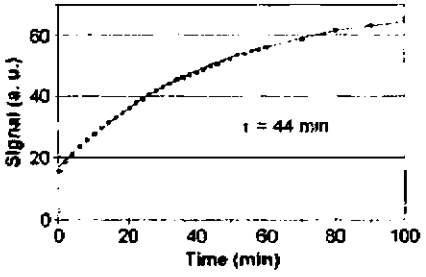

Fig. 3. Recording of the oxygen-signal increase of a 19-mm-thick piece of polystyrene foam while it is kept in ambient air but after it has been stored in a pure nitrogen atmosphere.

liquids can be envisaged. By use of these techniques it would be possible to monitor *in situ* physiological and degradation processes in various biological substances. Such measurements have been limited to extraction of emitted gas from, e.g., plants, fruits, and insects, measured by normal gas spectroscopic techniques.[11,12] The largest challenge would be to develop methods for monitoring minute amounts of free gas inside human tissue, possibly allowing development of new diagnostic techniques for diseases.

The new possibility of observing free gas in scattering media allows not only static gas assessment but also the study of dynamic processes, i.e., how embedded gas is exchanged with the environment. For instance, an object can be surrounded by a gas, and the successive gas penetration into the object can be studied. This example is demonstrated in Fig. 3. A piece of polystyrene foam was first subjected to a pure nitrogen atmosphere for 4 h. Invasion of oxygen into the material was observed to occur with a time constant ($1/e$) of 44 min. This experiment suggests that radioactive labeling can sometimes be replaced by the new technique.

In the limit of very small (nanometer-scale) enclosures of free gas, additional collisional broadening and shifts of diagnostic value can be expected. Note also that tomographic reconstruction of the gas distribution in the material is possible by use of multiple fibers placed around the object.

Quantifying and fully exploiting diagnostic aspects of gas in scattering media require full modeling of the multiple-scattering material. The theoretical and experimental techniques developed for medical applications are useful in this respect.[2,13] Time-resolved measurements are particularly powerful, providing a direct and independent assessment of photon history.[1,14,15]

The authors gratefully acknowledge the assistance of U. Gustafsson in setting up the oxygen spectrometer and of J. Sandsten in HITRAN spectral identifications. This work was supported by the Swedish Research Council for Engineering Sciences, the Knut and Alice Wallenberg Foundation, and the Swedish Institute. S. Svanberg's e-mail address is sune.svanberg@fysik.lth.se.

References

1. S. Andersson-Engels, R. Berg, S. Svanberg, and O. Jarlman, Opt. Lett. **15**, 1179 (1990).
2. G. Müller, B. Chance, R. Alfano, S. Arridge, J. Beuthan, E. Gratton, M. Kaschke, B. Masters, S. Svanberg, and P. van der Zee, eds., *Medical Optical Tomography: Functional Imaging and Monitoring*, Vol. 11 of SPIE Institute Series (Society of Photo-Optical Instrumentation Engineers, Bellingham, Wash., 1993).
3. J. C. Hebden, S. R. Arridge, and D. T. Delpy, Phys. Med. Biol. **42**, 825 (1997).
4. W. M. Star, Phys. Med. Biol. **42**, 763 (1997).
5. Y. Mendelson, A. C. Clermont, R. A. Peura, and B.-C. Lin, IEEE Trans. Biomed. Eng. **37**, 458 (1990).
6. A. Roggan, M. Friebel, K. Dörschel, A. Hahn, and G. Müller, J. Biomed. Opt. **4**, 36 (1999).
7. N. E. Shafer and R. N. Zare, Phys. Today **44**(10), 48 (1991).
8. H. I. Schiff, G. I. Macay, and J. Bechara, in *Air Monitoring by Spectroscopic Techniques*, M. W. Sigrist, ed., Vol. 127 of Chemical Physics Series (Wiley, New York, 1994), Chap. 5.
9. J. A. Silver, Appl. Opt. **31**, 707 (1992).
10. D. S. Bomse, A. C. Stanton, and J. A. Silver, Appl. Opt. **31**, 718 (1992).
11. F. G. C. Bijnen, H. Zuckermann, F. J. M. Harren, and J. Reuss, Appl. Opt. **37**, 3345 (1998).
12. F. J. M. Harren, in *Encylcopedia of Analytical Chemistry: Applications, Theory and Instrumentation*, R. A. Meyers, ed. (Wiley, New York, 2000), pp. 2203–2226.
13. S. Andersson-Engels, R. Berg, and S. Svanberg, J. Photochem. Photobiol. **16**, 155 (1992).
14. B. Chance, J. S. Leigh, H. Miyake, D. S. Smith, S. Nioka, R. Greenfeld, M. Finander, K. Kaufmann, W. Levy, M. Young, P. Cohen, H. Yoshioka, and R. Boretsky, Proc. Natl. Acad. Sci. USA **85**, 4971 (1988).
15. R. Berg, O. Jarlman, and S. Svanberg, Appl. Opt. **32**, 574 (1993).

dis 8

Concentration measurement of gas imbedded in scattering media employing absorption and time-resolved laser spectroscopy

Gabriel Somesfalean, Mikael Sjöholm, Janis Alnis, Claes af Klinteberg, Stefan Andersson-Engels, and Sune Svanberg

Department of Physics, Lund Institute of Technology
P.O. Box 118, SE-221 00 Lund, Sweden

Abstract

Diode-laser-based absorption spectroscopy for evaluation of imbedded gas concentrations in porous materials is demonstrated in measurements of molecular oxygen dispersed throughout scattering polystyrene foam, here used as a generic test material. The mean path length of light scattered in the material is determined using the temporal characteristics of the radiation transmitted through the sample. This combined with sensitive gas absorption measurements employing wavelength modulation spectroscopy yields an oxygen concentration in polystyrene foam of 20.4% corresponding to a foam porosity of 98%, which is consistent with manufacturing specifications. This feasibility study opens up many possibilities for quantitative measurements using the method of gas-in-scattering-media absorption spectroscopy.

1. Introduction

Imbedded gas is often found in porous materials of both organic and synthetic origin. Monitoring of the distributed free gas can convey the internal gas concentration, pressure and temperature, and can reveal useful information about the bulk material, e. g., internal structure and diffusion characteristics. Recently, we have demonstrated a new technique, denoted gas in scattering media absorption spectroscopy (GASMAS),[1] used for the characterization and diagnostics of free gas in scattering solids and turbid liquids. First demonstrations included proof-of-principle measurements of the imbedded oxygen concentration relative to an equivalent column of air, of the internal gas pressure, and assessment of the gas exchange. The dispersed gas is analyzed *in situ* using absorption spectroscopy employing a single-mode probing diode laser tuned over a sharp absorption feature of the free gas molecule. The absorption and scattering cross sections of the bulk material display slow wavelength dependence, thus these properties can be assumed to be constant over the wavelength range tuned. Wavelength modulation techniques[2] are used to increase the detection sensitivity and to effectively discriminate against background signals, allowing for detection of around 10^{-4}-10^{-5} absorption fractions of the light received.[1]

Due to inhomogenities on the microscopic scale in the optical properties of the turbid medium, the radiation is scattered multiple times in the material. This prevents a straightforward application of the Beer-Lambert law, which requires well-defined path lengths. However, using a temporally resolved technique, as it is routinely done in tissue

optics studies,[3,4] a mean path length of the diffused light can be estimated, that together with the strength of the gas absorption determines the concentration of the dispersed gas. In this paper we demonstrate the possibility for quantitative concentration measurements using polystyrene foam as a generic test material.

2. Theoretical background

In order to extract the concentration of gas imbedded in a turbid sample, we employ two independent measurements to obtain the gas absorbance a and the absorption path length L, respectively. The Beer-Lambert law yields the transmitted intensity over a free path length L of a species having a concentration c and a wavelength-dependent absorption cross-section $\sigma(\lambda)$, according to

$$I(\lambda) = I_0(\lambda)e^{-\sigma(\lambda)cL} = I_0(\lambda)e^{-a}, \qquad (1)$$

where $I_0(\lambda)$ is the initial injected intensity and $I(\lambda)$ is the recorded intensity of the transmitted light. The gas absorbance is obtained using this equation by measuring the transmitted intensity through the sample at wavelengths on and off the gas absorption line. The expression cL can thus be determined from the transmission measurement, assuming the absorption cross section to be known. The optical path length in a scattering medium L_{sm} is, however, not simply the thickness of the sample, but is determined by the absorption and scattering properties of the material, as well as by the measurement geometry. Independent measurements of both the absorbance and the optical path length are thus required to obtain the concentration. The absorption of the gas is often very small as compared to the bulk material absorption, and will thus essentially not influence the optical path length. The influence of gas absorption on the optical path length is neglected below.

The absorption path length can be estimated as the mean path length traveled by the photons $\langle l \rangle$. Two different approaches can be used to determine the path length, by a direct time-resolved measurement, or indirectly by assessing the optical properties of the medium, making it possible to calculate L_{sm} with the use of a transport model for the light propagation within the sample. In the limit of small absorptions, the mean traveled path length can be estimated from the experimentally determined average time-of-flight of the photons $\langle t \rangle$, according to

$$L_{sm} = \langle l \rangle = v \langle t \rangle, \qquad (2)$$

where v is the velocity of light in the scattering material. The material optical properties can be assessed experimentally in three different ways: by time-resolved, spatially-resolved, and frequency-domain measurements.

In this work, the powerful technique of time-resolved measurements utilizing ultra-short light pulses and fast optical detection was used for studying photon propagation in multiple-scattering materials.[3,4] The analysis of the time-resolved data was based on the

diffusion approximation to the radiative transfer theory. When solving the diffusion equation, boundary conditions must be specified. In the case of simple geometries, such as a slab with finite thickness and infinite expansion, the most common approach is to mirror an infinite set of imaginary positive and negative isotropic sources in an extrapolated boundary at some distance beyond the actual surface, to insure that the fluence rate of photons is fully cancelled out. It yields an analytic expression for the transmitted pulse shape in terms of the absorption coefficient μ_a and the reduced scattering coefficient μ_s' of the sample material. In the case of an infinitely extended slab of scattering material, the time-dependent transmitted intensity can be expressed as[5]

$$I(\rho, d, t) = (4\pi Dv)^{-3/2}\, t^{-5/2} \exp\left(-\mu_a vt - \frac{\rho^2}{4Dvt}\right) \sum_{k=0}^{-\infty} \left\{ z_{-k} \exp\left(-\frac{r_{-k}^2}{4Dvt}\right) - z_{+k} \exp\left(-\frac{r_{-k}^2}{4Dvt}\right) \right\} \tag{3}$$

where ρ is the injection-detection separation, d is the slab thickness, $D = \left[3\left(\mu_a + \mu_s'\right)\right]^{-1}$ is the diffusion coefficient, $z_0 = \left(\mu_s'\right)^{-1}$ is the mean free path of isotropic scattering, $z_{\pm k} = (2k+1)d \pm z_0$ is the depth of the imaginary sources used to fulfill the boundary conditions, and $r_{\pm k} = \left(\rho^2 + z_{\pm k}^2\right)^{1/2}$ is the distance between the detector position and the sources used in the calculations. The optical properties of a sample can be evaluated by fitting such an analytical expression to the experimentally acquired temporal dispersion curve by adjusting the free parameters, the absorption and reduced scattering coefficients. For a slab of thickness d the expression for the average time-of-flight of the photons, calculated by integration of Eq. (3), is given by[6]

$$\langle t \rangle = \frac{\sum_{k=0}^{\infty} \left\{ \frac{z_{+k}}{r_{+k}} \exp\left(-\mu_{eff} r_{+k}\right) - \frac{z_{-k}}{r_{-k}} \exp\left(-\mu_{eff} r_{-k}\right) \right\}}{2vD \sum_{k=0}^{\infty} \left\{ \frac{z_{+k}}{r_{+k}^3} \left(1 + \mu_{eff} r_{+k}\right) \exp\left(-\mu_{eff} r_{+k}\right) - \frac{z_{-k}}{r_{-k}^3} \left(1 + \mu_{eff} r_{-k}\right) \exp\left(-\mu_{eff} r_{-k}\right) \right\}}, \tag{4}$$

where $\mu_{eff} = \left(\mu_a / D\right)^{1/2}$ is the effective attenuation coefficient. If the distribution of gas in the porous material is assumed to be homogeneous and the absorption is of the order of a few percent, the detected gas absorption signal can be considered to be the integrated contribution from all exiting photons. A typical theoretical time-dispersed curve for light transmitted through a 39 mm thick sample with the optical parameters μ_a = 0.002 cm^{-1} and μ_s' = 40 cm^{-1} is shown in Fig. 1. The broad time-of-flight distribution of the photons, corresponding to the absorption path lengths through the imbedded gas, give rise to varying absorption signal strengths, which are also schematically shown in the figure. Thus, the gas absorption can be used as a means to track the "history" of the photons in the material.

A simpler alternative to the time-resolved measurement technique, also explored in the present work, is to use a continuous-wave laser source and to spatially monitor the diffuse light intensity distribution at the sample surface.[7,8] When the recorded light intensity is plotted *versus*, e.g., the injection-detection separation distance, the final slope of the curve at large distances is found to be determined by the effective attenuation coefficient μ_{eff}. The spatially-resolved measurement method requires also that the absolute intensities of the injected and scattered light are measured, which may be difficult to perform experimentally because of unknown conditions regarding the coupling of light at the medium boundary. Solving the diffusion equation in the steady-state case yields a transmitted intensity for an infinite slab of scattering material

$$I(\rho, d) = \frac{1}{2\pi} \sum_{k=0}^{\infty} \left\{ \frac{z_{-k}}{r_{-k}^3} \left(1 + \mu_{eff} r_{-k}\right) \exp(-\mu_{eff} r_{-k}) - \frac{z_{+k}}{r_{+k}^3} \left(1 + \mu_{eff} r_{+k}\right) \exp(-\mu_{eff} r_{+k}) \right\}. \quad (5)$$

In our previous work on measurements of molecular oxygen,[1] we expressed the concentration of the gas in a scattering medium by introducing an equivalent mean path length L_{eq}. It is defined as the distance traversed by light in air, yielding a detected signal of the same magnitude as that from the absorption of photons by oxygen imbedded in the porous material, according to

$$c_{air} L_{eq} = c_{sm} L_{sm}, \quad (6)$$

where c_{air} is the oxygen concentration in air, and c_{sm} is the oxygen concentration in the scattering medium. The purpose of the present paper is to demonstrate quantitative gas concentration measurements. Thus, determination of an effective absorption path length can be performed by means of time- and spatially-resolved measurements.

3. Experimental

The experimental set-up for GASMAS measurements has been previously described in detail.[1] Basic experiments of the GASMAS type are conveniently performed on molecular oxygen, because this gas is normally diffused from the surrounding atmosphere into porous materials. A near-IR single-mode diode laser (Sharp LT031MDO) was placed in a nitrogen-flushed chamber and the light was brought to the sample through a 0.6 mm core diameter optical fiber, to ensure that the ambient air did not influence the measurements. A transilluminating geometry was chosen, in that the samples were placed on a long-pass colored-glass filter (Schott RG 695) attached directly to the cathode surface of a 2-inch-diameter photomultiplier tube (EMI 9558 QA). A very high sensitivity and a large dynamic range were achieved with this detector set-up, which is necessary when only small and variable amounts of light seep through the scattering materials under observation. In the measurements performed in this study, relatively high transmitted light intensities were available, and it was thus possible to spatially limit the detection area by using a mask with a circular aperture of 3 mm diameter. Spatially resolved measurements could thus also be performed.

The experiments were performed on the strong, isolated R7R7 line at 761.003 nm in the oxygen A band. Wavelength-modulation spectroscopy (WMS) employing lock-in techniques was used to pick up the second-harmonic component, which produces a signal similar to the second derivative of the original absorption lineshape. An experimental signal for oxygen in free air is shown in Fig. 2, where also a direct absorption recording is included. In our case, modulation at 55 kHz (Philips PM5139) effectively discriminated the background signals by shifting the detection band to a high-frequency region, where the noise level is low.[2] An absolute absorption calibration was established by performing a long-path measurement in free atmosphere, where the direct absorption signal could also be observed. The curves (a) and (b) in Fig. 2 are recordings obtained for a 10 m long absorption path length in air. In order to compensate for fluctuations in the detected light intensity, the experimental WMS signal, S_{WMS}, was normalized against the interpolated intensity of the diffused light at the line center, S_{Dir}, defining a GASMAS differential absorption signal

$$g \equiv \frac{S_{WMS}}{S_{Dir}}, \tag{7}$$

determined for the selected modulation parameters. Fabry-Pérot etalon fringes in Fig. 2(c) allow the oxygen linewidth to be evaluated to about 3.6 GHz.

Figure 3 shows a schematic diagram of the experimental set-up used for the time-resolved measurements. Two different laser sources were used for generation of picosecond long light pulses: a diode laser with a repetition rate of 10 MHz (Mitsubishi ML4405 with a Bios Quant DL4040 driver) and a mode-locked Ti:sapphire laser with a repetition frequency of 76 MHz (Coherent MIRA 900). Diode lasers are particularly convenient to use in such applications because of their simple operation, compact size, and possibility to produce short light pulses by applying high frequency components to the driving current. The average output power of the diode laser was 0.3 mW, while only a small fraction of the available radiation of the Ti:sapphire laser was used. Both lasers were tuned near to the selected absorption wavelength of oxygen around 761 nm. Due to the broadened linewidths of the short-pulsed lasers, the gas absorption has no significant influence on the photon propagation through the scattering medium. A transillumination arrangement was used, as shown in Fig. 3, although a backscattering detection scheme can in certain cases be more appropriate. Optical fibers with a core diameter of 0.6 mm were employed for light injection and for collection of scattered radiation, with the samples placed between the fiber ends. The injector-detector separation could be varied by translating the collecting fiber. The transmitted light was detected with a microchannel plate photomultiplier tube (Hamamatsu R2566U-07), which ensured a high detection sensitivity. The time-correlated single photon detection technique, including a constant fraction discriminator (CFD), a time-to-amplitude converter (TAC), and a multichannel analyser, was employed.[4,9] The photon arrival time distribution was recorded, and the overall temporal response function of the system was approximately 140 ps for the diode laser and 60 ps for the Ti:sapphire laser, respectively. The latter number corresponds essentially to the electronic response time, since the Ti:sapphire laser has sub-ps pulse length.

Spatially-resolved gas absorption measurements GASMAS combined with transmitted light intensity measurements were also performed using the transilluminating geometry. The incident beam diameter was 3 mm, and the receiving photomultiplier tube, with a detection area masked down to 3 mm diameter, could be translated side-ways.

The measurements were performed on polystyrene foam samples of different thicknesses but of the same kind. We have chosen polystyrene foam as a model scattering material, due to its relatively high homogeneity, strong scattering properties and high content of gas, i.e., factors that contribute to a strong gas signature. This material also has a great industrial and commercial importance since it is extensively used as an insulation and packaging material.

4. Results

Figure 4 shows the recorded photon arrival time distribution curve for a 39 mm thick slab of polystyrene foam measured using the diode laser. The time-response of the system itself, the apparatus function, was obtained at time t=0 using a separate fiber, transmitting part of the laser pulse directly to the detector (see Fig. 3). This signal also provided a time reference during the measurement. As can be seen from the time distribution curve, a certain fraction of the photons have traveled more than 15 ns through the material, i.e., corresponding to a path length of 4.5 m, although the physical thickness of the slab is only 0.039 m. The absorption and scattering coefficients of the polystyrene foam were determined by first convolving the solution of the diffusion equation, Eq. (3), to the impulse response of the system, and then fitting the resulting curve to the detected time dispersion curve, as shown in Fig. 4. Note that the scale is logarithmic, causing small discrepancies in the low intensity region at late times to be clearly visible. No extrapolated boundary condition was employed in the model due to resulting negligible corrections. In principle, laser-induced fluorescence could perturb the measurements. However, because of the long excitation wavelength, the fluorescence is negligible compared to the directly scattered light. The evaluated absorption coefficient is μ_a = 0.002 cm^{-1}, and the transport scattering coefficient is μ_s' = 40 cm^{-1}, yielding an effective attenuation coefficient μ_{eff} = 0.5 cm^{-1}.

Gas absorption spectroscopy data for a 9.4 mm thick slab of polystyrene foam embedded with atmospheric oxygen are shown in Fig. 5. It illustrates the amplitude variation of the GASMAS signal for several added free columns of air, and is used to estimate an extrapolated equivalent mean path length in polystyrene foam according to the standard-addition method. Since the fraction of light absorbed by the gas within the medium is small, corresponding to only a few percent of the incident light, the absorption signal g is approximately linearly proportional to the concentration. We denote the slope of the curve

$$k_{gL} \equiv \frac{g}{L}, \tag{8}$$

where L is the absorption path length in air. The oxygen concentration in the polystyrene foam can now be estimated as

$$c_{sm} = \frac{c_{air} L_{eq}}{v < t >} = \frac{g}{< t > v k_{gL}} \frac{c_{air}}{}, \tag{9}$$

where Eqs. (2) and (6), and substitution of $L = L_{eq}$ in Eq. (8) have been utilized. In order to minimize the influence of material inhomogeneities, temporal dispersion curves were also recorded for various lateral positions of the detector. The pulsed Ti:sapphire laser was employed in such a measurement on a 9.4 mm thick polystyrene foam slab. An experimental plot of the directly evaluated mean photon arrival time *versus* various injector-detector separations is shown in Fig. 6(a), derived from these measurements. A theoretical curve corresponding to the evaluated optical parameters is also plotted according to Eq. (4). In Fig. 6(b) the experimental value at different injection-detection separations of the ratio between the GASMAS signal and the mean time-of-flight, $k_{gt} \equiv g / < t >$, is shown together with a least square fit. The uncertainty in the ratio was 1.3%, evaluated using a 95% confidence interval of the experimental values. The only unknown factor left is the index of refraction of the scattering material n_{sm}, which determines the light velocity in the medium according to $v = c_0 / n_{sm}$, where c_0 is the light velocity in vacuum. Due to the homogeneous and isotropic nature of the porous material, the macroscopic index of refraction was estimated as a weighted mean of the refractive indices of the individual compounds contained, i.e.,

$$n_{sm} = P n_{air} + (1 - P) n_b, \tag{10}$$

where P is the material porosity, n_{air} and n_b are the indices of refraction of air and of the bulk material, respectively. In case of gas equilibrium with the surrounding atmosphere, the foam porosity P can be derived from the imbedded gas concentration using the relationship

$$P = \frac{V_{gas}}{V_{tot}} = \frac{c_{sm}}{c_{air}}, \tag{11}$$

where V_{gas} is the volume of gas in the porous material and V_{tot} is the total volume of the porous material. With an index of refraction of the polystyrene bulk material $n_b = 1.4$, and an atmospheric oxygen content of 20.8%, the oxygen concentration in the polystyrene foam can accordingly be evaluated using Eqs. (9-11) to yield $c_{sm} \approx 20.4\%$, and the corresponding foam porosity $P \approx 98\%$.

The mean time-of-flight of the photons, and consequently the imbedded gas concentration, can as described above also be evaluated indirectly using spatially-resolved measurement techniques. Experimental curves recorded with the GASMAS setup are shown in Fig. 7 for a 9.4 mm (a,b) and 39 mm (c,d) thick slab of polystyrene foam. Figs. 7(a,c) show the total transmitted light intensity as a function of the lateral

displacement, where the zero separation corresponds to the position where the transmitting and the receiving fibers are placed oppositely to each other. Figs. 7(b,d) display the GASMAS signal of the imbedded oxygen. Note that the transmitted light intensity falls off laterally at the same time as the GASMAS signal increases. The distributions are, as expected, broader in the case of the thicker slab. Theoretical curves (Eq. (5)) using the previously evaluated effective attenuation coefficient together with the experimental points are plotted in the figure. In the general case, the mean time-of-flight can thus be evaluated inserting the obtained optical parameters in the analytical formula Eq. (4). However, a fit of the theoretical curve to the spatially-resolved steady-state data measured at long injection-detection separation ($\rho >> z_0$) can only provide an unambiguous value for the lumped coefficient μ_{eff}, and not for μ_a and μ_s' separately. The imbedded gas concentration can thus not readily be assessed using only these kind of steady-state measurements.

Measurements on polystyrene foam slabs of different thickness were also performed and the variation of the equivalent mean path length with the slab thickness is plotted in Fig. 8. It can be seen in the figure that in the case of polystyrene foam, which has weak absorption and strong scattering properties, the mean time-of-flight related to the equivalent mean path length is proportional to the square of the thickness of the slab, i.e., $< t > \propto d^2$, as it is predicted by Eq. (4) for the case of low gas absorption. A similar relationship was also obtained considering the related topic of light propagation through clouds.[10]

5. Conclusions and discussions

In the present paper we show that the imbedded gas concentration can be estimated using time-resolved measurements together with the newly developed GASMAS technique. The proof of principle measurements were performed on atmospheric oxygen at a wavelength characterized by weak absorption. The gas was imbedded in polystyrene foam, which is a model material with high porosity and strong scattering properties. The evaluated porosity of polystyrene foam are comparable with manufacturing specifications. However, in the more general case of moderate porosity or of substantial gas absorption, it is still a subject for further investigation whether there is any preference for the photons to travel through the diffused gas or through the bulk material when being multiply scattered inside the porous material. This is a research topic that might reveal novel insights into the field of light propagation through confining media.

It should be noted that many aspects of the GASMAS technique do not require a detailed knowledge about the light propagation, as in the present case of an absolute concentration measurement. For instance, gas pressure, temperature, and ratios between gas concentrations, are quantities that can be readily evaluated, being independent of the light scattering inside the porous medium.

Gas tomography is another possible application of the technique. This extension corresponds to the one done for optical mammography and skull haematoma detection.

An alternative to the time and spatially-resolved techniques presented in the present paper, is to perform phase sensitive measurements in the frequency domain.[11, 12] A major advantage of such a method is that it only needs one single diode laser both for the GASMAS measurements and for the determination of the optical properties of the bulk material using modulation techniques.

This work was supported by the Swedish Research Council for Engineering Sciences (TFR), the Knut and Alice Wallenberg Foundation, and the Swedish Institute.

References

1. M. Sjöholm, G. Somesfalean, J. Alnis, S. Andersson-Engels, and S. Svanberg, "Analysis of gas dispersed in scattering media," Opt. Lett. 26, 16-18 (2001).
2. U. Gustafsson, G. Somesfalean, J. Alnis, and S. Svanberg, "Frequency-modulation spectroscopy with blue diode lasers," Appl. Opt. 39, 3774-3780 (2000).
3. B. Chance, J. S. Leigh, H. Miyake, D. S. Smith, S. Nioka, R. Greenfeld, M. Finander, K. Kaufmann, W. Levy, M. Young, P. Cohen, H. Yoshioka, and R. Boretsky, "Comparison of time-resolved and – unresolved measurements of deoxyhaemoglobin in the brain", Proc. Natl. Acad. Sci. USA 85, 4971-4975 (1988).
4. S. Andersson-Engels, R. Berg, S. Svanberg, and O. Jarlman, "Time-resolved transillumination for medical diagnostics", Opt. Lett. 15, 1179-1181 (1990).
5. M. S. Pattersson, B. Chance, and B.C. Wilson, "Time resolved reflectance and transmittance for the non-invasive measurement of tissue optical properties," Appl. Opt. 28, 2331-2336 (1989).
6. S. R. Arridge, M. Cope, D. T. Delpy, "The theoretical basis for the determination of optical pathlengths in tissue: temporal and frequency analysis," Phys. Med. Biol. 37, 1531-1560 (1992).
7. T. J. Farrell, M. S. Pattersson, and B. Wilson, "A diffusion theory model of spatially resolved, steady-state diffuse reflectance for noninvasive determination of tissue optical properties *in vivo*", Med. Phys. 19, 879-888 (1992).
8. J. S. Dam, P. E. Andersen, T. Dalgaard, and P. E Fabricius, "Determination of tissue optical properties from diffuse reflectance profiles by multivariate calibration", Appl. Opt. 37, 772-778 (1998).
9. R. Berg, O. Jarlman, and S. Svanberg, "Medical transillumination imaging using short-pulsed diode lasers", Appl. Opt. 32, 574-579 (1993).
10. U. Platt, Institute for Environmental Physic, University of Heidelberg, Heidelberg, Germany, private communication (2000).
11. J. K. Link, "Measurements of the radiative lifetimes of the first excited states of Na, K, Rb, and Cs by means of the phase shift method", J. Opt. Soc. Am. 56, 1195-1199 (1966).
12. J. Fishkin, E. Gratton, M. J. van de Ven, and W. W. Mantulin, "Diffusion of intensity-modulated near-infrared light in turbid media", Proc. SPIE 1431, 122-135 (1991).

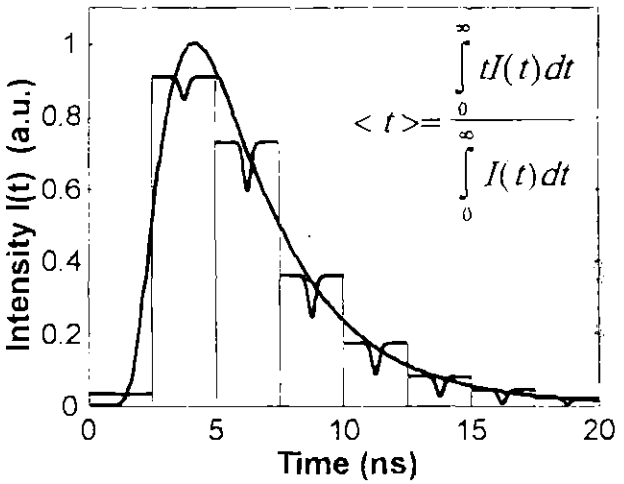

Fig. 1. Analytical time dispersion curve obtained for transillumination of a 39 mm thick slab with the optical parameters μ_a = 0.002 cm^{-1} and μ_s' = 40 cm^{-1} using short-pulsed light. For the sake of clarity, the direct absorption signals corresponding to photons that have traveled differently long distances in the material are intentionally exaggerated. The mean traveling time in the limit of small absorptions is shown as an insert in the figure.

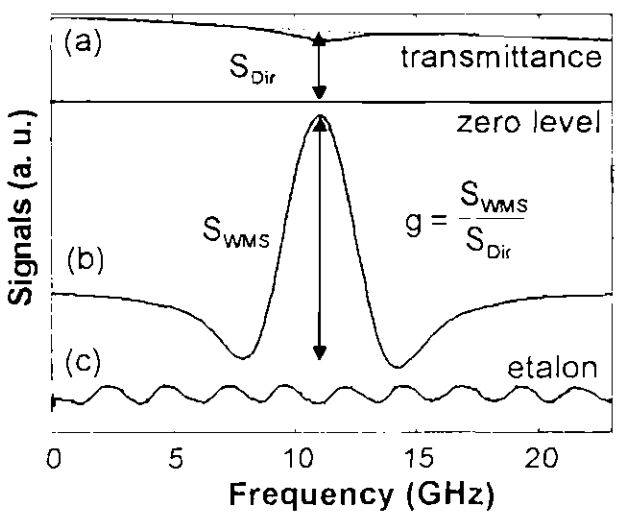

Fig. 2. (a) Direct absorption and (b) second-harmonic component of the WMS spectrum for the R7R7 line in the oxygen A band measured along a 10 m long path in air. (c) Low-finesse fringes from a 2.43 GHz free spectral range Fabry-Pérot etalon used for calibration of the frequency scale.

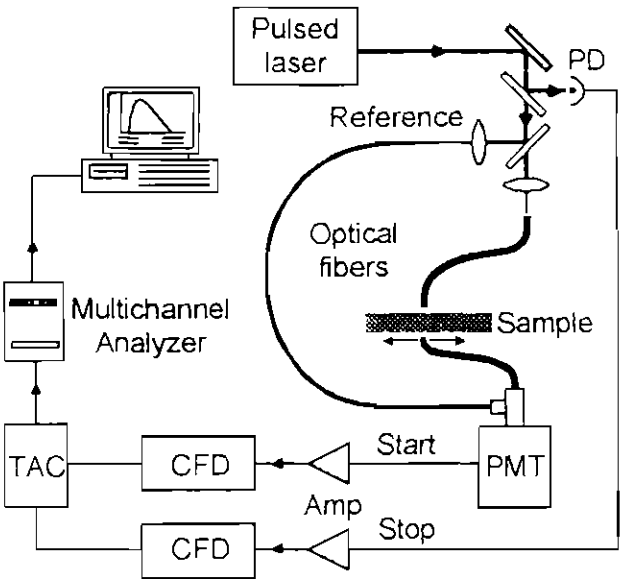

Fig. 3. Experimental set-up used for time-resolved measurements. PD, photo diode; PMT, photomultiplier tube; Amp, amplifier; CFD, constant fraction discriminator; TAC, time to amplitude converter.

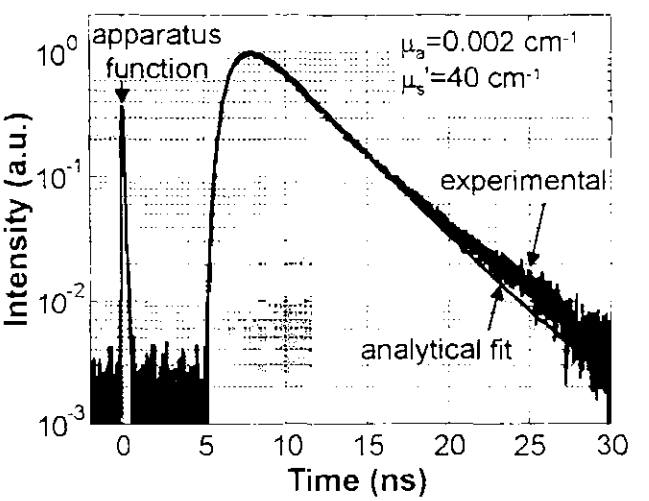

Fig. 4. Recorded time dispersion curve obtained when transilluminating a 39 mm thick slab of polystyrene foam using a diode laser source pulsed at 10 MHz. A fit of a theoretical curve and the instrumental transfer function are also depicted.

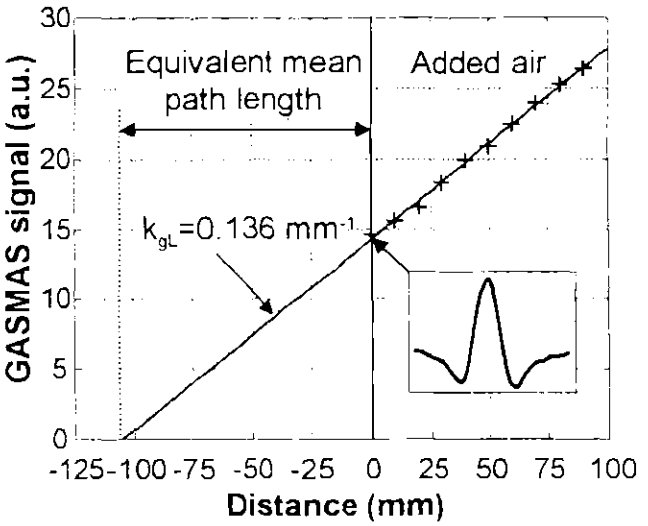

Fig. 5. Standard-addition plot for molecular oxygen obtained with the GASMAS setup showing the extrapolated equivalent mean path length for a 9.4 mm thick slab of polystyrene foam. The WMS signal obtained with the light-injecting collimator in direct contact with the sample is shown as an insert.

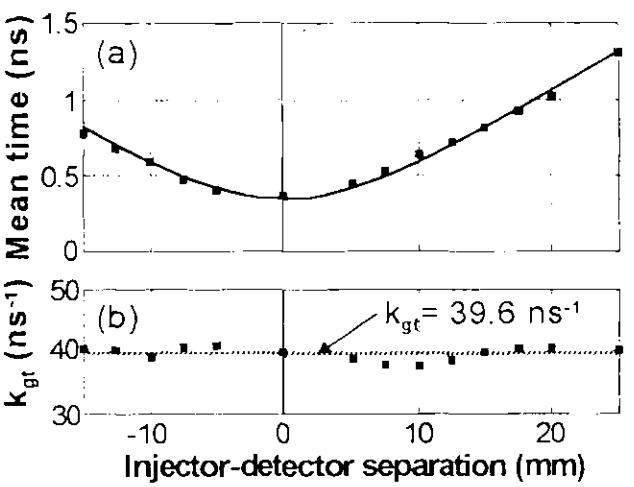

Fig. 6. (a) Recorded mean time-of-flight through a 9.4 mm thick slab of polystyrene foam measured using a pulsed Ti:sapphire laser. The solid line represents a theoretical curve corresponding to the evaluated optical parameters (μ_a = 0.002 cm^{-1}, μ_s' = 40 cm^{-1}). (b) The quotient between the GASMAS signal and the mean travelling time of the photons is shown together with a least square fit of the factor k_{gt} (pointed line).

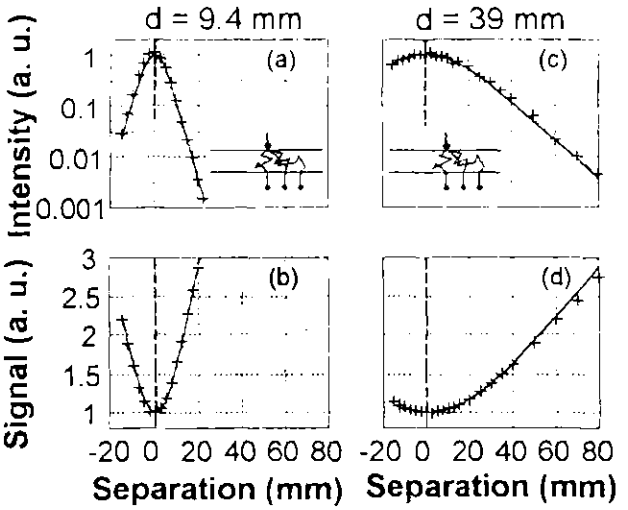

Fig. 7. Spatially-resolved transmission recordings measured with the GASMAS setup on two polystyrene foam slabs, (a-b) 9.4 mm and (c-d) 39 mm thick. The upper curves show the transmitted intensity, and the lower curves represent the detected oxygen absorption signal amplitude for different injector-detector separation distances. Fits according to the evaluated effective attenuation coefficient (μ_{eff} = 0.5 cm^{-1}) are also indicated. A schematic picture of the transillumination set-up is shown as an insert, and dashed lines at the zero position mark the symmetry axis.

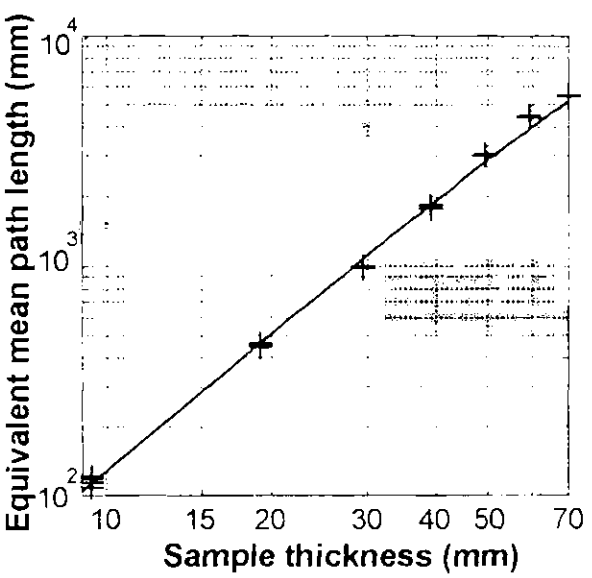

Fig. 8. Plot of the equivalent mean path length corresponding to oxygen absorption measured through differently thick slabs of polystyrene foam using a diode laser. The mean time-of-flight is proportional to the square of the slab thickness. The solid line corresponds to the theoretical curve evaluated using μ_a= 0.002 cm^{-1} and μ_s'= 40 cm^{-1}.